Component-based Simultaneous Topology and Continuous Fiber Layout Optimization of Additively-manufactured Parts

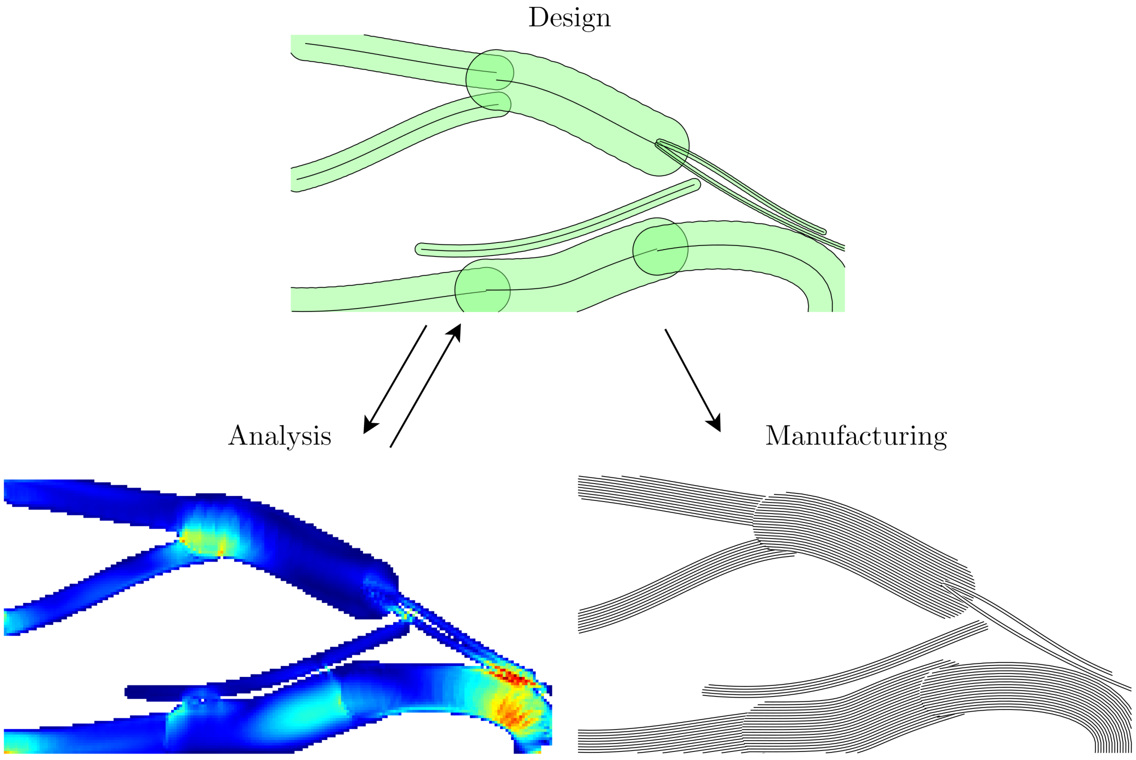

Master's Thesis
Design of Mechanical Systems
Aalborg University
31/05/2024

AALBORG UNIVERSITY
STUDENT REPORT

The Faculty of Engineering and Science
Mechanical Engineering and Manufacturing
Fibigerstræde 16
9220 Aalborg Øst
http://www.mp.aau.dk

Title:

Component-based Simultaneous Topology and Continuous Fiber Layout Optimization of Additively-manufactured Parts

Semester:

10th Semester

Semester theme:

Master's Thesis

ECTS:

30 Points

Project period:

01/02-31/05 2024

Supervisor:

Erik Lund | el@mp.aau.dk

Project members:

Andreas Weje Warén Larsen
Frederik Brun Hoff Østergaard

Issue: 1
Pages: 91
Date of submission: 31/05-2024

Signatures

Andreas Weje Larsen

Andreas Weje Warén Larsen

F.Ø.

Frederik Brun Hoff Østergaard

Summary

The topic of this thesis is simultaneous topology and fiber layout optimization for additive manufacturing processes. Topology optimization generates efficient parts of high geometric complexity, which may be realized by additive manufacturing. Using continuous fibers, high performance parts can be obtained, however, several manufacturing limitations complicates this process. Commercial methods rely on intuition to place the fibers, and in most other works where optimization is used, post-processing is needed in order to manufacture the results, leading to a difference between the product and analysis model and sub-optimal parts.

This thesis utilizes the Moving Morphable Components (MMC) framework, with the ersatz material model, for topology optimization. Each component is parametrized by a skeleton curve defined based on the Absolute Nodal Coordinate Formulation (ANCF). This formulation allows fibers to be defined from the skeleton, which in turn allows the definition of manufacturing constraints for the fibers. With this definition, fibers can move, merge and curve throughout the design domain.

The objective is to minimize compliance subject to a volume constraint. To manufacture the results, a minimum fiber length and maximum fiber curvature constraint is formulated. In each component the fibers are evenly spaced. Since fibers cannot be defined in the same place, an overlap constraint between the components is formulated. The endpoints of each component can merge to obtain inter-component fiber continuity. A failure index constraint based on the Tsai-Wu failure criterion is added to the formulation.

The results show that the proposed developments can be used to ensure manufacturability, and conformity between analyzed and produced part. If inter-component continuity is obtained, and all constraints are fulfilled, a topology and fiber layout with low compliance, reduced volume, that is not expected to fail and can be manufactured with limited post-processing, results from the scheme.

Finally, several suggestions are made to improve the numerical model, component- and optimization formulation.

Contents

Preface

This report represents the Master's thesis project for the degree of Master of Science in Design of Mechanical Systems at the Faculty of Engineering and Science, Aalborg University. The scope of the project is to do simultaneous topology and fiber layout optimization via the Moving Morphable Components framework, in a way that ensures manufacturable parts and displays conformity between the analyzed and produced part.

Reading Guide

Referencing

Referencing is done via the Harvard method. In cases where the authors name is used as part of the text, the reference is indicated by 'Name, (year)'. In cases where the author name is not used as part of the text the reference is indicated by '(Name, year)', at the end of the last sentence in a section. References for figures are in the figure caption and for tables, in a cell or the table caption. A list of references is given before the appendices. All references are blue to indicate a hyperref to the list of references.

Numeration (Sections, Figures and Tables)

Sections are numerated by up to three numbers; ($x.y.z$). In this number system, x designates the chapter, y designates the section and z designates the subsection. For figures, equations and tables, only two numbers are used, (x,y), where x designates the chapter and y designates the figure, equation, or table number. The appendices are alphabetized rather than enumerated.

Symbols and Abbreviations

A list of nomenclature, including symbols, abbreviations, notation and terminology, is given on the following page. This list applies to the entirety of the report, but is not extensive with respect to e.g. subscripts for symbols used a multitude of times.

All subscripts in this work indicate naming, e.g. σ_x is a stress in the x-direction. All superscripts are used as counters or powers, e.g. $\boldsymbol{\rho}^e$ is the density of element e. In case such a symbol is also raised to the power 2, the notation is $(\boldsymbol{\rho}^e)^2$.

This project has been supervised by Professor Erik Lund at Aalborg University.

Nomenclature

Abbreviations

AM	Additive Manufacturing. Synonymous with '3D-printing'.
ANCF	Absolute Nodal Coordinate Formulation.
BJT	Binder Jetting.
CAD	Computer-Aided Design.
CAE	Computer-Aided Engineering.
DED	Directed Energy Deposition.
DMO	Discrete Material Optimization.
EQS	Equally Spaced.
FEM	Finite Element Method.
FOS	Factor of Safety.
FR	Fiber-Reinforced.
HAZ	Heat-Affected Zone.
MBB	Messerschmitt-Bölkow-Blohm.
MEX	Material Extrusion.
MJT	Material Jetting.
MMC	Moving Morphable Components.
MTO	Multi-component Topology Optimization.
NURBS	Non-uniform Rational B-spline.
PA	Polyamide.
PBF	Powder Bed Fusion.
SHL	Sheet Lamination.
SIMP	Solid Isotropic Material with Penalization.
SOMP	Solid Orthotropic Material with Penalization.
TDF	Topology Description Function.
TO	Topology Optimization.
TSMMC	Time-Series MMC.
VPP	Vat Photopolymerisation.
XFEM	Extended Finite Element Method.

Notation

$[1, 10]$	Interval.
$[1 : 10]$	Integer interval.
$\|x\|$	Absolute value.
$\|\|\mathbf{x}\|\|$	Euclidian norm. Indexed for other norms, e.g. $\|\|\mathbf{x}\|\|_P$ for P-norm.

Vector and Index Notation

$-^{c}$	Component counter.
$-^{d}$	Design variable counter.
$-^{e}$	Element counter.
$-^{i}$	Iteration counter.
$-^{n}$	Node counter.
$-^{r}$	Endpoint relation counter.
$-^{s}$	Segment counter.

$\mathbf{M}$	Matrix (uppercase boldface).
$\mathbf{v}$	Vector (lowercase boldface).

Symbols and Letters

α_{int}	Relative weight.
ϵ	Heaviside smoothing parameter.
κ_{max}	Maximum fiber curvature in $[\mathrm{mm}^{-1}]$.
$\mathbb{H}$	Heaviside function, regularized.
$\mathbb{H}_\rho$	Nodal density field.
$\mathbb{H}_\theta$	Orientation field.
$\mathcal{F}_{TW}$	Failure index. Index ’TW’ denoting Tsai-Wu.
ϕ	Topology description function (TDF), or overhang angle.
θ	Component rotation angle in [Rad].
$\bar{\mathbf{Q}}$	Transformed plane stress-reduced constitutive matrix.
$\boldsymbol{\delta}$	Perturbation vector.
$\boldsymbol{\epsilon}$	Strain vector.
$\hat{\mathbf{f}}^r$	Combined endpoint relation function.
$\boldsymbol{\rho}^e$	Element density.
$\boldsymbol{\sigma}_{\mathbf{12}}$	Stress vector in the material coordinate system.
$\boldsymbol{\sigma}_{\mathbf{xy}}$	Stress vector in the Cartesian coordinate system.
$\boldsymbol{\theta}_{int}$	Inter-component endpoint angular difference vector.
$\mathbf{B}$	Strain-displacement matrix.
$\mathbf{C}$	Constitutive matrix.
$\mathbf{d}$	Design variable vector.
$\mathbf{f}$	Skeleton curve.
$\mathbf{f}^r_\theta$	Orientation relation function.
$\mathbf{f}^r_{dist}$	Distance relation function.
$\mathbf{K_e}$	Element stiffness matrix.
$\mathbf{K}$	Global stiffness matrix.
$\mathbf{l}_{contact}$	Sum of component radii at endpoints.
$\mathbf{l}_{int}$	Inter-component endpoint distance vector.
$\mathbf{p_A}$, $\mathbf{p_B}$	Component endpoint coordinates.
$\mathbf{p_{Ax}}$, $\mathbf{p_{Bx}}$	Component endpoint gradient vectors.
$\mathbf{Q}$	Plane stress-reduced constitutive matrix.
$\mathbf{S}$	Component shape function matrix.
$\mathbf{T}$	Transformation matrix.
$\mathbf{u}$	Displacement vector.
$\mathbf{w}^e$	Element strain energy density.
ξ	Component coordinate.
C	Compliance.
D_{sep}	Fiber separation distance.
F	Load, in [N].
F_i, F_{ij}	Tsai-Wu strength tensor.
g	Constraint.
L_{min}	Minimum fiber length in [mm].
N	Number, e.g. N_c is the number of components.
P	Aggregation parameter.

p	Penalization parameter.
t	Thickness.
V	Volume.
W_e	Extrusion width in [mm].
w_{int}	Inter-component weight factor.

Terminology

Fiber	Is used as a collective term for *fibers*, *strands*, *tows*, *threads* and *rovings*. Despite the differences, the thesis content applies to all 1D continuous reinforcements.

Material Properties

ν	Poisson's ratio.
E_1	Stiffness, in the material coordinate system, along the fiber direction, in [GPa].
E_2	Stiffnesses in the material coordinate system, transverse to the fiber direction, in [GPa].
G	Shear modulus in [GPa].
S	Shear strength in [MPa].
X_c	Compressive strength in the fiber direction, in [MPa].
X_t	Tensile strength in the fiber direction, in [MPa].
Y_c	Compressive strength transverse to the fiber direction, in [MPa].
Y_t	Tensile strength transverse to the fiber direction in [MPa].

1 Introduction and Thesis Motivation

The scope of this thesis is to do Topology Optimization (TO) of Fiber-Reinforced (FR) Additively Manufactured (AM) parts, where the topology and fiber layout is specified by TO. This chapter introduces these three subjects (TO, AM and FR) and presents what motivates their combination. Furthermore, an initial problem statement is formulated.

1.1 Additive Manufacturing

By additive manufacturing, it is meant that material is successively joined, for example layer upon layer, to create physical parts (DS/EN ISO/ASTM, 2022). The AM process is visualized in Fig. 1.1, where a computer model is converted to machine code and manufactured to form a physical part.

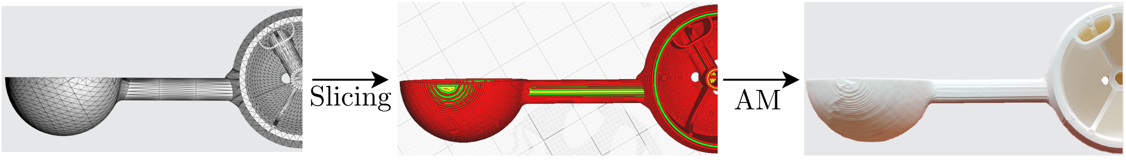

Model Machine code Part

Figure 1.1. The AM process.

By 2010, the original patents for a variety of AM-techniques expired, leading to a rapid increase in the number of machines, companies and products based on AM (Gibson et al., 2021). This is due to unique advantages AM offers.

AM offers parts of high geometric complexity without the need for part-specific tools. Thus, the cost-per-part for AM is relatively constant as opposed to conventional processes. In a number of ways, AM is faster than traditional processes, including the product development process, due to the CAD integration. Faster production and development, in turn, enables rapid prototyping and mass customization. Furthermore, since there is no part-specific tooling, local manufacturing is supported, leading to less transportation-related downsides such as costs, time and emissions (Gibson et al., 2021).

1.2 Topology Optimization

Topology optimization is a method for determining the optimal material distribution of a structure from a design domain, by extremizing a objective function or the combination of multiple. A widely used objective is compliance. As an example, Fig. 1.2 shows the design domain corresponding to the stiffness-optimized result in Fig. 1.3.

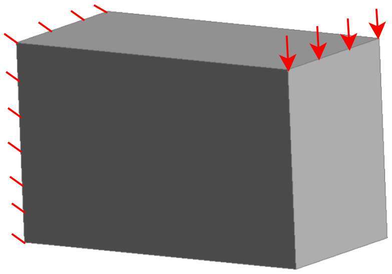

Figure 1.2. Design domain. Red indicating boundary conditions.

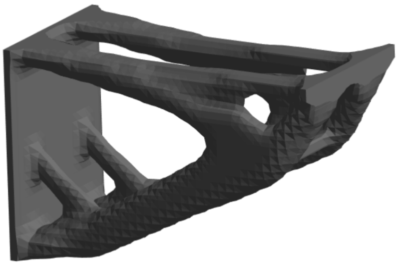

Figure 1.3. Stiffness-optimized result.

The removal of material is important in a wide range of aspects. Firstly, it may reduce raw material usage, which can reduce part cost and part emissions. Secondly, it will reduce part weight. Saving weight reduces the fuel consumption if the part produced is to be transported, or is part of the transportation vessel. In one aspect, this will reduce emissions (from transportation). In another aspect, the weight saved may be substituted for fuel capacity or more parts, such that the transportation range or payload capacity is increased.

1.3 Continuous Fiber Reinforcement

Composite structures are typically designed as a series of stacked lamina, consisting of two constituents; a fibrous material (e.g. carbon fibers) joined with a matrix material (e.g. a polymer). In each lamina, the fibers may be aligned in one direction, or woven in multiple directions. This work focuses on selectively deposited fibers, meaning that a single continuous fiber can be placed arbitrarily in a domain. Furthermore, different local orientations can be achieved, in the same layer, using multiple fibers.

If designed correctly, composite materials can exhibit improved stiffness, strength (static and fatigue), thermal, acoustic and density properties (Jones, 1999). Thus, with a higher stiffness- or strength-to-weight ratio, weight savings may also be achieved by composite materials, carrying over the same weight-saving advantages as were mentioned for TO. The composite materials treated in this thesis are purely with continuous fiber reinforcement, of which properties are known to be superior to the short-fiber- or particle-reinforced counterparts (Barbero, 2011). The properties of the structure depends on the material type, amount and location. Thus, by changing these parameters, composite materials allow tailoring of the properties of the material to its use. If the tailoring task is solved to perfection, the part possesses only the stiffness and strength that is needed in each direction (Jones, 1999). Naturally, the tailoring of composites must be done by some sort of decision maker, for example an optimization algorithm.

1.4 Initial Problem Formulation

The combination of the above three subjects is heavily motivated, for complex, lightweight, high-performance parts. It is not intuitive to design parts with the amount of spatial and material design freedom offered by AM and FR, thus the coupling with an optimal decision maker (TO) is needed to fully harness this freedom.

The task of combining these three subjects is not trivial. For some years, commercial software offered by AM-companies have based fiber layouts on intuition, by e.g. reinforcing the part perimeter. However, according to Boissonneault (2022), Computer-Aided Engineering (CAE) tools that can propose part shapes and fiber layouts based on optimization have undergone development, proving the industrial value of the task.

In order to obtain useful results, the AM process limitations must be taken into account during optimization, otherwise, the result cannot be manufactured. Furthermore, a variety of topology optimization frameworks exist, some better than others in terms of how much the result has to be post-processed in order to be manufactured. Post-processing is meant as changing the design after an optimized result is obtained, without re-analysis, in order to achieve e.g. manufacturable parts. With post-processing, considerable changes to the optimized objective function is to be expected, and some constraints may be violated. Thus, an initial problem formulation for this project is defined as outlined in the box below.

What are the limitations of AM-processes for selectively deposited fibers, and which topology optimization framework has advantageous formulations to take these into account?

This problem is treated in the next two chapters, forming the basis for formulating the problem statement of the thesis.

2 Continuous Fiber Additive Manufacturing

The purpose of this chapter is to identify the limitations of AM-techniques for manufacturing parts with selectively deposited continuous fibers. If a manufacturable result is sought from optimization of the fiber layout, the constraints must be known.

2.1 Overview of Continuous Fiber AM-processes

According to DS/EN ISO/ASTM (2022), seven AM-processes exist. The operating principle of each process is illustrated and explained in Appendix A. In this chapter, focus is drawn to the processes applicable to selective continuous fiber reinforcement, limiting the scope to four out of the seven processes, outlined in Tab. 2.1.

Process	**Acr.**	**Status**	**Reference**
Material extrusion	MEX	Commercial	Anisoprint, Markforged, 9T Labs
Directed energy deposition	DED	Commercial	AREVO
Vat photopolymerization	VPP	Research	(Lu et al., 2022) and (Khatua et al., 2023)
Powder bed fusion	PBF	Research	Baranowski et al. (2023)
Material jetting	MJT	N/A	[-]
Binder jetting	BJT	N/A	[-]
Sheet lamination	SHL	N/A*	[-]

Table 2.1. Continuous fiber AM-processes. 'N/A' meaning not applied. *Is commercial for woven fabrics, not selectively deposited fibers.

Binder- and material jetting are based on powder and droplet material deposition and have, to the authors knowledge, not been used with continuous fibers. The next two sections describe the continuous fiber AM-processes, and the limitations of these in Sec. 2.4.

2.2 Commercial Processes

Commercially available processes for continuous fiber additive manufacturing include material extrusion and directed energy deposition. This section describes these processes.

2.2.1 Material Extrusion (MEX)

The process of composite MEX-based AM is not much different from traditional MEX-based AM (see Appendix A). Fig. 2.1 shows a fiber (black) with matrix material (green) being extruded through a nozzle and deposited onto a build platform (Mason and Gardiner, 2022).

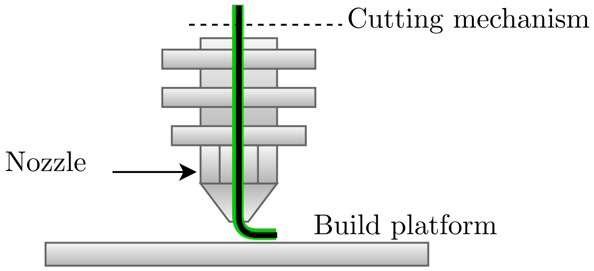

Figure 2.1. Material extrusion additive manufacturing (Mason and Gardiner, 2022).

Multiple different designs and patents thereof exist. The main difference between the designs is where the fiber is impregnated. Some manufacturers (e.g. Markforged) use filament which consists of both matrix and fiber material. Others (e.g. Anisoprint) use pre-impregnated fibers which are co-extruded with matrix material. Dry fiber bundles may also be impregnated during extrusion (Mason and Gardiner, 2022).

2.2.2 Directed Energy Deposition (DED)

To be classified as DED, materials must be melted and joined via focused thermal energy during deposition (DS/EN ISO/ASTM, 2022). Hence, DED for continuous fibers uses thermoplastic matrix materials. The DED process for fibers is conceptualized in Fig. 2.2 (Langnau, n.d.).

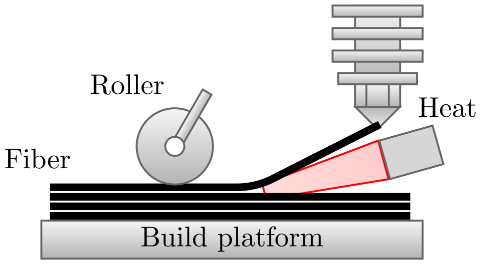

Figure 2.2. DED for continuous fibers (Langnau, n.d.).

This process resembles the aforementioned MEX-based process, as well as Automated Fiber Placement (AFP) processes. An additional fiber consolidation roller may be present (Langnau, n.d.). In the MEX-process the nozzle fulfills this function.

2.3 Experimental Processes

Other AM techniques have been used to manufacture parts with fiber reinforcement. Using other processes, alternative feedstock materials or formats may be used, tolerances and material properties may be improved or manufacturing time may be reduced. More importantly, for this work, they may be subject to other limitations. This section describes two processes; vat photopolymerization and powder bed fusion.

2.3.1 Continuous Fiber Vat Photopolymerization (VPP)

Vat photopolymerization uses a liquid photopolymer contained in a vat, which is selectively cured via a lightsource (DS/EN ISO/ASTM, 2022), see Appendix A. Lu et al. (2022) used VPP to cure layers such that they form a hollow channel into which the continuous fibers are placed, as illustrated in Fig. 2.3.

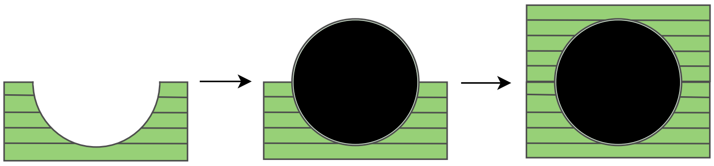

Figure 2.3. VPP with continuous fiber reinforcement as conducted in Lu et al. (2022).

Using this method, fiber reinforcement can be made in-plane and out-of-plane. A potential drawback to the process is that inserted fibers shield the light supplied for photopolymerisation, potentially leaving material in its green (uncured) state in the final part. However, using a post-curing step mitigates this effect (Lu et al., 2022).

Khatua et al. (2023) instead suspended fibers in the uncured polymer, and cured the matrix as the fiber was moved by a robot arm.

2.3.2 Powder Bed Fusion (PBF)

The PBF process is similar to VPP, however, instead of a photopolymer, a powder material which can be melted is used as feedstock. Powder is selectively melted, and a new layer added using a recoater, see Appendix A.

Baranowski et al. (2023) have designed a machine to selectively deposit fibers in a PBF process. The design is similar to a MEX-printhead situated on top of a powder bed. After a powder layer is deposited and selectively melted, a nozzle with continuous fiber remelts part of the layer, generating a heat-affected zone (HAZ) into which the fiber is deposited. The process is illustrated on Fig. 2.4.

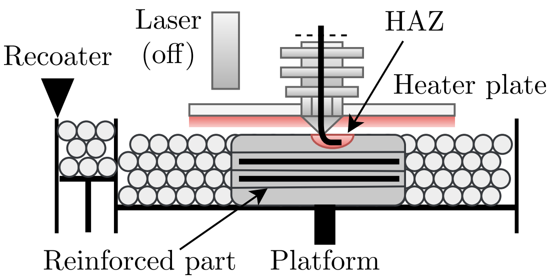

Figure 2.4. Conceptual sketch of the process given in Baranowski et al. (2023).

An additional heater plate is needed to keep the material within process temperature, and the HAZ need to be deep enough to fully contain the fiber, such that the recoater does not collide with deposited fiber.

2.4 Limitations of Fiber-reinforced AM

AM limitations have been sought to be fulfilled by constraints in the optimization formulation. These are e.g. overhang constraints, void constraints and feature-size constraints. For the continuous fiber AM-processes described above, more limitations apply. These, and the general AM limitations, are explained in the following. Focus is put on MEX-based processes since these are well-documented, however, the constraints apply to most or all of the processes above.

2.4.1 Minimum Fiber Length

At some point in the manufacturing process (e.g. when changing layer) the continuous fiber has to be cut. This is achieved by a blade near the nozzle. Although it is advantageous to keep the fiber continuous, the smallest fiber length will constrain the fiber layout. The distance between the blade and nozzle end sets the limit for the smallest fiber length achievable in the process. This length will vary between manufacturers. Two popular desktop printers from Markforged and Anisoprint are limited to 45 mm as the smallest fiber length (Markforged, 2022) (Top3DMedia, 2022).

2.4.2 Maximum Fiber Curvature

Zhang et al. (2021) investigated the effects of turning angle and radius of curvature experimentally and numerically using a Prusa I3 3D printer and Markforged 1K, 0.375 mm, carbon fiber filament. Increments of 30° turning angles are used and different curvature radii are examined. The results from the turning angle experiment are shown in Fig. 2.5.

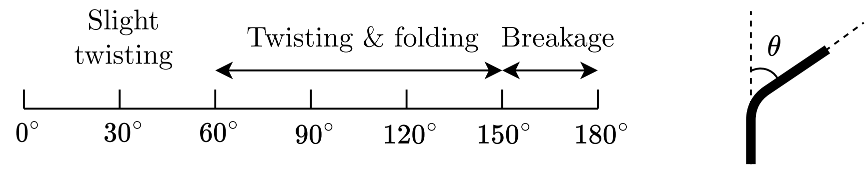

Figure 2.5. Turning angle effect. Data from Zhang et al. (2021).

As seen in Fig. 2.5, larger turning angles make the fibers twist and fold over, possibly leading to fiber breakage. Zhang et al. (2021) recommend a turning angle <120°. Fig. 2.6 shows the results of different curvature radii.

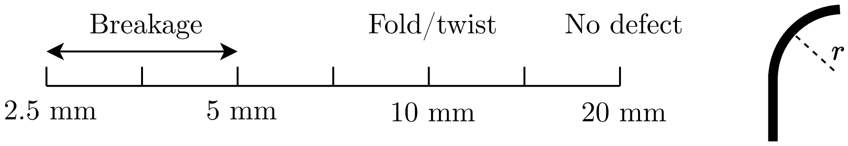

Figure 2.6. Radius of curvature effect. Data from Zhang et al. (2021).

From this experiment, Zhang et al. (2021) recommend a curvature radius of >5 mm. For different bundle sizes, the results may vary. Thus, more study is needed before recommendations can be made for specific machines (nozzle sizes, bundle sizes, materials etc.).

Matsuzaki et al. (2018) observed the same twisting/folding mechanisms in their experiments, which sought to test the error between set and printed radius for improving manufacturing robustness. Matsuzaki et al. (2018) used varying set radii and varying fiber bundle sizes. The results indicate a larger error for larger fiber bundle sizes which may be caused by the twisting/folding mechanisms.

2.4.3 Fiber Overlap and Feature Size

When a continuous fiber is printed in a layer, it cannot overlap with other fibers (or itself) in the same layer. Furthermore, fiber width and surrounding matrix material (together forming extrusion width) will govern the smallest feature size. For a single fiber and surrounding matrix material, the smallest feature size W_E is defined in Fig. 2.7 (Markforged, 2022).

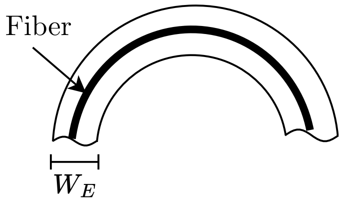

Figure 2.7. Extrusion width as explained by Markforged (2022).

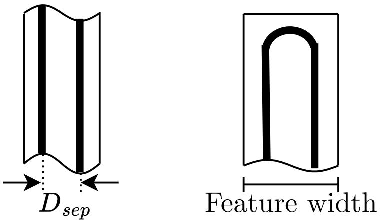

Figure 2.8. Fiber separation distance as explained by Markforged (2022).

For parallel fibers in the same layer, a smallest fiber separation distance, D_{sep}, is defined in Fig. 2.8. In some cases with open features, the same fiber has to loop back into the overall geometry (Fig. 2.8, right), in which both the curvature limitation and fiber separation defines a larger feature size. In 3D, a specified minimum layer height is also needed to add fiber reinforcement in 2D layers (Markforged, 2022).

2.4.4 Overhangs

In some AM-processes, a large overhang angle may require the use of support structures, which are structures that support the part during manufacture and are subsequently removed. The overhang angle is illustrated in Fig. 2.9. The smallest angle is process- and material dependent.

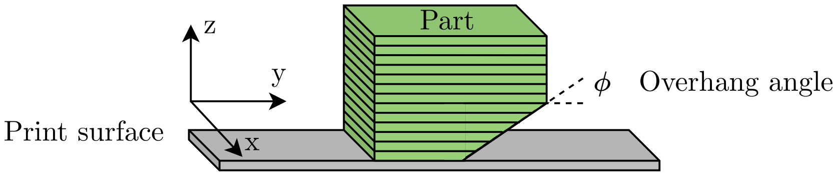

Figure 2.9. Overhang angle.

The use of support structures is undesired since they require additional steps for removal, may leave rough surfaces, consume material and add production time. Thus, several attempts have been made to avoid them during optimization (Khadiri et al., 2023).

2.4.5 Voids

If an optimized structure contains voids, support material within is not possible to remove. Assuming no support structures are manufactured, voids are still not allowable for some processes, such as PBF, due to the powder infiltrating the voids (Khadiri et al., 2023).

2.4.6 Listed Limitations

Throughout this chapter the limitations of AM-processes with selectively deposited continuous fibers were defined. For later reference, these are listed in Tab. 2.2.

Limitation	**Symbol**	**Used value**
Min. feature size	W_e	0.75 mm
Min. fiber length	L_{min}	45 mm
Min. separation distance	D_{sep}	0.75 mm
Max. fiber curvature	κ_{max}	$0.2\,\text{mm}^{-1}$
Max. overhang angle	ϕ_{max}	70°
Voids	[-]	[-]
No Z-reinforcement	[-]	[-]

Table 2.2. AM process limitations. Values based on Elmstrøm et al. (2023) (Anisoprint Composer A4 with carbon fiber filament). Overhang angle based on personal experience.

It is expected that taking into account the above limitations, realizable and high-quality structures are to result. The next chapter will present state-of-the-art approaches for topology- and fiber layout optimization, assessing their ability to include AM-limitations.

3 State of the Art: Topology Optimization of Continuous Fiber Structures

Since the work of Bendsøe and Kikuchi (1988), structural optimization and especially topology optimization has gained increasing interest. The implementation of anisotropic materials and specifically orthotropic fiber materials is increasingly studied in recent years due to new manufacturing methods as described in Chap. 2. The additional implementation of orthotropy and constraints caused by manufacturing of fiber composites, yields further development of the topology optimization formulations. The purpose of this chapter is to describe and evaluate problem formulations and corresponding consequences of different frameworks and underlying methods. For brevity, details on each framework are omitted and focus is drawn to their overall characteristics.

Topology optimization formulations are evaluated with reference to Fig. 3.1, which depicts three parts needed for design optimization and their relation. The design model is the structure, formulated from the parametrization of geometry, material or a combination of these. The analysis model is FEA. Hence, the design is discretized and analyzed, yielding the structure's behavior and sensitivities for design update. The manufactured model is not necessary for topology optimization but included due to the manufacturing constraints posed for realizable design.

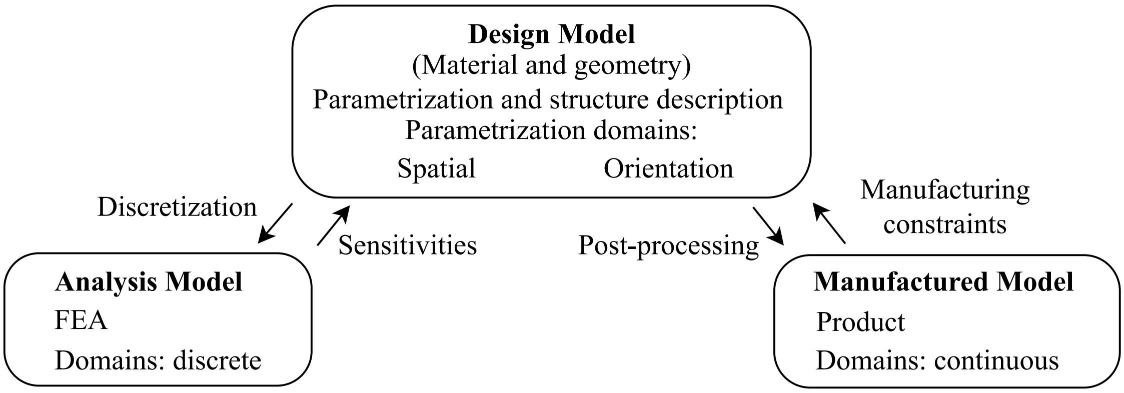

Figure 3.1. General fiber topology design problem.

In Papapetrou et al. (2020) the importance of design for failure is exemplified showing different structures and fiber layouts having approximately equal compliance but radically different failure load. Even the same structure with a slight change in fiber angle shows this characteristic. Due to these local failure characteristics and the posed manufacturing constraints, the conformity between the analysis and manufactured model is essential for design. Hence post-processing that changes the design after an optimized result is obtained is undesired.

The conformity between analysis and manufactured model is achieved through the design model. The parametrization of the design model is divided into a spatial and orientation domain. The parametrization, structure descriptions, limitations and post-processing needed for different methods are investigated in the following, where methods are divided into three overall topology frameworks, categorized as material penalization, level-set and moving morphable components.

3.1 Material Penalization-based Approaches

The material penalization categorization is defined by the design model altering material properties and not the geometry of the structure directly, implying the topology is formed by altering densities to 0 or 1 in a fixed subdomain. When the design depends on a fixed subdomain, the design and analysis model are fused and inseparable. The methods presented are inspired or further developed from the Solid Isotropic Material with Penalization (SIMP) method (Bendsøe and Sigmund, 2004).

3.1.1 Solid Orthotropic Material with Penalization (SOMP)

This method is a direct further development of the SIMP method. In SIMP the density in every element of a fixed grid is a design variable, which is penalized to make intermediate densities uneconomical. Hence, the structure is formed by element-wise densities of 0 or 1 (Sigmund, 2001). To incorporate fibers, an additional orientation design variable is introduced in every element (Schmidt et al., 2020)(Papapetrou et al., 2020). To exemplify SOMP, a short cantilever beam is sketched in Fig. 3.2 where gray elements in the initial structure resembles unknown density and orientation. When iterating the structure is formed and orientations, indicated with red, are found.

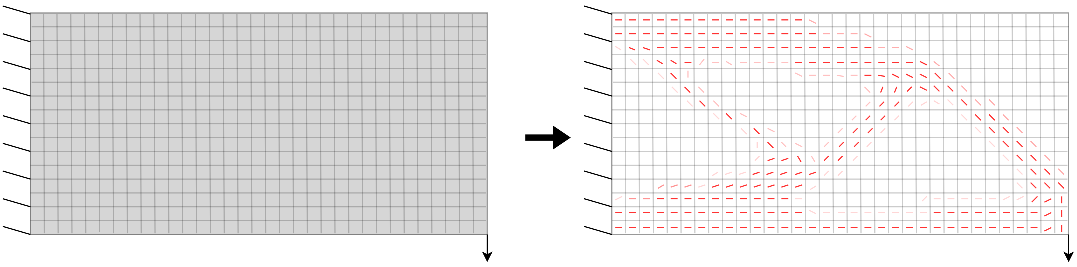

Figure 3.2. Sketched short cantilever beam example using SOMP inspired by Zhang et al. (2024).

Since SOMP is directly developed from SIMP, problems such as mesh dependency, intermediate densities and checkerboarding are inherent to the method. These problems can however be alleviated by e.g. filtering (Bendsøe and Sigmund, 2004). The main concern of SOMP is the lack of fiber continuity. Since the parametrization is a continuously varying orientation in every element, nothing governs adjacent elements to ensure orientation alignment or a maximum angular difference. Hence, fiber orientations are discontinuous element-wise. This especially causes problems at intersecting members considering manufacturing constraints as no overlapping fibers, minimum fiber length etc. To alleviate this problem orientation filtering is implemented, however filtering explicitly describing manufacturing constraints has, to the authors knowledge, not yet been achieved (Schmidt et al., 2020)(Elmstrøm et al., 2023) (Zhang et al., 2024). Therefore post-processing of the optimized result for manufacturing constraints is needed. This is also referred to as path planning.

Multiple methods for path planning exist, however only the methods using the filtered fiber orientations are briefly presented. The streamlining method is conceptualized by dropping a particle somewhere in the solid geometry and letting the particle follow the orientation vector field. By this a continuous path is created, however control of this path considering manufacturing has not matured (Elmstrøm et al., 2023) (Papapetrou et al., 2020). The equally spaced (EQS) method uses horizontal or vertical subdivision of geometry where the number of fibers at each division line is equal throughout the structure. This creates continuous fibers in the direction of the subdivision and Papapetrou et al. (2020) suggest an equal fiber spacing at each division line. Zhang et al. (2024) suggest an additional fiber volume fraction design variable to enable nonequal fiber spacing at each division line. However the EQS method does not enable fiber termination or fibers enclosing voids. Further, this method is not suitable for handling complex geometries (Zhang et al., 2024).

From the previous descriptions, the following properties of the SOMP method are highlighted. For this, and the following, lists '$\oplus$' refers to a positive statement, '$\ominus$' a negative and '$\odot$' a neutral statement.

$\oplus$ Nonrestrictive - design evaluation of density and orientation on element basis.
$\ominus$ Mesh dependence.
$\ominus$ Intermediate densities.
$\ominus$ Trapping in local minima.
$\ominus$ Lack of fiber continuity.
$\ominus$ Post-processing needed - path planning.
$\ominus$ No fiber discontinuity modeling.

Since path planning as post-processing is necessary, the correlation of analysis and manufactured model is compromised leading to lost knowledge of product performance. This is specifically important considering the drastic change in failure load by change in local fiber orientation or discontinuity.

3.1.2 Discrete Material Optimization (DMO)

DMO was first introduced by Stegmann and Lund (2005) and was originally posed for laminate shell structures optimized for material, orientation and stacking sequence. However a 2D beam in four-point bending is exemplified, hence the method could be used for fiber placement. The method uses the concept of material penalization to evaluate the optimum between a set of materials, including discrete fiber orientations as different materials, in a fixed subdomain. For reference a depiction of this method is equal to SOMP in Fig. 3.2 where gray elements mean intermediate materials and orientations being fixed to a predefined set.

Development of DMO for continuous fiber optimization is investigated in Gadegaard and Thuesen (2022) combining the density penalization of SIMP with the discrete orientations of DMO. The purpose was to minimize post-processing by enhancing predefined fiber continuity due to the discrete orientations, but results proved further need of post-processing for length scaling and orientation intersections. Thereby, the following remarks are noted.

- ⊙ Restrictive - discrete fiber orientations which will influence the spatial optimization.
- ⊖ Mesh dependent.
- ⊖ Intermediate materials.
- ⊖ Trapping in local minima.
- ⊕ Fiber continuity by having the same discrete material in adjacent elements.
- ⊖ Post-processing needed - path planning - alleviated compared to SOMP.
- ⊖ No fiber discontinuity modeling.

3.1.3 Multi-Component Topology and Material Orientation of Composite (MTO-C)

Multi-component topology optimization (MTO) was originally meant for structure decomposition defining substructures (components) due to manufacturing considerations. This problem was solved by discrete density and joint variables in a fixed subdomain. For efficient computation the discrete formulation is proposed relaxed and penalized in Zhou and Saitou (2018) enabling gradient-based computation. Thereby, the method has a continuous density variable in every element as in SIMP. Implementation of orthotropic material properties is achieved in Zhou et al. (2018) by a three-layer design field as depicted in Fig. 3.3. The first design field is the density field (1) the second the membership field (2) here depicted with three members and lastly the orientation field (3). The orientation fields use a curvilinear description which is depicted unidirectional. By this description, the design variables are identified as continuous penalized density (1) and membership fraction (2) combined with continuous component-wise curvilinear fiber orientation (3). The distinction between members and components are members being of same curvilinear description and components being constructed from adjacent element densities and curvilinear description.

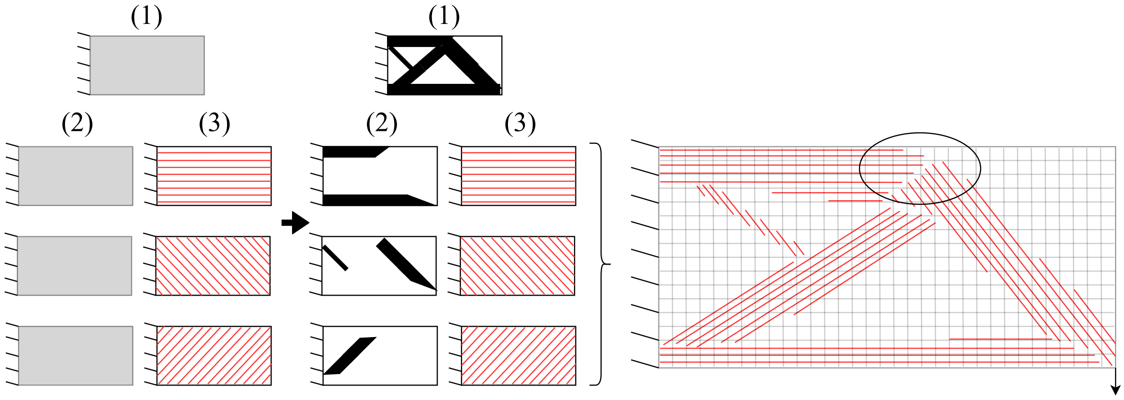

Figure 3.3. Sketched short cantilever beam example using MTO-C inspired by (Zhou et al., 2018).

The density field variable causes the design and analysis model to be fused leading to the same problems as SIMP. Another consequence of the fused modeling is lack of fiber discontinuity modeling at component intersections. By allowing curvilinear component-wise orientation, alignment of fibers at component ends might be obtained e.g. in the encircled area in Fig. 3.3. This leads to an analysis model description as continuous fibers and thereby strength overestimation. Since the manufactured model does not have continuous fibers at intersections, conformity is lost.

The components-wise orientation enables explicit posing of manufacturing constraints as maximum curvature and a predefined fiber continuity which alleviates post-processing. However design freedom is restricted to the number of members (Zhou et al., 2018). This is alleviated by increasing the number of members but as a consequence, additional components are introduced, which increase the number of discontinuous fibers. Thereby, the method suffers from a tradeoff between design freedom, manufacturing constraints and reliability of manufactured model. The following remarks are noted for method comparison.

- ⊖ Restrictive - structure becomes dependent of the number of members.
- ⊖ Mesh dependent.
- ⊖ Intermediate densities.
- ⊖ Trapping in local minima.
- ⊕ Fiber continuity - component-wise.
- ⊙ Tradeoff between design freedom and analysis/manufactured model conformity.
- ⊕ Maximum curvature manufacturing constraint by curvilinear member orientation.
- ⊕ Limited post-processing needed - no path planning.
- ⊖ No fiber discontinuity modeling.

3.2 Level-set Topology-based Approaches

Level-sets were first used for topology optimization by Sethian and Wiegmann (2000) and is a higher order function propagation framework, hence the parametrization is mainly on geometry as opposed to material in penalization methods. The solid structure is formed as an embedding of a higher dimensionality function on an iso-surface. The surface of the embedding is then allowed to propagate during optimization, implicitly altering the higher dimensionality function. In this framework formulation, the design and analysis model are separated and mesh dependency, pseudo densities etc. are removed (Wang et al., 2003). Implementation of fiber orientation has been achieved by two overall approaches. One approach separates the spatial and orientation parametrization. Thereby, the spatial domain is defined from a level-set and orientations are parametrized element-wise inside the level-set. This separation enables sequential or simultaneous spatial and orientation optimization (Xu et al., 2022)(Mokhtarzadeh et al., 2024). Another approach is having both spatial and orientation parametrization on the level-set description. Thereby, the fiber placement is defined from the structure edge or the higher order function itself (Papapetrou et al., 2020)(Xu et al., 2024). With the scope of simultaneous optimization and due to the similarities to penalization-based approaches, only approaches with both parametrizations on the level-set are further investigated.

To the authors knowledge, only two similar simultaneous methods, with orientation parametrization on the level-set, have been proposed. These are the offset and fast-marching method. Both methods utilize the level-set for primary fiber path placement, meaning a fiber is placed along all structure edges. For placement of fibers inside the solid domain, referred to as secondary paths, the methods differ. The offset method simply uses a fixed offset distance of the primary fiber path for secondary paths. Problems occurring using this method are fiber overlap, gaps and acute fiber angles (Papapetrou et al., 2020). To alleviate these problems a fast-marching approach for enabling differing offset distancing is implemented in Xu et al. (2024). Utilizing these methods, the inherent difference in design parametrization (spatial and orientation) is mainly restricted to the orientation being derived from the spatial edge. A depiction is seen in Fig. 3.4.

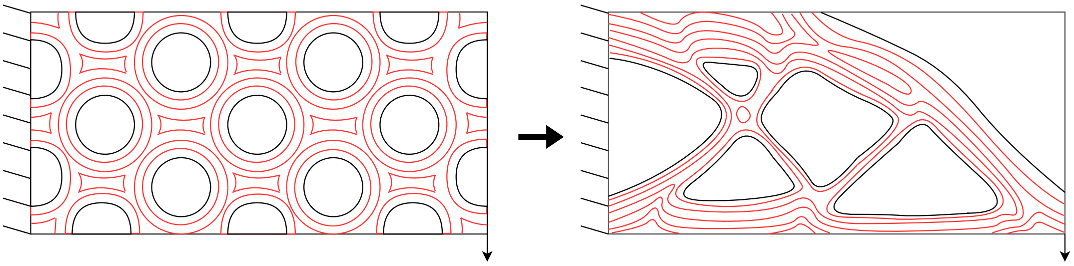

Figure 3.4. Sketched short cantilever beam example using fast marching. (Xu et al., 2024).

The described methods are further expansions of the level-set topology framework carrying on problems such as lack of nucleation and initial guess dependency. However due to concurrent spatial and orientation optimization, fiber continuity is ensured from edge descriptions alleviating manufacturing constraints but neglecting fiber discontinuity at e.g. fibers enclosing voids. The following remarks are noted for comparison.

- ⊖ Restrictive design - orientations mainly given from edge geometry.
- ⊕ Mesh independence.
- ⊕ Explicit boundaries.
- ⊖ Trapping in local minima.
- ⊖ Nucleation problem.
- ⊙ Fiber continuity - edge distance dependent.
- ⊖ Fiber overlapping, gaps, acute fiber angles - alleviated by fast marching.
- ⊕ Limited post-processing needed.
- ⊖ No fiber discontinuity modeling.

3.3 Moving Morphable Components (MMC) Based Approach

The MMC framework for topology optimization uses multiple overlapping level-set embeddings to form a structure. This methodology was firstly introduced by Guo et al. (2014) with inspiration from the general level-set framework. The difference of these frameworks is highlighted by the MMC utilizing multiple higher order functions on the same reference domain and allowing the embedding of these, referred to as components, to interact. By interaction the complexity of the structure is determined from the number and complexity of components. Hence increasing the number of components allows for a simple geometric component parametrization to be efficient to sustain structure complexity and vice versa (Zhang et al., 2016). From this formulation the framework adopts design and analysis model separation and thereby mesh independence and explicit boundaries without nucleation problems.

Implementation of orthotropic material is proposed by Smith and Norato (2021) using a bar component description and placing the fiber orientation along the length of the bar, as depicted in Fig. 3.5. In the example, parametrization is reduced to component center coordinates, length, width, and orientation. Another parametrization used in Sun et al. (2022) allows for variable width and separated component and fiber orientation.

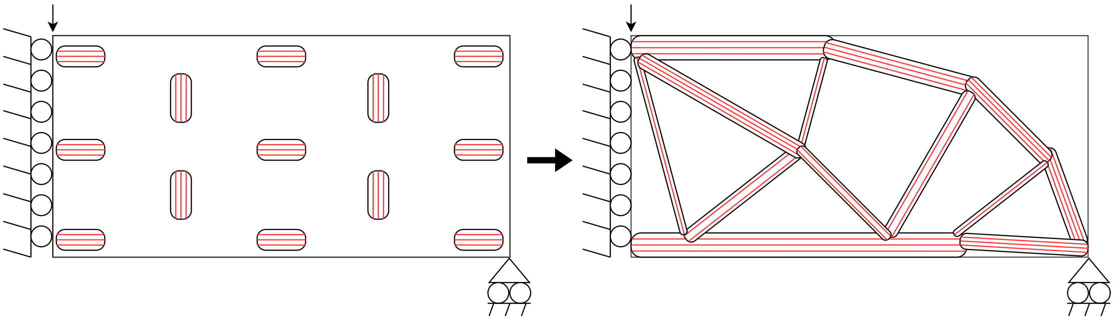

Figure 3.5. Sketched MBB beam example by MMC inspired by (Smith and Norato, 2021).

The structure forming by overlapping components is prohibited by orthotropic materials not allowing for overlap. Thereby, specific handling of component intersection is needed and two methods are proposed. The method proposed in Smith and Norato (2021) use an evaluation criteria based on strength to choose a favorable component. Thereby, the intersecting part of the unfavorable component is neglected in the embedding. Sun et al. (2022) elongates components by adding isotropic material at component ends while prohibiting the orthotropic parts from intersecting. To the authors knowledge, a method for fiber continuity at component intersection, has not been attempted. Due to this, and no fiber discontinuity modeling, the same tradeoff of design freedom and conformity, as described in Sec. 3.1.3, occurs. Thereby, the following remarks are noted.

- ⊖ Restrictive - Components limited to parametrization and structure to the number of components.
- ⊕ Mesh independent.
- ⊕ Explicit boundaries.
- ⊖ Trapping in local minima.
- ⊖ Initial guess dependent.
- ⊖ Component intersection method needed.
- ⊙ Fiber continuity - component-wise.
- ⊙ Tradeoff of design freedom by component number and conformity.
- ⊕ No post-processing.
- ⊖ No fiber discontinuity modeling.

3.4 Method Comparison

As stated in Fig. 3.1 topology optimization of continuous fibers consist of three parts which are design, analysis and manufactured model and the correlation of these. The manufactured model was included to describe method limitations and design alterations needed for realizable design, due to the constraints posed from Chap. 2. Thereby, the general task of topology optimization of continuous fiber structures can be formulated as:

Formulate topology optimization algorithm for posing of ***manufacturing constraints*** *without* ***restricting design freedom*** *and* ***fiber continuity*** *while minimizing* ***post-processing*** *to retain conformity of analysis and manufactured model*

The bold font keywords are used as method evaluation criteria in Tab. 3.2. To summarize the described frameworks and methods, the method parametrizations are listed in Tab. 3.1.

Framework	Design/ analysis	Method	Spatial	Orientation
Penalization	Fused	SOMP	Density in element	Continuous in element
		DMO	Material in element	Discrete in element
		MTO-C	Density in element	Curvilinear in component
Level-set	Separate	-	Higher order function	Continuous
MMC	Separate	-	Component description	Continuous in component

Table 3.1. Method parametrizations.

The consequences of these parametrizations are described and listed throughout this chapter and a keyword description of the main concerns are listed in Tab. 3.2 according to the criteria.

Method	Design restriction	Post-processing	Manufacturing constraints	Fiber continuity
SOMP	Mesh resolution	Path planning and intermediate densities	Filtering and post-processing	Element-wise - Filtering and post-processing
DMO	Mesh resolution and discrete orientations	Path planning and intermediate materials	Filtering and post-processing	Element-wise - Filtering and post-processing
MTO-C	Mesh resolution, number of members and curvilinear orientation	Intermediate densities	Component filtering and curvature limit	Component-wise
Level-set	Nucleation and secondary fiber placement	None	Fast-marching	Edge dependent
MMC	Component parametrization and number	None	Component parametrization limits	Component-wise

Table 3.2. Consequences of parametrization.

From Tab. 3.2 a general tendency of design freedom vs. manufacturing is interpreted, where one thing does not come without a cost of the other. This is especially seen in the difference of frameworks where level-set and MMC in general are restrictive in design but manufacturing is easier posed with larger areas of continuous fibers while retaining conformity. The cause of this correlation is thought to be the restrictive design of utilizing continuous fibers.

Meant by restrictive design, is that manufacturing-constrained continuous fibers are geometries themselves. Therefore, topology optimization using continuous fibers is a problem of fitting these restricted geometries to a combined structure. Thereby, the idea of parametrizing these geometries, creating a design-manufacturing correlation, occurs.

Having an element-wise parametrization, as penalization methods, causes more design freedom than the actual manufacturing allows, hence design restrictions cannot be posed without post-processing and loss of conformity occur. Therefore, these methods are undesirable. In the level-set method using fast-marching, the design freedom is further restricted by the secondary fiber placements method, nucleation problem and initial guess dependency.

By the MMC method, manufacturing constraints could be posed directly as limits on the component parametrization creating the previously described design-manufacturing restriction correlation. By this, no post-processing is needed and fiber continuity is guaranteed component-wise. However the described methods in Sec. 3.3 only utilize bar components and the potential of fiber continuity across components is neglected, hence the methods have not matured.

Therefore, the MMC framework is further developed for simultaneous topology and fiber layout optimization in this work.

4 | Problem Statement

The goal of this work is to design structures with optimal material- and fiber layouts, that are manufacturable by AM-processes, without the use of post-processing to achieve conformity between analysis and manufactured model. Based on the previous chapter, the MMC framework is a strong candidate to solve this problem, if inter-component continuity can be achieved and a component description allowing for the definition of the manufacturing limitations can be found or created.

As a starting point, minimization of compliance subject to a volume constraint is used as the formulation, and thus the problem statement is outlined as follows.

> *How can an MMC-based scheme be developed for compliance minimization by simultaneous topology and fiber layout optimization, with selectively deposited continuous fibers, to ensure manufacturability and analysis-product conformity?*

Taking failure into account in the optimization is of importance, thus, this is included in the developed formulation after manufacturability is ensured. To provide an overview of the following chapters, the optimization problem is depicted below. The numbers indicate the chapters in which the formulations are handled.

Minimize Parametrization ⑥	Compliance ⑤⑥
Subject to	Max. vol ⑥
	Min. feature size ⑥
	Min. fiber separation distance ⑥⑦
	Min. fiber length ⑦
	Max. curvature ⑦
	Failure ⑧

The MathWorks MATLAB code for MMC-based topology optimization given in Zhang et al. (2016) will be used as a starting point. Only two-dimensional problems are considered, and only static failure is considered.

5 | Initial MMC Framework

This chapter presents the starting point for the developed code for simultaneous topology and fiber layout optimization using the MMC framework. First, essential definitions of the MMC method are presented. Next, the 188-line MATLAB program given by Zhang et al. (2016) is briefly presented. Lastly, subsequent modifications for implementation of orthotropic FEA and the used material parameters are presented.

5.1 Definitions of MMC

To shorten the review of different methods in Chap. 3, the details of each method were not presented. The MMC method is explained in greater detail in this section.

5.1.1 Topology Description

As mentioned in Chap. 3, the MMC method relies on the interaction of multiple components, described by higher-order functions, to form a structure. Such higher order functions (or topology description functions, TDF) are denoted by ϕ (or ϕ^c for the c$^{\text{th}}$ component). The topology of a component is thus described by the level-set in Eq. (5.1) (Zhang et al., 2016).

$$\begin{cases} \boldsymbol{\phi}^c(\mathbf{x}) > 0, & \text{if}\, \mathbf{x} \in \Omega^c \\ \boldsymbol{\phi}^c(\mathbf{x}) = 0, & \text{if}\, \mathbf{x} \in \partial\Omega^c \\ \boldsymbol{\phi}^c(\mathbf{x}) < 0, & \text{if}\, \mathbf{x} \in D \setminus \Omega^c \end{cases} \tag{5.1}$$

Here, Ω^c is the region occupied by $\phi^c \geq 0$ (solid geometry) and $\Omega^c \subset D$ where D is the design domain. The components are assembled via Eq. (5.2).

$$\boldsymbol{\phi}_s(\mathbf{x}) = \max(\boldsymbol{\phi}^c(\mathbf{x})), \quad c = [1 : N_c]; \tag{5.2}$$

From which it follows that $\Omega_s = \cup_{c=1}^{N_c} \Omega^c$ yielding the topology of the entire structure. The concept of using Eq. (5.1) and Eq. (5.2) is graphically depicted in Fig. 5.1.

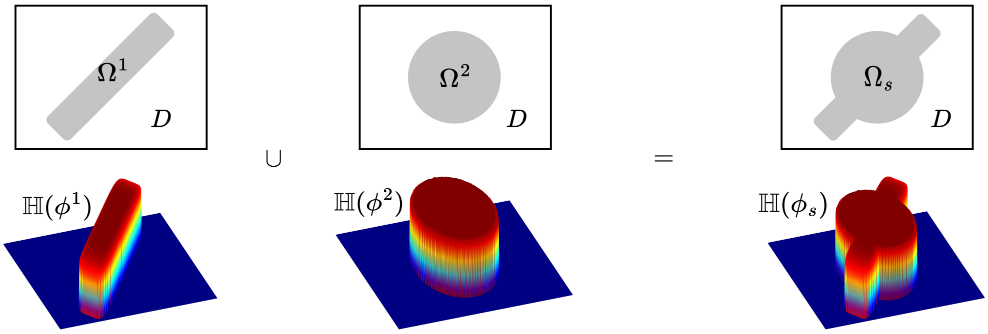

Figure 5.1. Topology description and component assembly in the MMC method. Inspired by Zhang et al. (2016).

The Heaviside function, $\mathbb{H}$, used in Fig. 5.1 is explained in the following.

5.1.2 Component Description

In the authors perspective, the ability to choose the TDF is one of the main virtues of the MMC method, as it allows for changing the structural complexity while being able to choose the number, and type, of design variables.

In the revised work of Zhang et al. (2016), components are described by the TDF given in Eq. (5.3a).

$$\phi^c(x,y) = \left(\frac{x'}{L^c}\right)^p + \left(\frac{y'}{f(x')}\right)^p - 1 \tag{5.3a}$$

$$\begin{Bmatrix} x' \\ y' \end{Bmatrix} = \begin{bmatrix} cos(\theta^c) & sin(\theta^c) \\ -sin(\theta^c) & cos(\theta^c) \end{bmatrix} \begin{Bmatrix} x - x_0^c \\ y - y_0^c \end{Bmatrix} \tag{5.3b}$$

In Eq. (5.3a), p determines the roundness of the corners, L is the component length, $f(x')$ is the thickness through the length. x' and y' form the local component coordinate system, determined by the component angle θ^c. In the original work of Guo et al. (2014) the term $f(x')$ was simply t for a uniform thickness whereas in Zhang et al. (2016) multiple $f(x')$ functions are proposed for uniform, linearly varying and quadratically varying thickness through the length.

5.1.3 Projection for Finite Element Analysis

No matter which TDF are used, if structural optimization is to be done, the union of them shall somehow be modeled in a finite element context. To this end, XFEM is used for remeshing component boundaries in Guo et al. (2014) for a completely binary material distribution. In Zhang et al. (2016), for computational reasons, the ersatz material model is utilized for projection onto a fixed FE-grid using a regularized Heaviside function, making intermediate densities along the component edges (Dambrine and Kateb, 2010). Thus, the level-set of the structure TDF, ϕ_s in Fig. 5.1, is projected onto a fixed nodal grid to form the nodal density field $\mathbb{H}_\rho$. This is computed by the smoothed Heaviside function in

Eq. (5.4) from Zhang et al. (2016).

$$\mathbb{H}_\rho = \begin{cases} 1, & \phi_s > \epsilon \\ \frac{3(1-\alpha)}{4}\left(\frac{\phi_s}{\epsilon} - \frac{{\phi_s}^3}{3\epsilon^3}\right) + \frac{1+\alpha}{2}, & -\epsilon \leq \phi_s \leq \epsilon \\ \alpha, & \phi_s < -\epsilon \end{cases} \tag{5.4}$$

The Heaviside function is smoothed to maintain differentiability and the parameter α is a non-zero positive value to avoid singular stiffness when components do not overlap. The parameter ϵ defines the interval on ϕ_s to consider as edge and assign intermediate densities.

5.2 MATLAB Code: MMC188.m

Fig. 5.2 outlines a pseudo-code of the 188-lines MATLAB script given in Zhang et al. (2016). The file `main.m` is used as a call to the function `MMC188.m`. Input from `main.m`, e.g. mesh size, component dimensions, loads and material, is used to initialize the code. The element stiffness matrix is defined using the function `BasicKE.m`. In the main loop, the components are assembled (Eq. (5.2)) and plotted.

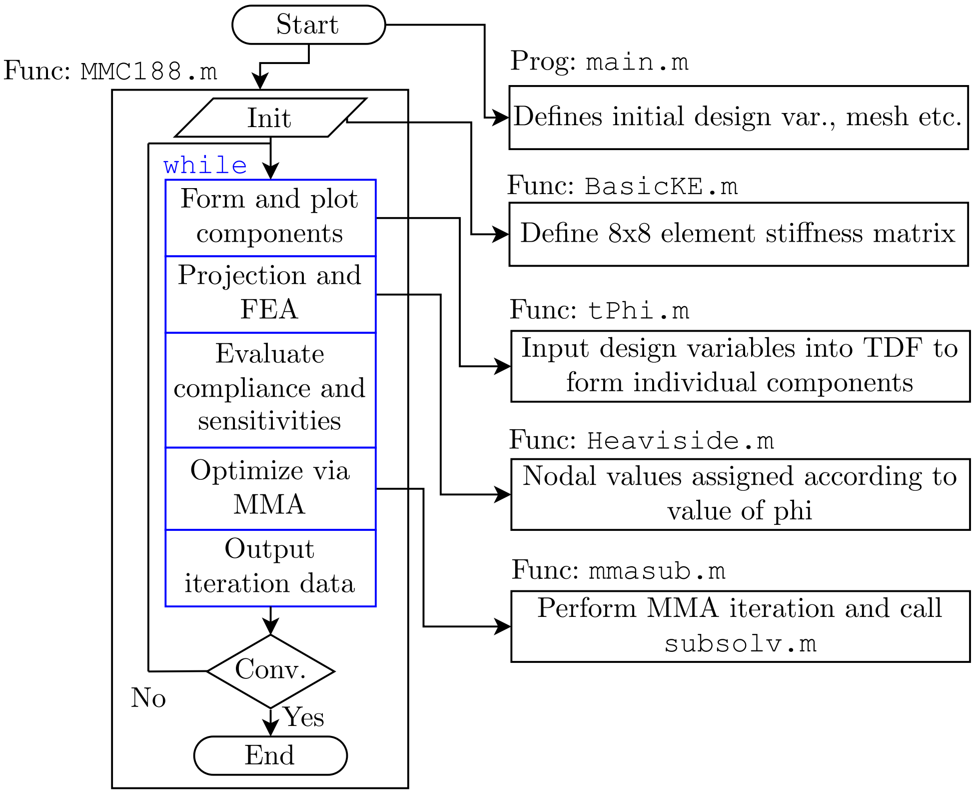

Figure 5.2. Pseudo-code of the 188-line MATLAB code by Zhang et al. (2016).

After plotting, the components are projected onto the FE-grid using `Heaviside.m`. A finite-element analysis is carried out. The results from FE are used to evaluate compliance and the sensitivities through finite difference approximations. The data is passed to `mmasub.m`. After outputting the iteration data to the command window, if the result has converged or the maximum number of iterations is surpassed, the program stops.

5.3 FEA Modifications

The academic codes often supplied with papers on topology optimization offer a great way of learning about the approach, as well as a good starting point for additions. In this section, several modifications to the code in Zhang et al. (2016) are presented.

5.3.1 Isoparametric Elements

Because of the ease of implementation, isoparametric elements are implemented instead. These may also reduce difficulty if XFEM needs implementation later. The implementation follows Cook et al. (2002) with the following additions to the code.

- Constitutive matrix, $\mathbf{C}$, for isotropic materials with a plane stress assumption from (Cook et al., 2002, p. 94).
- Strain-displacement matrix, $\mathbf{B}$, based on (Cook et al., 2002, pp. 207-208).
- Numerical integration procedure for element stiffness matrix, $\mathbf{K_e}$, following pseudo-code in (Cook et al., 2002, p. 212).

To use orthotropic materials, an orthotropic constitutive matrix is implemented as detailed in the next subsection.

5.3.2 Orthotropic Constitutive Matrix

To treat orthotropic materials, the following additions are made to the code.

- Plane stress-reduced constitutive matrix, $\mathbf{Q}$, for the 1-2 (material) coordinate system (Jones, 1999, p. 72).
- Transformation matrix, $\mathbf{T}$, given by (Jones, 1999, p. 75). To save computational time the inverse, $\mathbf{T}^{-1}$, is solved symbolically once, and written into another function.
- Transformed plane stress-reduced constitutive matrix, $\bar{\mathbf{Q}} = \mathbf{T}^{-1}\mathbf{Q}\mathbf{T}^{-T}$ for the xy (cartesian) coordinate system (Jones, 1999, p. 77).

Thus, $\mathbf{K_e}$ can be obtained for orthotropic element properties and with the same integration procedure as for isotropic properties.

5.3.3 Stiffness and Stress Computation

With the constitutive matrices defined, the stiffness and stress computation is briefly presented. From the projected nodal densities, $\mathbb{H}_\rho$, the penalized element density ${\boldsymbol{\rho}_\mathbf{p}}^e$ is defined in Eq. (5.5).

$$ {\boldsymbol{\rho}_\mathbf{p}}^e = \frac{\sum_{n=1}^{4} \left(\mathbb{H}_\rho^{e,n}\right)^2}{4} \tag{5.5} $$

Here superscript e and n denotes the element number and corresponding nodes respectively. With this penalized density, the scaled element stiffness matrix is computed as the following.

$$\mathbf{K_{e,s}}^e = \mathbf{K_e}^e \boldsymbol{\rho_p}^e \tag{5.6}$$

Here, the element stiffness matrix, $\mathbf{K}_e$, is defined using the orthotropic constitutive matrix, $(\bar{\mathbf{Q}}(\boldsymbol{\theta}^e))$, which depends on the element angle. The scaled element stiffness matrix is used to formulate the global stiffness matrix $\mathbf{K}$, used to solve the system of equations for the displacements. When displacements are obtained, strains can be computed as in Eq. (5.7) (Cook et al., 2002, p. 230).

$$\boldsymbol{\epsilon_{xy}} = \mathbf{Bu} \tag{5.7}$$

The stresses and strains can be related to the 1-2 (material) coordinate system (Eq. (5.8) by (Jones, 1999, p. 77)) for strength calculation.

$$\boldsymbol{\sigma_{xy}} = \bar{\mathbf{Q}}\boldsymbol{\epsilon_{xy}} \tag{5.8a}$$

$$\boldsymbol{\sigma_{12}} = \mathbf{T}\boldsymbol{\sigma_{xy}} \tag{5.8b}$$

Next, the input material properties are defined.

5.4 Material Parameters

To use the orthotropic elements implemented, as well as a failure criterion, material parameters are needed. Additive manufacturing has many process parameters, which highly affect the measured material properties. Therefore, material parameters measured from an AM process are sought. The continuous fiber AM machine available at Aalborg University is an Anisoprint Composer A4. Material properties from this specific printer is sought to be used in this work.

For orthotropic materials, material parameters in the material coordinate (1-2) system are sought. This coordinate system follows the definition in Fig. 5.3.

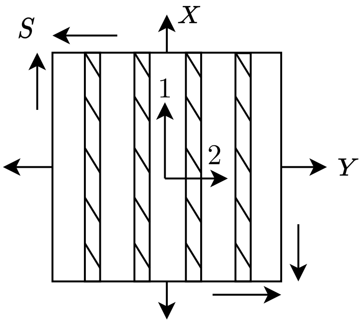

Figure 5.3. Parameters in the material coordinate system. Inspired from Jones (1999).

For strength considerations, five parameters are sought if the material exhibits different properties in tension and compression. These are also marked on Fig. 5.3 as X, Y and

S where the two former are differentiated between tension and compression by indices 't' and 'c'.

Gadegaard and Thuesen (2022) did a partial material characterization of the continuous fiber composite using the Composer A4. Because of printing errors and disagreement with the test standard, the transverse tensile strength, Y_t, did not accurately represent the true strength. Furthermore, three of the material parameters, G, X_c and S, were not tested, and based on other sources. While Gadegaard and Thuesen (2022) used a PA matrix, these sources used PLA, PETG and a short-fiber reinforced PA for the parameters, respectively. Gadegaard and Thuesen (2022) recommend a more thorough testing of the continuous fiber composite.

Since the work of Gadegaard and Thuesen (2022), Anisoprint have changed their matrix material to PETG. However, the datasheet only contains E_1, X_t, X_c and ν_{12} (Anisoprint, 2022). From an e-mail correspondence with Anisoprint, the data in Tab. 5.1 apply.

Parameter	**Value**	**Unit**
E_1	57	[GPa]
E_2	4.1	[GPa]
ν_{12}	0.4	[-]
G	0.4	[GPa]
X_t	775	[MPa]
X_c	237	[MPa]
Y_t	20	[MPa]
Y_c	20	[MPa]
S	15	[MPa]

Table 5.1. CFC-PETG Material parameters supplied by Anisoprint.

These material parameters are implemented in the code and used in this work.

6 | Component Description

The main concern using the MMC framework is the component parametrization since these are the 'building blocks' of the topology. Therefore design freedom, constraint handling, etc. depends on the component description. This chapter seeks to investigate different component descriptions starting by describing and evaluating existing component parametrizations. From the evaluation, a component formulation is selected, implemented and tested in the code.

6.1 Component Review

In this section, component descriptions are investigated to form a basis for evaluation in Sec. 6.2. The investigated components are general descriptions and thereby not constructed for orthotropic fiber material.

6.1.1 Skeleton Representation

The skeletal representation of components is used in the original framework and 188-line MATLAB code (Guo et al., 2014) (Zhang et al., 2016). Skeleton representation is shape construction from a medial axis, here defined as $f(x')$. Hence, components are constructed from center coordinates (x_0, y_0), rotation to global coordinate system θ, a medial axis $f(x')$, and a width function $d(x')$ which is exemplified in the following.

In general, skeletal descriptions use the coordinate transformation defined in Eq. (6.1). This transformation is also used by other descriptions in Sec. 6.1.2 and Sec. 6.1.3.

$$\begin{Bmatrix} x' \\ y' \end{Bmatrix} = \begin{bmatrix} cos(\theta) & sin(\theta) \\ -sin(\theta) & cos(\theta) \end{bmatrix} \begin{Bmatrix} x - x_0 \\ y - y_0 \end{Bmatrix} \tag{6.1}$$

In the original works of Guo et al. (2014) and Zhang et al. (2016), a straight medial axis is used to form the TDF as by Eq. (6.2a) with either Eq. (6.2b) or Eq. (6.2c) incorporated.

$$\phi(x, y) = \left(\frac{x'}{L}\right)^p + \left(\frac{y'}{f(x')}\right)^p - 1 \tag{6.2a}$$

$$f(x') = 2t \tag{6.2b}$$

$$f(x') = \frac{t_1 + t_2 - 2t_3}{2L^2} x'^2 + \frac{t_2 - t_1}{2L} x' + t_3 \tag{6.2c}$$

$$f(x') = a x'^2 d(x') \tag{6.2d}$$

Further works of Guo et al. (2016) incorporated curved medial axis as in Eq. (6.2d) and extended the TDF to account for arbitrary axis and width function given in Eq. (6.3).

$$\phi(x,y) = \min\left((d(x'))^2 - (y' - f(x'))^2, (L_1 + x')(L_2 - x')\right) \tag{6.3}$$

The level-sets of the exemplified TDF's are depicted in Fig. 6.1.

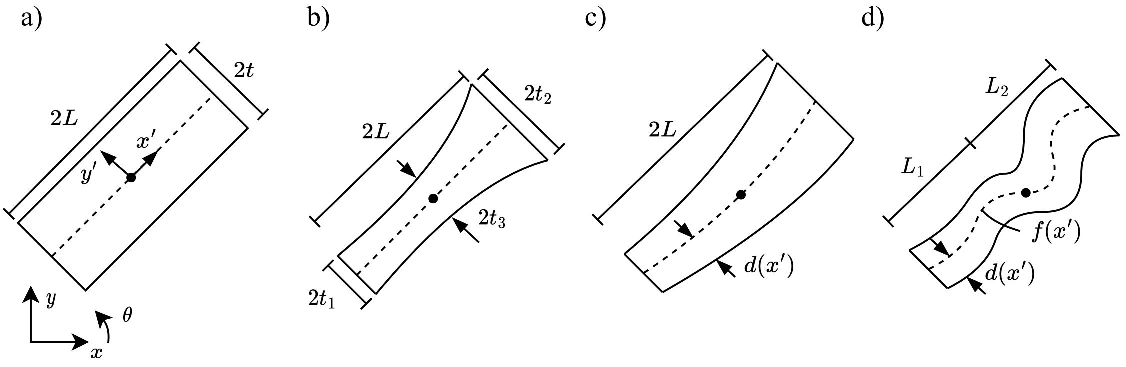

Figure 6.1. Sketched skeleton components: a) Rectangular by Eq. (6.2b) b) Varying width by Eq. (6.2c) c) Curved and varying width by Eq. (6.2d) d) Arbitrary functions by Eq. (6.3).

The concept of skeleton representations with other implementations is further investigated in the following subsections.

6.1.2 Piecewise Geometric Primitives

The construction of a component from piecewise geometric primitives is originally implemented by Norato et al. (2015) using a signed distance formulation instead of a level-set. This was also implemented in Smith and Norato (2021) as presented for orthotropic materials in Sec. 3.3. Further, Deng and Chen (2016) use this formulation combined with endpoint description given in Sec. 6.1.3 to form inter-component hinge joints and Liu and Du (2021) expands the formulation to account for nonuniform thickness. The idea of piecewise geometric primitives is here exemplified by combining two semi-circles and a bar with nonuniform thickness, hence the TDF is defined as Eq. (6.4).

$$\phi(x,y) = \begin{cases} t_1 - \sqrt{(x'+L)^2 + y'^2}, & \text{if } x' < -L \\ \frac{t_1+t_2-2t_3}{2L^2}x'^2 + \frac{t_2-t_1}{2L}x' + t_3 - \sqrt{y'^2}, & \text{if } -L \leq x' \leq L \\ t_2 - \sqrt{(x'-L)^2 + y'^2}, & \text{if } x' > L \end{cases} \tag{6.4}$$

A depiction of the level-set is given in Fig. 6.2 where $t_1 = t_2 = t_3$ would equal the commonly used piecewise bar component, presented under Sec. 6.1.3.

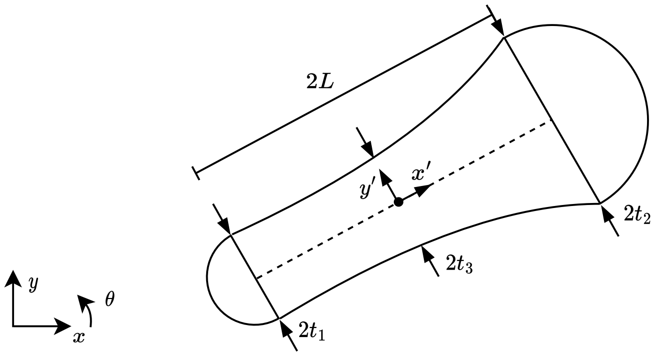

Figure 6.2. Sketched level-set of piecewise component.

The use of piecewise geometric primitives has, as previously described, been combined with the endpoint description, presented next.

6.1.3 Endpoint Descriptions

The endpoint component description uses two independent points in the design domain and a specified relation between these to form a TDF. The simplest relation is linear, depicted in Fig. 6.3, and is used combined with the piecewise construction in Norato et al. (2015), Smith and Norato (2021) and Deng and Chen (2016). A more complex relation is the Absolute Nodal Coordinate Formulation (ANCF) from Otsuka et al. (2023). This method uses position and cross sectional direction at the endpoints to form a cubic polynomial, depicted in Fig. 6.4.

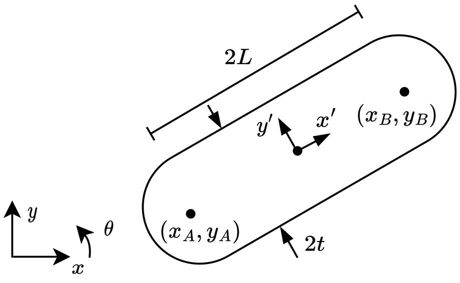

Figure 6.3. Piecewise bar defined from endpoints.

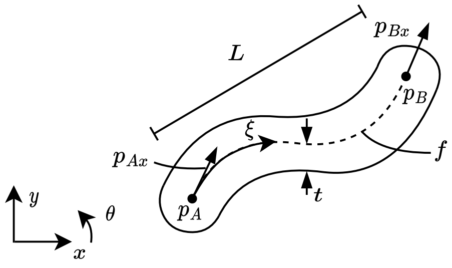

Figure 6.4. ANCF component.

The TDF corresponding to Fig. 6.3 and Fig. 6.4 are further described in the following.

Piecewise Bar

The piecewise bar can be constructed by the conversion from coordinates to geometric parameters as in Eq. (6.5).

$$2L = \sqrt{(x_B - x_A)^2 + (y_B - y_A)^2} \tag{6.5a}$$

$$\theta = \tan^{-1}\left(\frac{y_B - y_A}{x_B - x_A}\right) \tag{6.5b}$$

$$x_0 = \frac{x_B + x_A}{2} \tag{6.5c}$$

$$y_0 = \frac{y_B + y_A}{2} \tag{6.5d}$$

Utilizing these conversions the TDF of a piecewise bar is constructed by Eq. (6.4) where $t = t_1 = t_2 = t_3$ for uniform thickness.

ANCF Component

The ANCF method use the endpoints $\mathbf{p_A} = [x_A, y_A]^T$ and $\mathbf{p_B} = [x_B, y_B]^T$ combined with the gradient vectors $\mathbf{p_{Ax}}$ and $\mathbf{p_{Bx}}$ to form a skeletal polynomial formulation as in Eq. (6.6) (Otsuka et al., 2023). Here $\mathbf{S}(\mathbf{x}, L)$ is a shape function given from the length $L = ||\mathbf{p_B} - \mathbf{p_A}||$ and component coordinate ξ.

$$\mathbf{f} = \mathbf{S}(\xi, L)\mathbf{e} \tag{6.6a}$$

$$\mathbf{e} = \left[\mathbf{p_A}^T, \mathbf{p_{Ax}}^T, \mathbf{p_B}^T, \mathbf{p_{Bx}}^T\right]^T \tag{6.6b}$$

Using these definitions the TDF of an ANCF component can be defined by the distance function in Eq. (6.7).

$$\phi(x, y) = t - \min||\mathbf{f} - \mathbf{x}|| \tag{6.7}$$

From this, a cubically curved component is defined from nodal coordinates and a uniform thickness t. With a cubic component as reference, arbitrary curved components are further investigated.

6.1.4 B-spline, NURBS and Bezier curves

The B-spline, non-uniform rational B-spline (NURBS) and Bezier curves are all curve descriptions interpolated from multiple control coordinate points. Due to the similarities of these methods only the B-spline is detailed in the following, but the concept is general. The concept is to form a curve $\mathbf{f}(u)$ from the control points $\mathbf{p}^j$ as in Eq. (6.8). Here $N^{j,k}$ is the basis function associated with the j^{th} control point and of order k. Further, u is the intrinsic variable along the curve. The definition of $N^{j,k}$ is where B-splines and Bezier curves differ.

$$\mathbf{f}(u) = \sum_{j=1}^{N_c} N^{j,k}(u)\mathbf{p}^j \tag{6.8}$$

From these curves two approaches are proposed. In Zhang et al. (2017b) and Zheng and Kim (2020) the curves are used as component edge descriptions as depicted in Fig. 6.5 utilizing B-spline and NURBS respectively. To avoid curve intersection, the control points are reformulated from freely defined to being defined from center coordinates, relative angle and distance meaning $\mathbf{p}^j(x_c, y_c, \theta, d_j)$. By this formulation an inside-outside function is used as the TDF.

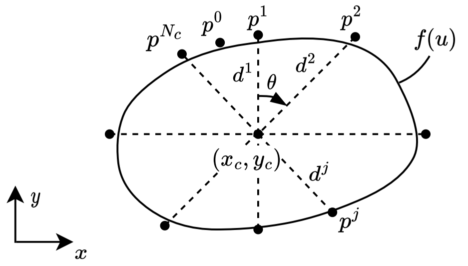

Figure 6.5. Curves as component edge.

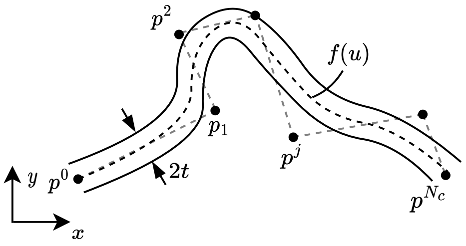

Figure 6.6. Curves as skeleton.

Another formulation, depicted in Fig. 6.6, is proposed by Zhu et al. (2021) and Shannon et al. (2022) where Bezier curves are utilized. In this approach the curve is used as a skeleton representation and a TDF is formed by Eq. (6.9).

$$\phi(x, y) = t - \min||\mathbf{f}(u) - \mathbf{x}|| \tag{6.9}$$

An alternative use of the NURBS curve as a skeleton is described in the following.

6.1.5 Time Series MMC (TSMMC) with NURBS Skeleton

Another component suggested in Li et al. (2023) is a further development of the NURBS curve as skeleton, where the progression of the curve and varying thickness is computed in a time domain. The component is firstly constructed by computing the NURBS curves $\mathbf{f}(t)$ and $r(t)$ which is time dependent placement and thickness accordingly, as defined in Eq. (6.10). Here j refers to the control point and N^j to the number of control points.

$$\mathbf{f}(t) = \frac{\sum_{j=1}^{N^j} N^{j,k}(t) w^j \mathbf{p}^j}{\sum_{j=1}^{N^j} N^{j,k}(t) w^j} \tag{6.10a}$$

$$r(t) = \frac{\sum_{j=1}^{N^j} N^{j,k}(t) \bar{w}^j r^j}{\sum_{j=1}^{N^j} N^{j,k}(t) \bar{w}^j} \tag{6.10b}$$

Having the placement curve defined as $\mathbf{f}(t) = [x(t), y(t)]^T$, the domain definition as $\mathbf{x} = [x, y]^T$ and the time interval in $t = [t_0 : t_n]$, a moment-TDF can be formed as in Eq. (6.11).

$$\tau(\mathbf{x}, t) = (r(t))^2 - (x(t) - x)^2 - (y(t) - y)^2 \tag{6.11}$$

Thereby, the TDF can be defined as in Eq. (6.12), where $\alpha_t = t_n - t_0$ and p is a tuning parameter.

$$\phi(x, y) = \frac{1}{p} \ln \left(\frac{1}{\alpha_t} \int_{t_0}^{t_n} e^{p\tau(\mathbf{x},t)} \mathrm{d}t \right) \tag{6.12}$$

From this definition a component, depicted in Fig. 6.7, is constructed.

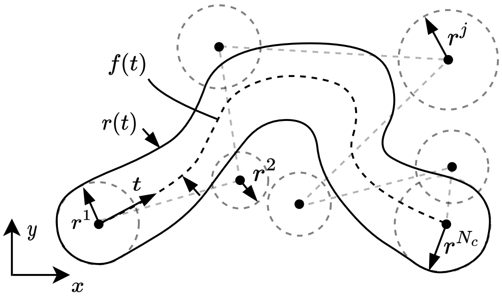

Figure 6.7. TSMMC component.

With the TSMMC component, the review is concluded. All component descriptions are evaluated in the next section.

6.2 Evaluation

As stated in the chapter introduction, the component description defines design freedom, constraint handling, etc. To form component evaluation criteria, an extension of these claims, combined with description desires, are given in a prioritized list. The prioritization is directly related to the numeration in Tab. 6.1.

1. **Intra-component fiber placement** - This criteria evaluates the relation of component and fiber geometry where a close resemblance or obvious relation is sought e.g. fibers placed parallel to skeleton.
2. **Manufacturing constraints** - Evaluated from similarities to design variables e.g. directly parameterized component length L or skeleton curvature.
   a) **Minimum length**
   b) **Maximum curvature**
   c) **Minimum separation distance** - specified as change of component thickness
3. **Design freedom** - Defined as the ability to form arbitrary geometries where a straight component is used as basis for evaluation.
4. **Robustness** - Evaluated as the sensitivity of geometric change by a perturbation on a design variable. Further, component self-overlap is considered.
5. **Ease inter-component fiber continuity** - Evaluated from possible directly defined C^1 continuity at component ends.

↓ Component / Criteria →	**1**	**2.a**	**2.b**	**2.c**	**3**	**4**	**5**
Skeleton	$\oplus$	$\oplus$	$\oplus$	$\oplus$	$\ominus$	$\oplus$	$\ominus$
Piecewise primitives	$\oplus$	$\oplus$	$\oplus$	$\ominus$	$\ominus$	$\oplus$	$\ominus$
Endpoint bar	$\oplus$	$\oplus$	$\oplus$	$\oplus$	$\ominus$	$\oplus$	$\ominus$
ANCF	$\oplus$	$\oplus$	$\oplus$	$\oplus$	$\oplus$	$\odot$	$\oplus$
Spline curves as edge	$\ominus$	$\odot$	$\odot$	$\odot$	$\oplus$	$\odot$	$\ominus$
Spline curves as skeleton	$\oplus$	$\oplus$	$\oplus$	$\oplus$	$\oplus$	$\ominus$	$\oplus$
TSMMC	$\oplus$	$\oplus$	$\oplus$	$\ominus$	$\oplus$	$\ominus$	$\oplus$

Table 6.1. Component evaluation where $\oplus$ and $\ominus$ is positive and negative respectively, and $\odot$ is neutral or unknown.

From Tab. 6.1 skeleton, piecewise primitives and endpoint bar descriptions are discarded due to the restriction of design freedom by straight components. Further, the arbitrary skeletons are discarded by being continuous in x', meaning unable to form e.g. a circle. The spline curves as edge description is discarded due to uncertainty of intra-component fiber placement. From the description, fibers could either be placed straightly through the component or offset from the edge and none of these idea alleviates the relation to manufacturing constraints. The TSMMC component is discarded since arbitrarily varying thickness is undesired and not utilizing this property equals the spline curve as skeleton component. This component however suffers from stability issues caused by sensitivity to polynomial degree and possible skeleton self-overlap. This leaves the ANCF which is evaluated as positive in all criteria except unknown robustness. Thereby, the ANCF component is the basis for implementation.

6.3 ANCF Component Implementation

This section introduces the ANCF component parametrization and how a density and orientation field is constructed from this. These fields are used to compute stiffness and volume used in the optimization formulation.

The ANCF was initially a beam element formulation used in FEA for large deformation and multibody system problems in Shabana (2014). However as described in Sec. 6.1.3 the formulation is used as a curved skeleton description by Otsuka et al. (2023) who construct a component from the skeleton $\mathbf{f}$ and a thickness t.

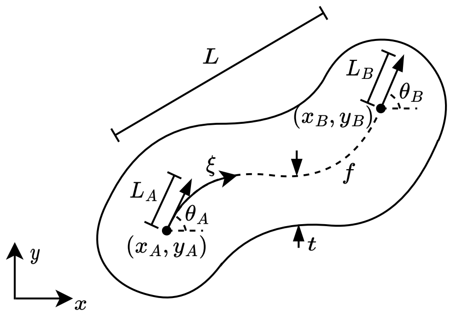

Figure 6.8. ANCF component definitions.

Depicted in Fig. 6.8 is the parametrization, skeleton curve and thickness. The relation between these is used to form the density- and orientation fields, as detailed in the following.

6.3.1 Parametrization and Skeleton Curve Construction

The design variables of the ANCF component are identified as the endpoint coordinates (x_A, y_A), (x_B, y_B) and corresponding angles at these points θ_A and θ_B. To further enhance formability of the ANCF component, this report introduces endpoint orientation vector scalability L_A and L_B. Lastly the thickness t is needed to form the TDF and therefore included in the design variable vector $\mathbf{d}$ as in Eq. (6.13) where c denotes the component number and N_c the number of components.

$$\mathbf{d}^c = \begin{bmatrix} x_A^c & y_A^c & \theta_A^c & L_A^c & x_B^c & y_B^c & \theta_B^c & L_B^c & t^c \end{bmatrix} \tag{6.13a}$$

$$\mathbf{d} = \begin{bmatrix} \mathbf{d}^1 & \mathbf{d}^c & \mathbf{d}^{N_c} \end{bmatrix}^T \qquad c = [1 : N_c] \tag{6.13b}$$

From these design variables the skeleton curve is constructed according to Shabana (2014) where the distance between the endpoints as in Eq. (6.14) is needed.

$$L^c = \sqrt{(x_B^c - x_A^c)^2 + (y_B^c - y_A^c)^2} \tag{6.14}$$

The shape function matrix $\mathbf{S}$ is constructed to account for endpoint coordinates and their gradients, hence the angles are rewritten to scaled coordinate gradients as in Eq. (6.15).

$$x_{Ax}^c = L_A^c \cos(\theta_A^c) \quad y_{Ax}^c = L_A^c \sin(\theta_A^c) \quad x_{Bx}^c = L_B^c \cos(\theta_B^c) \quad y_{Bx}^c = L_B^c \sin(\theta_B^c) \tag{6.15}$$

To match the entries of the shape function, the vector of nodal coordinates $\mathbf{e}$ is formed as in Eq. (6.16).

$$\mathbf{e}^c = \begin{bmatrix} x_A^c & y_A^c & x_{Ax}^c & y_{Ax}^c & x_B^c & y_B^c & x_{Bx}^c & y_{Bx}^c \end{bmatrix}^T \tag{6.16}$$

The shape function matrix $\mathbf{S}$ given in Eq. (6.17) is computed along the component axis with the component variable $\xi = [0, 1]$ going from point A to B. The component variable ξ is numerically discretized into N_s segments and the segments are numerated as $s = [1 : N_s]$.

$$\mathbf{S}(\xi, L^c) = \begin{bmatrix} 1 - 3\xi^2 + 2\xi^3 & 0 \\ 0 & 1 - 3\xi^2 + 2\xi^3 \\ L^c(\xi - 2\xi^2 + 3\xi^3) & 0 \\ 0 & L^c(\xi - 2\xi^2 + 3\xi^3) \\ 3\xi^2 - 2\xi^3 & 0 \\ 0 & 3\xi^2 - 2\xi^3 \\ L^c(\xi^3 - \xi^2) & 0 \\ 0 & L^c(\xi^3 - \xi^2) \end{bmatrix}^T \tag{6.17}$$

From the vector of nodal coordinates and shape function matrix, the skeleton curve $\mathbf{f}$ is computed as in Eq. (6.18). Here $f_x^c(\xi)$ and $f_y^c(\xi)$ denotes the x and y sets of the curve respectively.

$$\mathbf{f}^c(\xi) = \begin{bmatrix} f_x^c(\xi) \\ f_y^c(\xi) \end{bmatrix} = \mathbf{S}(\xi, L^c)\mathbf{e}^c \tag{6.18}$$

Numerically the curve $\mathbf{f}^c(\xi)$ is constituted by a series of coordinates caused by the discretization of ξ. Therefore a specific coordinate on the curve is denoted $\mathbf{f}^{c,s}$ which for $s = [1 : N_s]$ constitutes the full curve. The notation of c being a component counter and s a segment of component c is used throughout this report.

6.3.2 Density field

In Otsuka et al. (2023) the TDF of a component is described as a minimum distance function between the skeleton curve and nodal grid point. To avoid time consuming distance computations the TDF description in Li et al. (2023) is utilized as in Eq. (6.19). Here the TDF of every curve segment is firstly computed and the segments are then combined by a max operator to form the component as depicted in Fig. 6.9 and Fig. 6.10 using $s = 40$.

$$\phi_\rho^{c,s} = t^2 - (f_x^{c,s} - x)^2 - (f_y^{c,s} - y)^2 \tag{6.19a}$$

$$\phi_\rho^{c} = \max(\phi_\rho^{c,1}, ..., \phi_\rho^{c,s}, ..., \phi_\rho^{c,N_s}) \qquad s = [1 : N_s] \tag{6.19b}$$

From the individual component TDF, ϕ_ρ^c, the full structure TDF is formed as in Eq. (6.20). Utilizing the max operator to form the structure cause non-differentiability, however numerical evidence show no effect of this according to Zhang et al. (2016).

$$\phi_\rho = \max(\phi_\rho^{1}, ..., \phi_\rho^{c}, ..., \phi_\rho^{N_c}) \qquad c = [1 : N_c] \tag{6.20}$$

The structure assembly of two components is depicted in Fig. 6.11. Having the full structure TDF, the level-set of this TDF is projected onto a fixed nodal grid to form the density field $\mathbb{H}_\rho$. This is computed by the smoothed Heaviside function in Eq. (6.21) repeated from Sec. 5.1.3.

$$\mathbb{H}_\rho = \begin{cases} 1, & \phi_\rho > \epsilon \\ \frac{3(1-\alpha)}{4}\left(\frac{\phi_\rho}{\epsilon} - \frac{{\phi_\rho}^3}{3\epsilon^3}\right) + \frac{1+\alpha}{2}, & -\epsilon \leq \phi_\rho \leq \epsilon \\ \alpha, & \phi_\rho < -\epsilon \end{cases} \tag{6.21}$$

The density field is shown in Fig. 6.12.

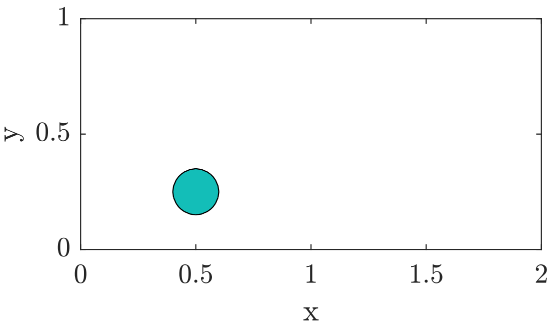

Figure 6.9. Zero contour of $\phi_\rho^{i,k}$, $k = 1$.

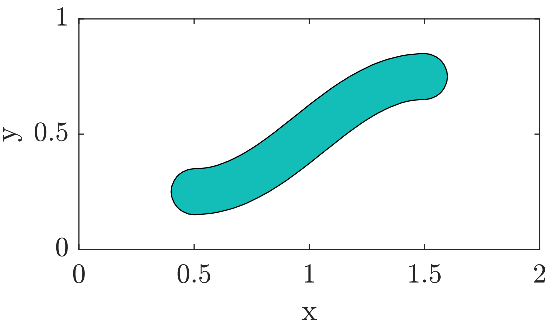

Figure 6.10. Zero contour of ϕ_ρ^{i}, $i = 1$.

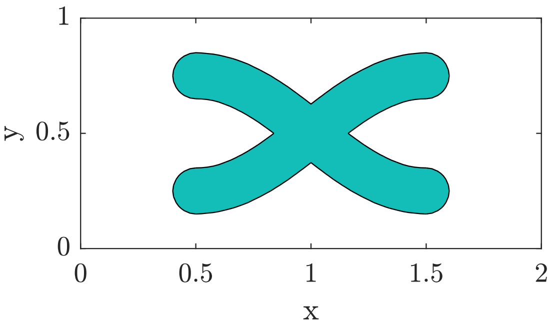

Figure 6.11. Zero contour of ϕ_ρ.

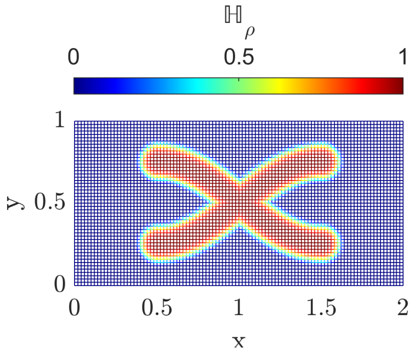

Figure 6.12. Nodal values of $\mathbb{H}_\rho$.

Having the density field of the structure defined by $\mathbb{H}_\rho$, the fiber orientation field needs to be defined, covered in the next subsection.

6.3.3 Orientation Field

The intra-component fiber placement and orientation requires both placement definition, corresponding to the density field on the fixed grid, and assigning orientation to every element within. To the authors knowledge, such projection has not been done in the literature with curved components. Therefore, a projection similar to the projection of the densities is created.

Orientation Projection Concept

The computation of orientations is chosen to be parallel to the skeleton curve as was the reference from the component evaluation in Sec. 6.2. From this choice the concept of orientation projection is depicted in Fig. 6.13, where the segment angle $\theta^{c,s}$ is projected to every element within the level-set of $\phi_\theta^{c,s}$, depicted circular. From this concept, the shape of the segment-wise level-set and handling of overlapping level-sets needs to be defined.

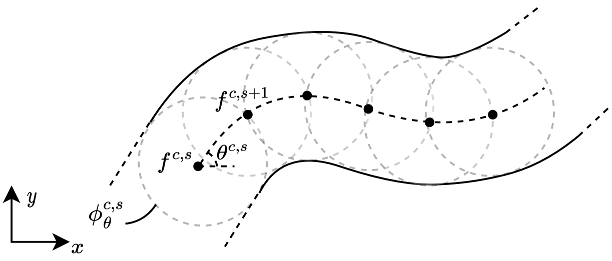

Figure 6.13. Orientation projection concept.

In Appendix B, multiple approaches are investigated. This includes overlapping area definitions as averaging of vectorized angles (presented here), averaging of direct angles (seen in Fig. B.2) and recursive segment-wise projection (presented in Appendix B.2). Of these definitions the averaging are continuous and differentiable and the recursive projection is not. Further, the use of circles, ellipses and semi-circles as segment-wise level-sets are investigated. The investigated approaches are evaluated according to the following.

Approach Evaluation

Due to the uniform thickness parametrization of components, and due to a desired constant fiber volume fraction along the length of components, equidistance of fibers placed within each component is needed. Equidistance of fibers can be geometrically ensured by curve parallelism. Parallelism is in this work defined by the two statements listed below according to Mokhtarzadeh et al. (2024).

1. Two parallel curves have a constant distance between every point along their length.
2. Two curves, in the same plane, are parallel if they have identical tangent vectors at corresponding points along their length.

These definitions are utilized to evaluate the orientation field approaches in Appendix B. All approaches investigated fulfill the first constant distance definition by increasing the number of segments. However the second definition cannot be ensured if the segment angles are averaged in overlapping areas. Further, recursive projection of $\theta^{c,s}$ to an area between $s-1$ and s will cause nonidentical tangents. Hence, only the semi-circle approach with recursive projection fulfills the demand of curve parallelism and thereby constant fiber volume fraction. This is however conditional by not allowing greater thickness than the radius of curvature of the skeleton curve and the problem is depicted in Fig. B.5.

Since maintaining differentiability of the component description is of priority, an error evaluation between the defined 'correct' recursive semi-circle projection and the averaging of vectorized angles using circles is made. The assessment of this evaluation is described in Appendix B.1.4 and with the prospect of efficient computation by analytic sensitivities, the differentiable averaging of vectorized angles using circles will be used throughout this report. The approach is detailed in the following.

Detailed Implementation

A segment-wise orientation TDF $\phi_\theta^{c,s}$ is formed as in Eq. (6.22). This orientation TDF is similar to the density TDF with the change of expanding the level-set by half the element diagonal length, $L_{e,diag}$. This is to project orientations to intermediate density elements on the component boundary.

$$\phi_\theta^{c,s} = \left(t + L_{e,diag}\right)^2 - \left(f_x^{c,s} - x\right)^2 - \left(f_y^{c,s} - y\right)^2 \tag{6.22}$$

The component orientation TDF ϕ_θ^c is then computed by Eq. (6.23).

$$\phi_\theta^c = \max(\phi_\theta^{c,1}, ..., \phi_\theta^{c,s}, ..., \phi_\theta^{c,N_s}) \qquad s = [1 : N_s] \tag{6.23}$$

These TDF's are used to define the projection placements on the fixed grid. The orientation projected to elements in each segment is defined by the coordinates $\mathbf{f}^{c,s}$ and $\mathbf{f}^{c,s+1}$. Since the distances between these points are not constant along the length of the curve, the vectorized orientations needs normalized when computing an average of the overlapping areas. Hence, the lengths in Eq. (6.24) are computed to normalize the orientation vector entries in Eq. (6.25) and Eq. (6.26).

$$L_{\theta}^{c,s} = \sqrt{(f_x^{c,s+1} - f_x^{c,s})^2 + (f_y^{c,s+1} - f_y^{c,s})^2} \tag{6.24}$$

From the segment-wise placements defined by the TDF the orientation vector entries are projected to element centers on the fixed grid as in Eq. (6.25) and Eq. (6.26). The smoothed Heaviside functions used are constructed similar to the density field. The non-zero parameter α_θ is to avoid singularity in Eq. (6.31) and is set to 10^{-3}. The segment counter projection $\mathbb{H}_{\theta,count}^{c,s}$ in Eq. (6.27) is constructed to count whether an orientation is projected to an element or not. This is further used to average the element orientations.

$$\mathbb{H}_{\theta,x}^{c,s} = \begin{cases} \frac{f_x^{c,s+1} - f_x^{c,s}}{L_\theta^{c,s}}, & \phi_\theta^{c,s} > \epsilon_\theta \\ \frac{f_x^{c,s+1} - f_x^{c,s}}{L_\theta^{c,s}} \left(\frac{3}{4} \left(\frac{\phi_\theta^{c,s}}{\epsilon} - \frac{(\phi_\theta^{c,s})^3}{3\epsilon^3} \right) + \frac{1}{2} \right), & -\epsilon_\theta \leq \phi_\theta^{c,s} \leq \epsilon_\theta \\ \alpha_\theta, & \phi_\theta^{c,s} < \epsilon_\theta \end{cases} \tag{6.25}$$

$$\mathbb{H}_{\theta,y}^{c,s} = \begin{cases} \frac{f_y^{c,s+1} - f_y^{c,s}}{L_\theta^{c,s}}, & \phi_\theta^{c,s} > \epsilon_\theta \\ \frac{f_y^{c,s+1} - f_y^{c,s}}{L_\theta^{c,s}} \left(\frac{3}{4} \left(\frac{\phi_\theta^{c,s}}{\epsilon} - \frac{(\phi_\theta^{c,s})^3}{3\epsilon^3} \right) + \frac{1}{2} \right), & -\epsilon_\theta \leq \phi_\theta^{c,s} \leq \epsilon_\theta \\ 0, & \phi_\theta^{c,s} < \epsilon_\theta \end{cases} \tag{6.26}$$

$$\mathbb{H}_{\theta,count}^{c,s} = \begin{cases} 1, & \phi_\theta^{c,s} \geq \epsilon_\theta \\ \frac{3}{4} \left(\frac{\phi_\theta^{c,s}}{\epsilon} - \frac{(\phi_\theta^{c,s})^3}{3\epsilon^3} \right) + \frac{1}{2}, & -\epsilon_\theta \leq \phi_\theta^{c,s} \leq \epsilon_\theta \\ 0, & \phi_\theta^{c,s} < -\epsilon_\theta \end{cases} \tag{6.27}$$

The number of orientations projected to a given element in segment overlapping areas, is then computed by the Kreisselmeier-Steinhauser function in Eq. (6.28) to avoid zero values causing singularities in Eq. (6.29) and Eq. (6.30) (Lund, 2023).

$$\mathbb{H}_{\theta,count}^{c} = \frac{1}{P} \log \left(e^P + e^{P \sum_{s=1}^{N_s} \mathbb{H}_{\theta,count}^{c,s}} \right) \tag{6.28}$$

A parameter value of $P = 50$ yields approximately 1% error if only one orientation is projected and will be used. Thereby, the element-wise average orientation vector entries are computed by Eq. (6.29) and Eq. (6.30).

$$\mathbb{H}_{\theta,x}^{c} = \frac{\sum_{s=1}^{N_s} \mathbb{H}_{\theta,x}^{c,s}}{\mathbb{H}_{\theta,count}^{c}} \tag{6.29}$$

$$\mathbb{H}_{\theta,y}^{c} = \frac{\sum_{s=1}^{N_s} \mathbb{H}_{\theta,y}^{c,s}}{\mathbb{H}_{\theta,count}^{c}} \tag{6.30}$$

From the orientation vector entries the component orientation field $\mathbb{H}_\theta^c$ is defined in Eq. (6.31) where atan2 is utilized for consistency of orientations (Ukil et al., 2011).

$$\mathbb{H}_\theta^c = \text{atan2}\left(\frac{\mathbb{H}_{\theta,y}^c}{\mathbb{H}_{\theta,x}^c}\right) \tag{6.31}$$

Using these definitions a single segment orientation field is depicted in Fig. 6.14 and a component orientation field in Fig. 6.15. The assembly of component orientation fields to a structure orientation field is given by Eq. (6.32).

$$\mathbb{H}_{\theta,struc}^c = \begin{cases} \mathbb{H}_\theta^c, & \phi_\theta^c \geq 0 \\ \mathbb{H}_{\theta,struc}^{c-1}, & \phi_\theta^c < 0 \end{cases} \qquad c = [1 : N_c] \tag{6.32}$$

For simplicity of notation the structure orientation field $\mathbb{H}_{\theta,struc}^{N_c}$ is denoted $\mathbb{H}_\theta$ throughout the rest of this report. The structure orientation field for two components is depicted in Fig. 6.16.

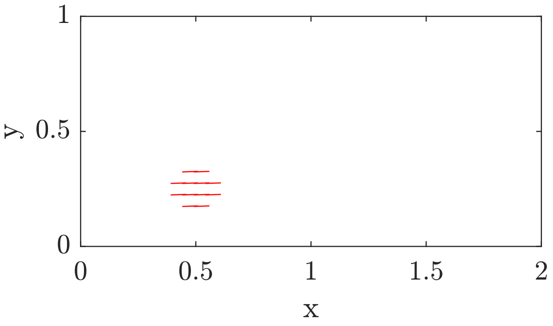

Figure 6.14. Depiction of first segment orientation field $\mathbb{H}_\theta^{c,1}$.

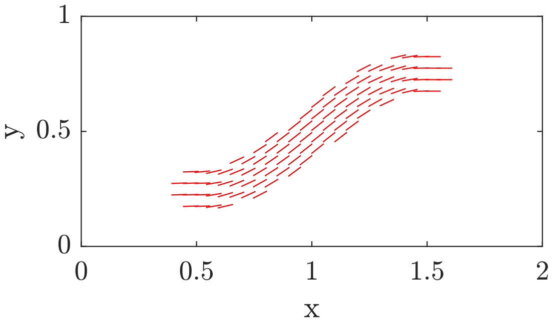

Figure 6.15. Component orientation field $\mathbb{H}_\theta^c$.

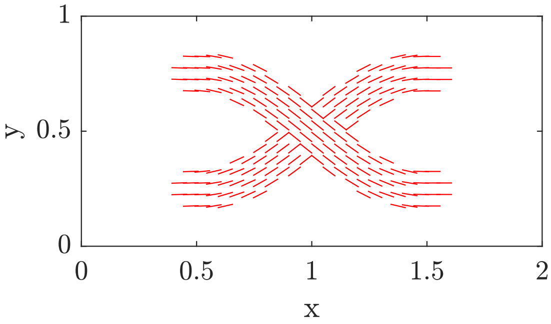

Figure 6.16. Structure orientation field $\mathbb{H}_\theta$.

By the full structure orientation field and the density field from Sec. 6.3.2 all inputs for stiffness computation presented in Sec. 5.3.2 are projected element-wise to the fixed grid as needed. Hence, the relation from design variables to FEA is achieved.

6.4 Optimization Formulation

As a starting point for structural optimization the general optimization formulation of compliance minimization subject to a volume constraint is used, as in Eq. (6.33). Here the ANCF parametrization constituting the design variables **d** are related to the stiffness matrix **K** as described throughout Sec. 6.3 and Sec. 5.3 in that order.

$$\underset{\mathbf{d}}{\text{Minimize}} \qquad C = \mathbf{u}^T\mathbf{K}\mathbf{u} \tag{6.33a}$$

$$\text{Subject to} \qquad V - \bar{V} \leq 0 \tag{6.33b}$$

To solve this structural optimization problem the frequently used MMA solver from Svanberg (1987) and Svanberg (2007) is used. To use gradient-based solvers such as the MMA, sensitivities of the objective and constraints need to be computed. Analytical sensitivities have not been pursued, since the main goal of this report is a proof of concept and not efficient computation. Therefore, semi-analytic sensitivities are computed approximately by finite differences as stated in Eq. (6.34) (Zhang et al., 2016). Here d denotes the entry in the design variable vector **d**.

$$\frac{\partial C}{\partial \mathbf{d}^d} = -\mathbf{u}^T\frac{\partial \mathbf{K}}{\partial \mathbf{d}^d}\mathbf{u} \approx -\mathbf{u}^T\frac{\Delta \mathbf{K}}{\Delta \mathbf{d}^d}\mathbf{u} \tag{6.34a}$$

$$\frac{\partial V - \bar{V}}{\partial \mathbf{d}^d} = \frac{\partial V}{\partial \mathbf{d}^d} \approx \frac{\Delta V}{\Delta \mathbf{d}^d} \tag{6.34b}$$

For stiffness and volume gradient computation by central differences, the reader is referred to Appendix C.1. Using this optimization formulation, numerical tests are performed.

6.5 Numerical Testing

This section presents numerical studies on the implemented ANCF component formulation. First, the test case used is briefly presented. Results obtained are presented and interpreted, and modifications implemented. Finally, necessary further work to ensure manufacturability of the structure is summarized based on the results.

6.5.1 Test Case and Parameters Used

To compare results with the literature, and later versions of the same code, a benchmark example is used. Fig. 6.17 shows dimensions and boundary conditions for the 'short cantilever beam' example used in e.g. Zhang et al. (2016) and Guo et al. (2016), which is also used here.

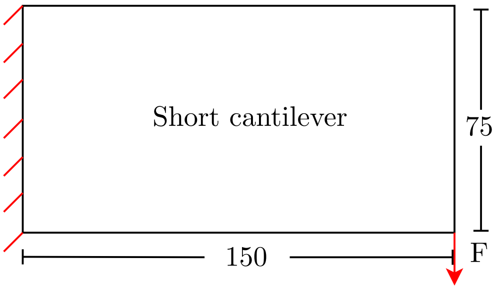

Figure 6.17. Short cantilever beam test case. Red indicating boundary conditions. Dimensions in mm.

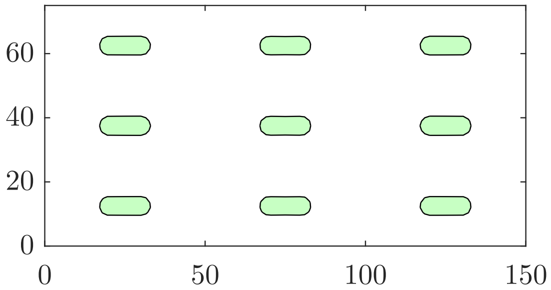

Figure 6.18. Initial design variables.

The initial guess for the test cases is seen in Fig. 6.18. Initially, the components are kept small to avoid prescribing the final structure as suggested by Smith and Norato (2021). The discretization and other parameters may be varied. For these tests, parameters are given in Tab. 6.2.

Parameter	**Value**
Discretization	100 × 50 elements
Load	40 N
Move limits	$\{x_A, y_A, x_B, y_B\} = 10\,\text{mm}$ $\{\theta_A, \theta_B\} = 22.5°$ $\{L_A, L_B\} = 0.5$ $t = 6\,\text{mm}$
Gradient perturbations	$\{x_A, y_A, x_B, y_B\} = 3\,\text{mm}$ $\{\theta_A, \theta_B\} = 10°$ $\{L_A, L_B\} = 0.1$ $t = 0.5\,\text{mm}$

Table 6.2. Parameters used in these tests.

The next subsection presents the results obtained using these parameters.

6.5.2 Results from Short Cantilever Beam

The results from running the code are seen in Figs. 6.19 to 6.22.

Fig. 6.19 shows the component plot, i.e. all components where overlapping ones are visible. Fig. 6.20 shows the iteration history of the compliance and the volume constraint. The total number of iterations is 3000, however, the iteration history plot is limited to 1000 iterations.

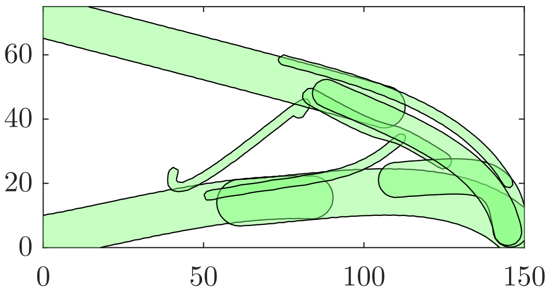

Figure 6.19. Component plot.

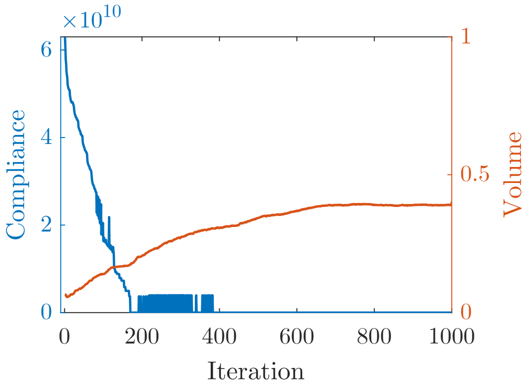

Figure 6.20. Iteration history.

In Appendix D.1.1, Fig. 6.20 in the range of 400-1000 iterations is repeated, due to the large change in compliance from 0-400 iterations. Fig. 6.21 shows the structure plot. This plot corresponds to the printed part, i.e. each black line represents a fiber and fibers are depicted with the minimum separation distance. The green is matrix material.

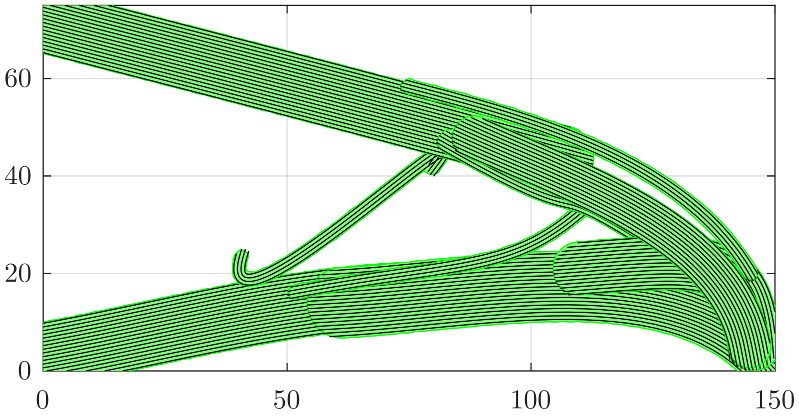

Figure 6.21. Structure plot.

Finally, Fig. 6.22 shows the element-wise angles used for finite element analysis, projected from the component.

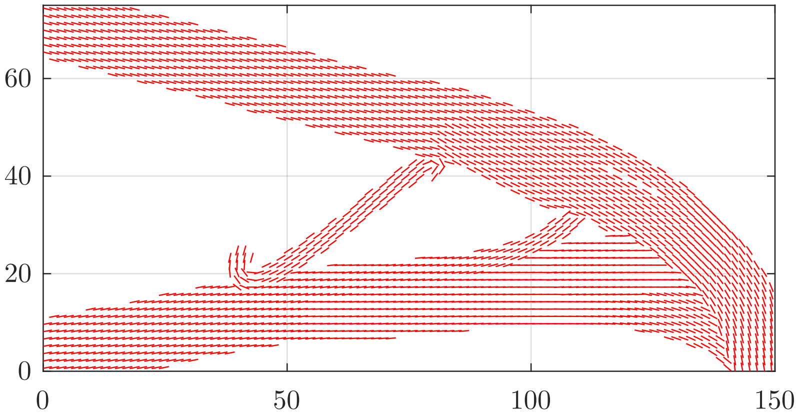

Figure 6.22. Element-wise angles used for FEA.

As is seen from the figures, the fibers near the loading are aligned with the direction of the load, and the components near the supports are spaced at a maximum distance from each other. Further, the volume constraint of ≤ 0.4 is met.

It is interesting to note that the lowest structural member, formed by two components, has much curvature. In another result obtained by a slightly different formulation of the stiffness interpolation (explained in the following) a more straight lower member is found. This result is seen in Appendix D.1.2. By comparing the compliance, the result presented here is lower with both of the stiffness scalings used.

It is noted that the results presented before are based on changing the low-density elements to an isotropic formulation, and the high-density elements on an orthotropic formulation. The reason and the used formulation is explained in the next subsection.

6.5.3 Low-density Element Effects

Since the ersatz material model is used, the stiffness of elements not part of the structure is scaled down, but not to zero since that would cause singular stiffness when components do not overlap. For simplicity in the code, all elements were given the same orthotropic properties, and were all assigned an angle. Shown in this subsection, the orientation of low-density elements have a significant effect on the resulting structure, and as conclusion the 'background grid' should have an isotropic formulation as in the results presented previously.

Fig. 6.23 and Fig. 6.24 show the short cantilever beam example with the same parameters except 'background elements' are given angles 0° and 90° respectively.

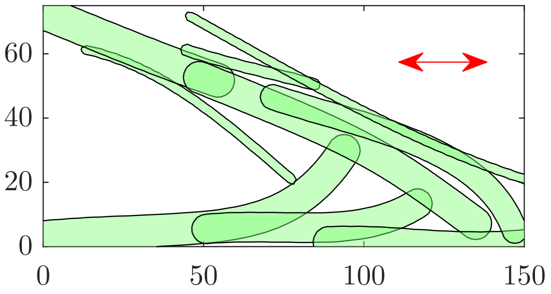

Figure 6.23. Component plot at a 1000 iterations. Low density element angle is 0°.

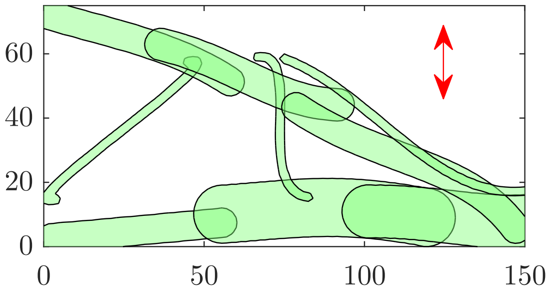

Figure 6.24. Component plot at a 1000 iterations. Low density element angle is 90°.

It is clear from these results that, because of the angles of the low-density elements, preferential member directions exist.

Schmidt et al. (2020) did SIMP-based topology optimization with element-wise fiber orientation optimization. The optimization results for different initial fiber angles were compared. It was found that when all angles were given the same value, the resulting member directions or fiber angle directions preferred angles similar to the initial value. This effect is similar to what is observed for this work in Figs. 6.23 to 6.24.

To mitigate the effects, Schmidt et al. (2020) used randomized angles, which yielded different topologies but with similar compliance, when succesive random initial guesses were given. For this work however, it is expected that with an angle-randomized low-density background grid, the preferential effects will still be present at a local level.

Thus, instead, the background grid is made isotropic using Eq. (6.35) inspired by the modified SIMP scheme in Sigmund (2007).

$$\mathbf{C}^e = \mathbf{C_{iso}} + \boldsymbol{\rho}^e(\bar{\mathbf{Q}}^e - \mathbf{C_{iso}}) \tag{6.35}$$

Here, $\mathbf{C}$ is the used constitutive matrix for the current element, $\mathbf{C_{iso}}$ the isotropic constitutive matrix, and $\bar{\mathbf{Q}}$ the orthotropic constitutive matrix. $\boldsymbol{\rho}^e$ is the unpenalized element density calculated from Eq. (6.36) based on the Heaviside projection, Eq. (6.21).

$$\boldsymbol{\rho}^e = \frac{\sum_{n=1}^{4}(\mathbb{H}_{\rho}^{e,n})}{4} \tag{6.36}$$

$\mathbf{C_{iso}}$ is based on a Young's modulus of $E = 1 \times 10^{-6}$ MPa, exclusively to prevent a singular stiffness matrix. With this stiffness scaling the parameter α in the Heaviside function in Eq. (6.21) is set to zero, which means that the 'background grid' gets no orthotropic properties. This formulation removes the low-density element orientation dependency from the results.

6.5.4 Verification Studies

Before including the manufacturing constraints, sanity checks are performed using the strain energy density and the principal stress directions. Stiffness-optimal designs have uniform strain energy density as far as the constraints allow them to (Pedersen, 2000). Further, minimum compliance is obtained when the stiffest material direction is aligned with the principal stress direction (Pedersen, 1989).

Thus, the element strain energy density, $\mathbf{w}^e$ can be computed for visualization as in Eq. (6.37) by Lund (2023).

$$\mathbf{w}^e = \frac{1}{2}\frac{(\mathbf{u}^e)^T\mathbf{K_e}^e\mathbf{u}^e}{V^e} \tag{6.37}$$

Here, $\mathbf{u}^e$ is the element displacement vector, $\mathbf{K}_e$ the element stiffness matrix and V^e the element volume. For the result presented in Figs. 6.19 to 6.22, Fig. 6.25 shows the element-wise strain energy density.

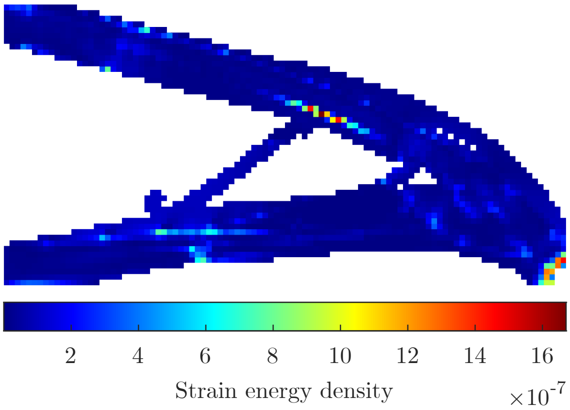

Figure 6.25. Element-wise strain energy density (topology is the same as Fig. 6.19).

It is noted that the six elements closest to the load introduction are removed, since the load is not included as load-equivalent. The element-wise strain energy density is somewhat uniform throughout the part. This result thus verifies that the topology and fiber layout follows expectations.

In Appendix D.1.3, the principal stress directions and a difference plot between the projected fiber angles and the angle of the largest principal stress is plotted. Larger differences are observed where the two principal stresses are approximately equal (where structural members meet), following intuition. It is shown that the difference between the angle of the maximum principal stress and the projected angle is for the most part $\leq 5°$. This result thus verifies that the fiber layout follows expectations.

6.5.5 Further Work

In this chapter, a component review was conducted and the ANCF component implemented. Preliminary tests show that optimization is working as intended.

Notable is that the manufacturing constraints of minimum fiber separation distance is partially implemented and minimum feature size is implemented by the component parametrization and projection as follows.

- Minimum fiber separation distance, D_{sep}, inside a component, is implemented by placing fibers intra-component and with equidistance of D_{sep}.
- Minimum feature size, W_e, is implemented by a lower bound on the component thickness t.

From the structure in Fig. 6.21 however, it is clear further development of the code is necessary to make manufacturable parts. This includes fiber length and curvature constraints. Furthermore, the only interaction mechanism for different components is overlap, and there is no inter-component continuity of the fibers. Component interaction and constraints are treated in the next chapter. It is noted that part of the components in Fig. 6.21 overlap the design domain boundary, which essentially cuts fibers as they are currently defined. This aspect will not be treated in the following chapters.

7 Component Interaction and Constraints

The main purpose of this chapter is introduction of the manufacturing constraints to the optimization formulation. This includes formulating a method for component interaction, both to enhance inter-component fiber continuity at endpoints and not allowing overlapping components. Lastly a minimum fiber length constraint and maximum fiber curvature constraint are needed. Since the interaction and constraint formulations are constructed with reference to the ANCF component parametrization, the presented formulations are novel approaches unless stated otherwise.

7.1 Inter-Component Relations

The purpose of this section is to describe inter-component relations needed for constraint computation and endpoint continuity. Hence, only parameters and bookkeeping are presented.

For clarification, the design variables used for inter-component relations are the endpoint coordinates, orientations and component thicknesses depicted in Fig. 7.1.

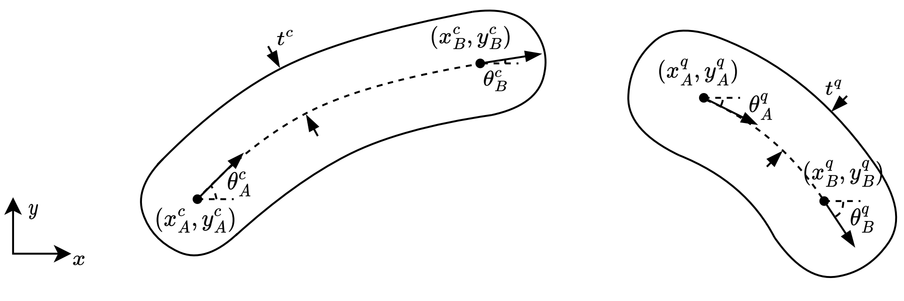

Figure 7.1. Component relation parameters.

Here $c = [1 : N_c - 1]$ denotes the component number and $q = [c + 1 : N_c]$ the other components defined subsequently to c. The definition of q is to specifically avoid computing relations twice. The counting and bookkeeping of component relations is conceptually depicted with four components in Fig. 7.2. The depiction refers to Eq. (7.1), but the bookkeeping is identical for orientation and thickness relations.

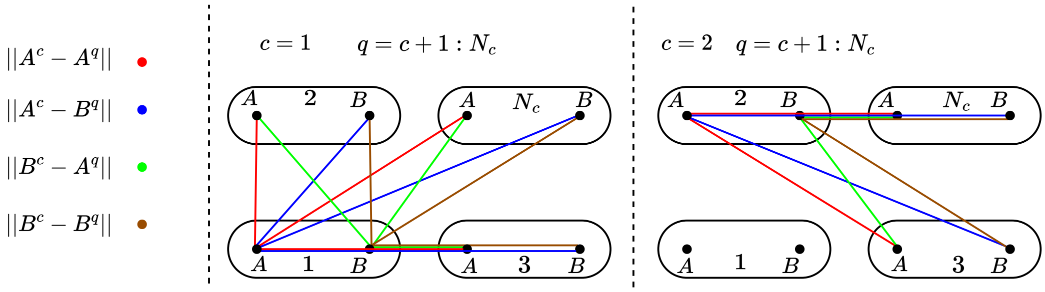

Figure 7.2. Depiction of relation counting.

For the first example depicted for $c = 1$, the entry $||A^c - A^q||$ in $\mathbf{l}^1_{int}$ is a 1×3 vector. Hence, $\mathbf{l}^1_{int}$ becomes a 1×12 vector with the lengths depicted. Thereby, the inter-component relation of endpoint distances is defined for a component in Eq. (7.1).

$$\mathbf{l}^c_{int} = \Big[||A^c - A^q|| \quad ||A^c - B^q|| \quad ||B^c - A^q|| \quad ||B^c - B^q||\Big] \qquad q = [c+1 : N_c] \tag{7.1}$$

From the counting of c and q, $\mathbf{l}^2_{int}$ neglects the first defined component and is therefore only a 1×8 vector. The component distances are then assembled as in Eq. (7.2) which contain every endpoint distance.

$$\mathbf{l}_{int} = \Big[\mathbf{l}^1_{int} \quad \mathbf{l}^c_{int} \quad \mathbf{l}^{N_c-1}_{int}\Big] \qquad c = [1 : N_c - 1] \tag{7.2}$$

The second relation is endpoint orientation differences as in Eq. (7.3) and assembled in Eq. (7.4).

$$\boldsymbol{\theta}^c_{int} = \Big[|\theta^c_A - \theta^q_A| \quad |\theta^c_A - \theta^q_B| \quad |\theta^c_B - \theta^q_A| \quad |\theta^c_B - \theta^q_B|\Big] \qquad q = [c+1 : N_c] \tag{7.3}$$

$$\boldsymbol{\theta}_{int} = \Big[\boldsymbol{\theta}^1_{int} \quad \boldsymbol{\theta}^c_{int} \quad \boldsymbol{\theta}^{N_c-1}_{int}\Big] \qquad c = [1 : N_c - 1] \tag{7.4}$$

The last relation is the distance at which endpoint segment come into contact, given by the sum of endpoint radii as in Eq. (7.5) and Eq. (7.6).

$$\mathbf{l}^c_{contact} = \Big[t^c + t^q \quad t^c + t^q \quad t^c + t^q \quad t^c + t^q\Big] \qquad q = [c+1 : N_c] \tag{7.5}$$

$$\mathbf{l}_{contact} = \Big[\mathbf{l}^1_{contact} \quad \mathbf{l}^c_{contact} \quad \mathbf{l}^{N_c-1}_{contact}\Big] \qquad c = [1 : N_c - 1] \tag{7.6}$$

By the vector assemblies presented, the entries of $\mathbf{l}_{int}$, $\boldsymbol{\theta}_{int}$ and $\mathbf{l}_{contact}$ match each other meaning the entry number gives the relation between the same endpoints. For further description, the entries are matched by the relation counter $r = [1 : N_r]$, where the total number of relations, N_r, is constructed by the component counters c and q.

7.2 Inter-Component Endpoint Continuity

One of the main advantages of using the MMC framework for continuous fiber topology optimization, is the predefined intra-component fiber continuity. However the potential of inter-component fiber continuity has not been achieved as described in Sec. 3.3. Further, the ANCF component parametrization is evaluated in Sec. 6.2 to ease inter-component continuity as is achieved by endpoint descriptions in Deng and Chen (2016) and Otsuka et al. (2023). However, these use equality constraints to ensure endpoint connection which causes the component connections to be predefined. This is undesirable in the context of this work. This section seeks to describe how to utilize the potential of inter-component fiber continuity by endpoint continuity.

7.2.1 Endpoint Continuity Concept

The conceptual approach is depicted in Fig. 7.3, where components move and morph freely according to the objective, until endpoint segments contact described by $\mathbf{l}_{int} = \mathbf{l}_{contact}$. When this distance requirement is fulfilled, a non-physical contribution driving equality of endpoint coordinates and orientations is implemented as depicted.

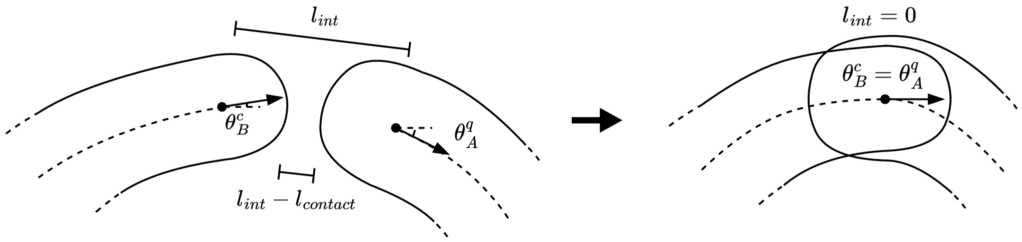

Figure 7.3. Component relations used for enhancing endpoint continuity.

A formulation for this non-physical geometric contribution is further investigated.

7.2.2 Formulation

The requirements for the geometric contribution, is to be described in the full domain and approximate zero when endpoint segments do not touch. Further, a smooth transition from zero to a given value for gradient computation is desired. From these demands the distance relation functions $\mathbf{f}^r_{dist}$, contributing to coordinate equality, are constructed with reference to a Gaussian distribution in Eq. (7.7).

$$\mathbf{f}^r_{dist} = -e^{-\left(\frac{2\mathbf{l}^r_{int}}{\mathbf{l}^r_{contact}}\right)^2} \tag{7.7}$$

The orientation equality is formulated in combination with the distance relation function. Therefore, the orientation relation function $\mathbf{f}^r_\theta$ in Eq. (7.8) is orientation penalization. Again, every term in Eq. (7.8) is constructed with reference to a Gaussian distribution. The first term is to only account for orientations when endpoint segments contact and the second term to yield value zero at orientation differences of 0, π and 2π.

$$\mathbf{f}^r_\theta = e^{-\left(\frac{2\mathbf{l}^r_{int}}{\mathbf{l}^r_{contact}}\right)^2} \left(-e^{-(\boldsymbol{\theta}^r_{int})^2} - e^{-(\boldsymbol{\theta}^r_{int}-\pi)^2} - e^{-(\boldsymbol{\theta}^r_{int}-2\pi)^2} + 1\right) \tag{7.8}$$

From the distance and orientation functions, the combined relation function, $\hat{\mathbf{f}}^r$, is computed in Eq. (7.9).

$$\hat{\mathbf{f}}^r = \mathbf{f}^r_{dist} + \mathbf{f}^r_\theta \tag{7.9}$$

To clarify the formulation in Eq. (7.9), a visualization of the function contribution is depicted. In Fig. 7.4 three different endpoint configurations are depicted. In Fig. 7.5 the function $\hat{\mathbf{f}}^r$ is depicted along the corresponding function values for the three configurations.

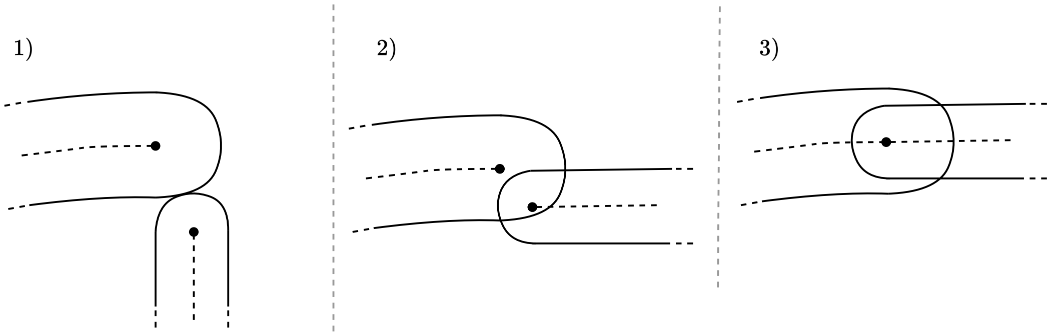

Figure 7.4. Depiction of geometric configurations corresponding to values in Fig. 7.5.

For the function depiction in Fig. 7.5, the polar coordinates $\mathbf{l}^r_{int} = [0, 15]$ and $\boldsymbol{\theta}^r_{int} = [0, 2\pi]$ are converted to Cartesian coordinates.

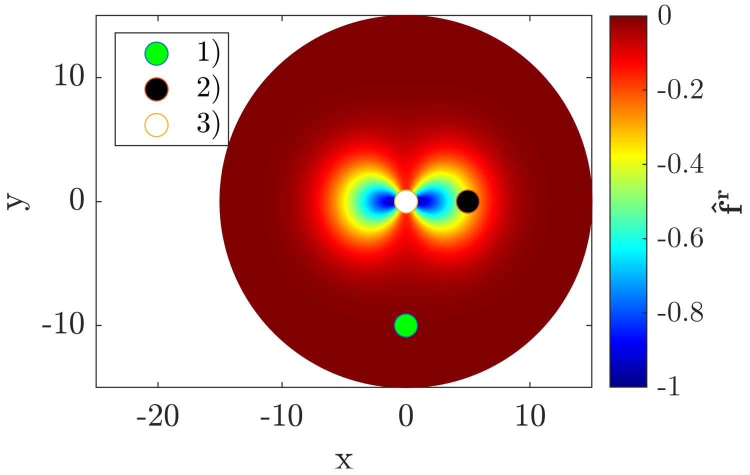

Figure 7.5. Depiction of $\hat{\mathbf{f}}^r$ in Cartesian coordinates with $\mathbf{l}^r_{contact} = 10$.

The purpose of the presented formulation is to ensure inter-component fiber continuity under the condition of the endpoint segments contacting. From Fig. 7.5 the function values for distances above $\mathbf{l}_{contact}$ approximate zero. Further, fiber continuity requires an inter-component distance of zero and orientation alignment. By the presented formulation, distance and orientation alignment is driven by minimization of the function. To account for all endpoint interactions the functions are combined by Eq. (7.10).

$$f_{int} = \sum_{r=1}^{N_r} \hat{\mathbf{f}}^r \tag{7.10}$$

The implementation of this geometric contribution in the optimization problem is described in the following.

7.2.3 Implementation in Optimization Formulation - Multi-objective

Endpoint continuity is not a necessary feature for a feasible design, but an opportunity for defining connections when endpoints are driven together by compliance minimization. Therefore implementation is not defined as a constraint, since this could potentially lock components to each other or keep endpoints separated. Another reason is the uncertainty of the number of connections formed. Since the connections should be driven by compliance, a predefined number of connections is impossible to estimate in an alternative constraint formulation. Therefore the geometric contribution is implemented in the objective inspired by penalization methods in Stolpe and Svanberg (2001).

This leads to a multi-objective problem formulation, hence a relation between the objectives needs to be defined. The initial formulation attempted was the normalized weighted sum in Eq. (7.11) (ANSYS, Inc., 2023). This formulation was chosen due to the inherent difference of objective values (Marler and Arora, 2010).

$$f_{WS} = \sum_{o=1}^{N_o} \alpha_o f_o \tag{7.11a}$$

$$\alpha_o = \frac{\frac{w_o}{|f_o|}}{\sum_{o=1}^{N_o} \frac{w_o}{|f_o|}} \tag{7.11b}$$

However, weighting problems occur, due to objective scaling of compliance dropping from approximately 10^{10} to 4 during optimization seen in Fig. 6.20, and geometric contribution objective changing in the order of 0 to -10. The formulation in Eq. (7.11) was attempted with two approaches. These two were a weighted normalization from initial function values and an adaptive approach using function values at the current iteration. Neither of these approaches proved sufficient. Using normalization from initial function values, the compliance objective contribution was negligible throughout optimization. Using adaptive normalization, the component formations were solely driven by the geometric endpoint contribution, until endpoints met. Meaning that the structure was formed by the closest endpoints interacting. This led to realization of two deficiencies of weighted sum methods stated in Marler and Arora (2010). The first being the difficulty in discerning between whether the weight factors simply compensate for function magnitudes or describes the relative weighted relations. Secondly the inability to account for the optimization progression or adaptability.

Instead of a weighted sum formulation, an adaptive and objective magnitude independent formulation is sought. Therefore, approaches related to adaptive constraint scaling in Le et al. (2010) and Oest and Lund (2017) were investigated, but these approaches refer to scaling approximates to real values of the same entities. In this approach the desire is to scale the geometric contribution entity based on convergence of the compliance entity. Another desire is, that compliance should only be further minimized by the geometric objective and not worsened. From these desires the multi-objective formulation in Eq. (7.12) is constructed.

$$f = C + w_{int}^{i} f_{int} \tag{7.12}$$

Here, w_{int}^{i} is the inter-component weight factor. This factor is used to implement the desired adaptability by the iteration counter, i, and magnitude scaling. For the formulation of w_{int}^{i}, the following requirements for the multi-objective behavior are listed.

- Initially the topology should be formed solely based on compliance minimization, thus $w_{int}^{i} = 0$ initially.
- f_{int} contribution should be subsequently increased by increasing w_{int}^{i} without compromising compliance converging to a minimum.
- w_{int} has to account for value scaling between C and f_{int}.
- w_{int} has to account for the relative weight between C and f_{int}.
- w_{int} has to converge to avoid combined objective oscillation.

From these requirements, the iteration-dependent weight factor in Eq. (7.13) is constructed. Here, C_{min} is the minimum compliance found from the first to the current iteration with the purpose of accounting for the objective scaling. Further, C_{min} converges by the compliance minimization. α_{int}^{i} is the iteration-dependent relative weighting of the objectives.

$$w_{int}^{i} = \alpha_{int}^{i} C_{min} \tag{7.13}$$

The relative weighting α_{int}^{i} is constructed to increase the f_{int} contribution without compromising the compliance objective. This is achieved by the formulation in Eq. (7.14a), where the weighting is either increased or decreased depending on the averaged relative compliance change ΔC_{avg}^{i} in Eq. (7.14b). The relative compliance change is computed over the last five iterations to account for compliance stability. The parameter $\Delta\alpha$ is the maximum perturbation on α_{int}^{i-1}. Hence, the weighting is increased or decreased depending on whether the relative compliance change is below or above $\Delta\alpha$ respectively. Further, weight limits of 0 and 2 are implemented since negative f_{int} contribution is undesired and a continuous increase would prohibit compliance convergence at C_{min}.

$$\alpha_{int}^{i} = \alpha_{int}^{i-1} + \Delta\alpha - \min\left(2\Delta\alpha, \Delta C_{avg}^{i}\right) \qquad 0 \leq \alpha_{int}^{i} \leq 2 \tag{7.14a}$$

$$\Delta C_{avg}^{i} = \frac{1}{5} \sum_{k=i-4}^{i} \frac{C^{k} - C_{min}}{C_{min}} \tag{7.14b}$$

The formulation in Eq. (7.14) accounts for the relative weighting and adaptability to compliance changes. However, convergence of α_{int}^{i} is needed to ensure convergence of the weight factor in Eq. (7.13). Convergence of α_{int}^{i} is given by the following possibilities.

- Compliance stabilizes at C_{min}. In this case $\Delta C_{avg}^{i} < \Delta\alpha$ leading to $\alpha_{int}^{i} \rightarrow 2$.
- Unstable compliance. In this case $\Delta C_{avg}^{i} > \Delta\alpha$ leading to $\alpha_{int}^{i} \rightarrow 0$.
- Compliance stabilizes at $\Delta C_{avg}^{i} = \Delta\alpha$ leading to α_{int}^{i} converging to an intermediate value $\alpha_{int}^{i} \rightarrow [0, 2]$.

Since convergence of w_{int}^i is ensured, gradient computation in the optimization formulation is neglected. Throughout the results of this report, the maximum weight perturbation $\Delta\alpha = 0.1$ corresponding to 10% is chosen. From the formulation presented, the weighting requirements are fulfilled and this approach is implemented. The results are further discussed in Sec. 7.5.4.

Since endpoint continuity is defined as an objective, absolute placement and orientation equality cannot be ensured. Further, specifications of which individual fibers to connect between the interacting components is undefined. Therefore post-processing to construct a continuous fiber in the overlapping area is needed. However, for lower endpoint continuity objective function value, less change from post-processing is needed. Therefore, for lower objective value, more conformity between analysis and manufactured model is obtained.

Next, overlap constraints are formulated taking the overlap of endpoints into account.

7.3 Overlap Constraints

The overlap constraint is essential for continuous fiber layout since multiple fibers cannot be defined in the same place both by manufacturing and computationally. However, due to endpoint continuity, an allowable endpoint overlap needs to be defined. From this the overlap definitions required are sketched in Fig. 7.6, where the green allowable overlap is defined under the conditions of component continuity as depicted.

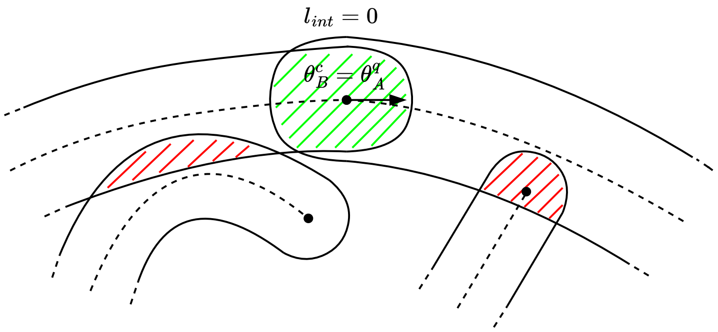

Figure 7.6. Allowable and unallowable component overlap.

Formulations to allow for the sketched endpoint overlap (green area) and not every other kind (red areas) are investigated in the following.

7.3.1 Overlap Constraint Formulation

Overlap constraint definitions have been pursued with bar components. Smith and Norato (2019) defined components with allowable endpoint overlap which, with reference to Fig. 7.6, would allow for the green area but also the red depicted to the right. Another approach, used in Sun et al. (2022), defines an allowable overlapping material surrounding the bar components. Hence, components containing fibers are completely restricted from overlapping. Lastly, Smith and Norato (2021) utilize a component density variable to define dominant components by the largest density. Thereby, component interaction is not prohibited but inferior components are cut by the dominant.

The definition sought by Fig. 7.6 is a mixture of completely prohibiting overlap as in Sun et al. (2022) and allowing endpoint overlap as in Smith and Norato (2019). However, the allowable overlap needs to be restricted to only account for endpoint connection. The mixed concept is described by Fig. 7.7.

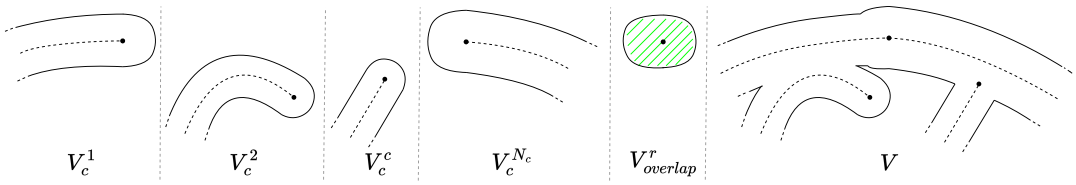

Figure 7.7. Overlap constraint concept.

Here, the volume of each component V_c^c is computed individually and should equal the volume of the structure V combined with the endpoint overlapping volumes $V^r_{overlap}$ as in Eq. (7.15). If the combination of volumes does not equal zero, the error must be equal to the sketched red area in Fig. 7.6. Thereby, the constraint is formulated as in Eq. (7.15).

$$g_{overlap} = \sum_{c=1}^{N_c} V_c^c - \sum_{r=1}^{N_r} V^r_{overlap} - V \tag{7.15}$$

The computation of each volume is given in the following.

Structure Volume V

Firstly the structure volume is computed from the density field $\mathbb{H}_\rho$ in Eq. (7.16). The density field is chosen as reference since it is already used in the volume constraint in Sec. 6.4 and to avoid complex geometric functions describing the structure.

$$V = \frac{\sum_{e=1}^{N_e} \sum_{n=1}^{4} \mathbb{H}_\rho^{e,n}(\mathbf{d})}{4WH} \tag{7.16}$$

Component Volume V_c^c

Two approaches for the component volume computation are suggested. The first being identical to the structure volume in Eq. (7.16). The other is to compute the component volume from the skeleton curve length and thickness added to the endpoint semi-circles. To maintain conformity of the structure volume and individual components, the first suggestion is chosen, where volumes are computed from their respective density fields as in Eq. (7.17). Thereby, the volume contribution from intermediate boundary densities are identical for the individual components and the structure.

$$V_c^c = \frac{\sum_{e=1}^{N_e} \sum_{n=1}^{4} \mathbb{H}_\rho^{c,e,n}(\mathbf{d}^c)}{4WH} \qquad c = [1 : N_c] \tag{7.17}$$

Endpoint Overlap Volumes $V^r_{overlap}$

The allowable endpoint overlap volumes $V^r_{overlap}$ proved tedious to implement due to only being allowed by the criteria described in the following. Two approaches have been tested, one geometric approach described in Appendix E and a discrete approach described here. The geometric approach proved insufficient due to discrepancies between geometric and element density based volume computation. This caused the optimizer to utilize this discrepancy to form infeasible overlap somewhere else in the structure as shown in Appendix E.2. Therefore the discrete element density based volume computation is implemented. The criteria needed for allowable overlapping are depicted in Fig. 7.8. As seen, the allowable overlap has to be endpoint orientation dependent causing a computational difference of whether an A-A or A-B connection is formed.

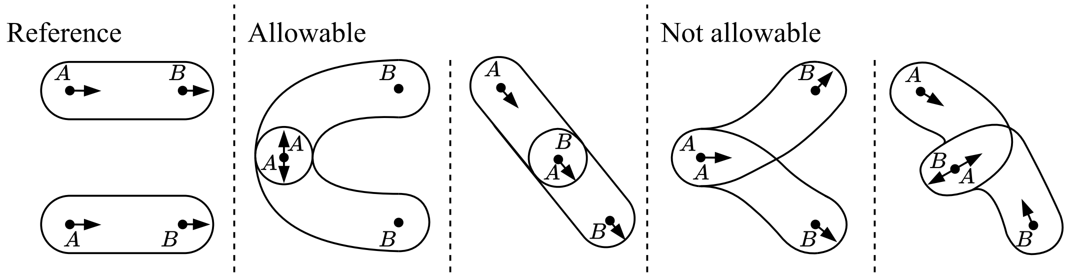

Figure 7.8. Depiction of allowable overlap from endpoint relations.

Therefore, $V^r_{overlap}$ is only computed if the following criteria are fulfilled. Here, the first criterion describes whether the endpoint segments interact and the two other criteria describe the orientation and relation dependence.

- If $\mathbf{l}^r_{int} \leq \mathbf{l}^r_{contact}$
- If A-A or B-B relation and $\frac{\pi}{2} \leq \boldsymbol{\theta}^r_{int} \leq \frac{3\pi}{2}$
- If A-B or B-A relation and $0 \leq \boldsymbol{\theta}^r_{int} \leq \frac{\pi}{2}$ or $\frac{3\pi}{2} \leq \boldsymbol{\theta}^r_{int} \leq 2\pi$

If the criteria are fulfilled, the overlapping volume is computed by forming a TDF, as in Eq. (7.18), from the two components interacting. The interacting components are numbered c and q corresponding to the relation number r. The bookkeeping of these relations are identical to the presented in Sec. 7.1. This TDF is projected to a density field $\mathbb{H}^r_{int}$ in Eq. (7.19) from which the volume is computed in Eq. (7.20).

$$\phi^r_{int} = \max\left(\phi^c_\rho, \phi^q_\rho\right) \tag{7.18}$$

$$\mathbb{H}^r_{int} = \begin{cases} 1, & \phi^r_{int} \geq \epsilon_{int} \\ \frac{3}{4}\left(\frac{\phi^r_{int}}{\epsilon_{int}} - \frac{(\phi^r_{int})^3}{3\epsilon^3_{int}}\right) + \frac{1}{2}, & -\epsilon_{int} \leq \phi^r_{int} \leq \epsilon_{int} \\ 0, & \phi^r_{int} < -\epsilon_{int} \end{cases} \tag{7.19}$$

$$V^r_{int} = \frac{\sum_{e=1}^{N_e} \sum_{n=1}^{4} \mathbb{H}^{r,e,n}_{int}}{4WH} \tag{7.20}$$

From this formulation, V^r_{int} is the volume of the two-component structure formed in relation r. Hence, the overlapping volume of relation r is computed from the difference of component-wise volumes and the two-component structure volume in Eq. (7.21). Here, V_c^c and V_c^q are reused from Eq. (7.17).

$$V^r_{overlap} = V_c^c + V_c^q - V^r_{int} \tag{7.21}$$

From these volume definitions the overlap constraint in Eq. (7.15) is implemented. However, by allowing endpoint overlap a new problem of not allowing multi-endpoint overlap is introduced.

7.3.2 Multi-Overlap Constraint

From the overlap constraint definition in Sec. 7.3.1 the volume of components are computed individually and overlapping volume of each distance relation is subtracted. This causes a counting error between the number of contacting components and the number of computed relations as illustrated by the example in Fig. 7.9. Depicted are three components overlapping in the same point, hence the individual component volumes account for the three contacting ends in red. Since inter-component relations are computed between every endpoint, three overlapping volumes are computed as depicted centered in green. Further, the same overlapping volume is computed as part of the full structure, causing a fourth volume computed. The optimizer then utilize this allowable fourth volume elsewhere causing infeasible overlap.

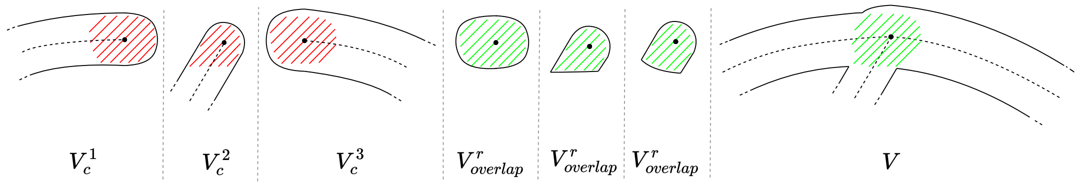

Figure 7.9. Multi-overlap problem.

Therefore, a second overlap constraint, prohibiting three or more components from overlapping at the endpoints is needed. Again the individual component density fields are utilized, here as a counter. These nodal density fields are summed to form a overlap counting field $\mathbb{H}_{overlap}$ as in Eq. (7.22).

$$\mathbb{H}^{e,n}_{overlap} = \sum_{c=1}^{N_c} \mathbb{H}^{c,e,n}_{\rho}\left(\mathbf{d}^c\right) \tag{7.22}$$

This field is used to describe whether or not a node is overlapped by three or more components by Eq. (7.23).

$$g^n_{overlap,count} = \begin{cases} 1, & \mathbb{H}^{e,n}_{overlap} \geq 3 \\ 0, & \mathbb{H}^{e,n}_{overlap} < 3 \end{cases} \tag{7.23}$$

A visualization of this is given in Fig. 7.10, where nodes given value 1 is marked green.

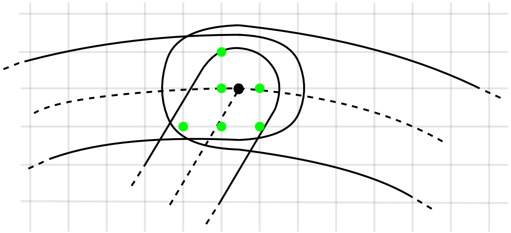

Figure 7.10. Depiction of multi-overlapped nodes.

To form a single constraint the node values are summed in Eq. (7.24).

$$g_{multioverlap} = \sum_{n=1}^{N_n} g^n_{overlap,count} \tag{7.24}$$

With this additional constraint three or more components cannot overlap and no alterations of the formulation in Sec. 7.3.1 is needed.

7.4 Minimum Fiber Length and Maximum Fiber Curvature

From the component description and intra-component fiber placement, continuous fibers are ensured parallel to the component skeleton curve. Due to this parallelism, the length and curvature extremes for all fibers within a component, are on the component edge. Hence, for minimum length and maximum curvature, only the fibers on the component edges have to be constrained, since this ensures feasibility of all fibers placed between.

7.4.1 Component Edge Description

To compute the edge lengths and curvatures, the discretized skeleton curve $\mathbf{f}^{c,s}$ from Sec. 6.3.1 is utilized. The skeleton curve is used to compute a discretized edge curve description depicted in Fig. 7.11.

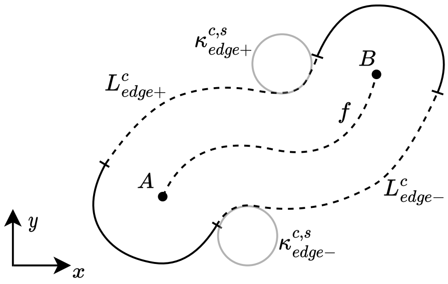

Figure 7.11. Constraint definitions from edge curve.

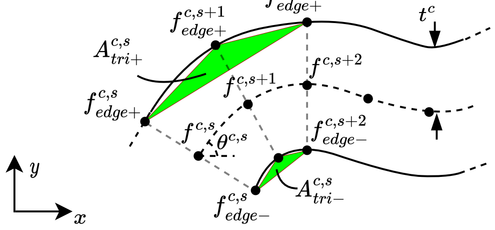

Figure 7.12. Edge curve definitions.

The edge descriptions are computed by coordinate transformation with reference to the skeleton curve using the definitions in Fig. 7.12. For the coordinate transformation, the segment angle, $\boldsymbol{\theta}^{c,s}$, is needed. The segment angle is computed as in Eq. (7.25) from the skeleton curve coordinates with the atan2 operator to avoid discontinuities at $\frac{\pi}{2}$ and $\frac{-\pi}{2}$ (Ukil et al., 2011). By computing the segment angles from coordinates, a discrepancy of the number of segments and angles occurs. Hence, the last angle is given by the design variable θ_B^c in Eq. (7.26).

$$\boldsymbol{\theta}^{c,s} = \text{atan2}\left(\frac{f_y^{c,s+1} - f_y^{c,s}}{f_x^{c,s+1} - f_x^{c,s}}\right) \qquad s = [1 : N_s - 1] \tag{7.25}$$

$$\boldsymbol{\theta}^{c,N_s} = \theta_B^c \tag{7.26}$$

With the segment angles, the coordinate transformations for edge coordinates are computed in Eq. (7.27) and Eq. (7.28). Here the edges are computed from the positive and negative component thickness t^c respectively.

$$\mathbf{f}_{edge+}^{c,s} = \mathbf{f}^{c,s} + \begin{bmatrix} cos(\boldsymbol{\theta}^{c,s}) & sin(\boldsymbol{\theta}^{c,s}) \\ -sin(\boldsymbol{\theta}^{c,s}) & cos(\boldsymbol{\theta}^{c,s}) \end{bmatrix} \begin{Bmatrix} 0 \\ t^c \end{Bmatrix} \tag{7.27}$$

$$\mathbf{f}_{edge-}^{c,s} = \mathbf{f}^{c,s} + \begin{bmatrix} cos(\boldsymbol{\theta}^{c,s}) & sin(\boldsymbol{\theta}^{c,s}) \\ -sin(\boldsymbol{\theta}^{c,s}) & cos(\boldsymbol{\theta}^{c,s}) \end{bmatrix} \begin{Bmatrix} 0 \\ -t^c \end{Bmatrix} \tag{7.28}$$

With the edge curve descriptions, the constraints are formulated.

7.4.2 Minimum Fiber Length

The fiber lengths at the component edges are computed as the sum of distances between edge curve coordinates as in Eq. (7.29). Here both the positive and negative edge are described using the ± notation but are computed separately.

$$L_{edge\pm}^{c} = \sum_{s=1}^{N_s-1} ||\mathbf{f}_{edge\pm}^{c,s+1} - \mathbf{f}_{edge\pm}^{c,s}|| \tag{7.29}$$

A desire for the minimum length constraint formulation is to account for inter-component fiber continuity as depicted in Fig. 7.13. Depicted to the left, the minimum length constraint is defined for the fibers on the component edge marked red. Thereby, every edge is constrained. When endpoint continuity occurs, depicted to the right, the length constraint on the component with the smallest thickness should be relaxed by the length of the other component. Thereby, the length of the smaller component should not be constrained.

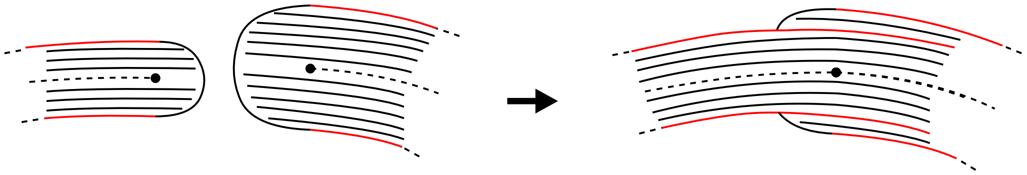

Figure 7.13. Desired inter-component fiber length constraint.

A formulation to account for this component length constraint relaxation has not been achieved. This is mainly due to the formulation having to be defined by the difficulties listed below.

- Endpoint continuity
    - Relaxation should only activate if endpoint distance is approximately zero.
    - Relaxation should only activate if endpoint orientations are aligned.
- If endpoint continuity is achieved and the thinner component becomes the thicker component, the active length constraint will change from one to the other component.
- When multiple components connect successively, the above applies to every interaction.

Due to these problems, the minimum fiber length constraint is computed without accounting for component interaction, meaning computation on every positive and negative component edge by Eq. (7.30).

$$\mathbf{g}^{c}_{length} = L_{min} - \begin{Bmatrix} L^{c}_{edge+} \\ L^{c}_{edge-} \end{Bmatrix} \tag{7.30}$$

With the minimum fiber length constraint, the maximum curvature constraint needs to be defined.

7.4.3 Maximum Fiber Curvature

Since curvature is a local entity, no component interaction is needed in this constraint formulation. The curvature of the component edges is computed for every segment by the Menger Curvature in Eq. (7.31) (Leger, 1999). Here the ± notation is used to describe both the positive and negative edge, however these are computed separately.

$$\kappa^{c,s}_{edge\pm} = \frac{4A^{c,s}_{tri\pm}}{||\mathbf{f}^{c,s}_{edge\pm} - \mathbf{f}^{c,s+1}_{edge\pm}|| \cdot ||\mathbf{f}^{c,s+1}_{edge\pm} - \mathbf{f}^{c,s+2}_{edge\pm}|| \cdot ||\mathbf{f}^{c,s+2}_{edge\pm} - \mathbf{f}^{c,s}_{edge\pm}||} \tag{7.31}$$

From Eq. (7.31), the number of computed curvatures leads to a large number of constraints, hence aggregation is utilized. Aggregation techniques are reviewed in Appendix C.2. Since the curvatures are only positive values and the constraint is a maximum value, a P-norm aggregation for each component is chosen. The P-norm is chosen since it overestimates the maximum value and therefore is a conservative approximation (Lund, 2023). Other aggregation techniques are presented in Sec. 8.2.1. Therefore the curvature is formulated as in Eq. (7.32).

$$g^{c}_{curvature} = \left(\sum_{s=1}^{N_s-2} \left(\kappa^{c,s}_{edge+}\right)^{P} + \left(\kappa^{c,s}_{edge-}\right)^{P} \right)^{\frac{1}{P}} - \kappa_{max} \tag{7.32}$$

Here, $P = 9$ is used and the maximum allowable curvature κ_{max} is given in Tab. 2.2.

With this curvature constraint, the manufacturing constraint formulations are concluded and a directly manufacturable design is expected from the solution to the optimization problem. The results using these formulations are presented in the next section.

7.5 Constrained Results

This section presents the results obtained by the constrained optimization formulation. Multiple tests are presented for investigation of constraint influence and a formulation tuning is suggested.

7.5.1 Optimization Formulation

From the additional objective of endpoint continuity, and constraint formulations presented throughout this chapter, the optimization problem in Eq. (6.33) is reformulated to Eq. (7.33).

$$\underset{\mathbf{d}}{\text{Minimize}} \quad f = C + w^i_{int} f_{int} \tag{7.33a}$$

$$\text{Subject to} \quad V - \bar{V} \leq 0 \tag{7.33b}$$

$$g_{overlap} \leq 0 \tag{7.33c}$$

$$g_{multioverlap} \leq 0 \tag{7.33d}$$

$$\mathbf{g}^c_{length} \leq 0 \qquad c = [1 : N_c] \tag{7.33e}$$

$$g^c_{curvature} \leq 0 \qquad c = [1 : N_c] \tag{7.33f}$$

The overlap constraints are both formulated as global criteria, hence only two constraint equations are needed. The length constraint, $\mathbf{g}^c_{length}$, consists of the positive and negative component edge. Hence, the number of length constraints is two times the number of components. The curvature constraints are aggregated for every component, and the number of constraint equations is therefore equal to the number of components. Sensitivities are computed similarly to Sec. 6.4 by central differences. Using the formulation in Eq. (7.33) the following results are obtained.

7.5.2 Result - Fully Constrained Formulation

The first result sought is a fully constrained structure by the complete optimization formulation in Eq. (7.33). Hence, this result serves as validation of the constraint and endpoint continuity formulations. The short cantilever beam benchmark from Sec. 6.5 is used. The resulting structure after 1000 iterations is seen in Fig. 7.14.

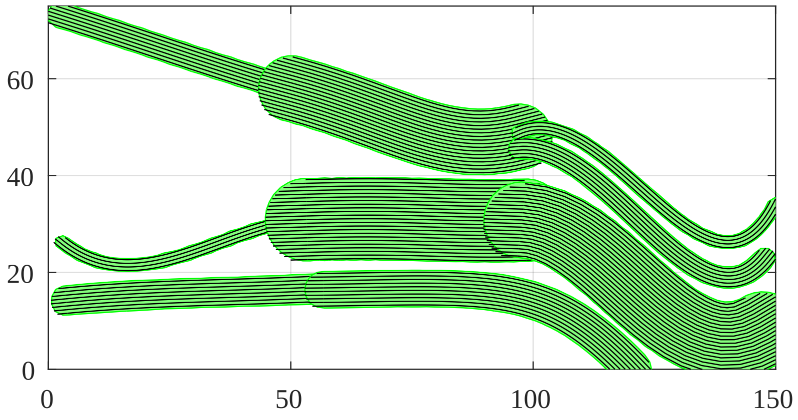

Figure 7.14. Manufacturable structure at 1000 iterations.

From apparent looks, the components placed adjacent to each other are disconnected, but this is only due to the geometric depiction and mesh size. In Appendix D.2.1 the orientation and density fields are depicted showing connections in the analysis model. From visual inspection the structure seems to be manufacturable, but to verify the individual contributions of the optimization formulation, further investigations are needed.

Firstly, convergence of the compliance objective in Fig. 7.15, is investigated. As depicted, compliance converges to a value of 17.6 from the initial value of $6 \cdot 10^{10}$. Further description of the optimization progression is given by the three distinct phases in the following.

- 0-150 iterations.
  - Enlargement of components almost without any component interactions.
- 150-400 iterations.
  - Structure forming by interacting components.
  - Highly nonlinear behavior is due to structure continuity being formed by overlapping components, but due to the overlap constraint, this is only allowable at the endpoints.
- 400-1000 iterations.
  - Structure continuity is formed from allowable endpoint overlaps and component boundary interaction on element basis by adjacent intermediate densities.
  - Considerable component movement and morphing still occurs.

Investigating the constraints, all constraints are fulfilled and the structure is therefore considered manufacturable. The global constraints (volume and overlap) are depicted in Fig. 7.16 with the length and curvature constraint of component number 5 (in the center of Fig. 7.14). Notable is the infeasible initial length constraint and feasibility reached within the initial 150 iterations where the structure is not yet formed. This is used for discussion in Sec. 7.5.3.

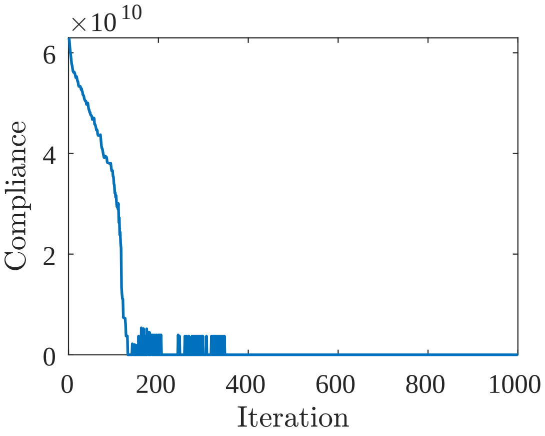

Figure 7.15. Convergence plot.

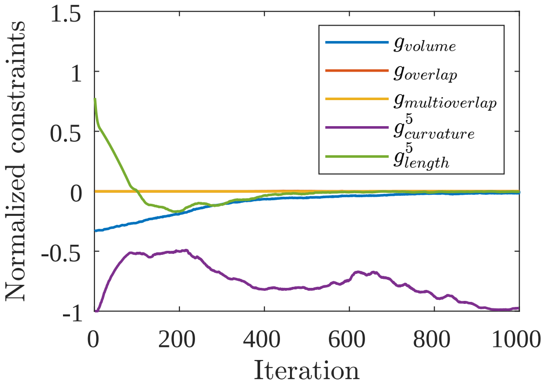

Figure 7.16. Constraint plot.

To investigate the endpoint continuity objective, the component plot showing endpoint overlaps is depicted in Fig. 7.17. From visual inspection endpoint continuity is successful by the equality of placement and orientations. Computing the difference of design variables proved this by a maximum placement and orientation deviation of 0.01 mm and 0.03 rad respectively. Hence, the endpoint continuity objective formulation is validated. In Sec. 7.2.3 it is stated, that endpoint continuity should not be achieved by compromising compliance minimization. Seen from Fig. 7.18, compliance is not increased by the introduction of the multi-objective formulation at iteration 500. Further, the weighting, w^i_{int}, converges with the compliance objective, hence the multi-objective formulation behaves as expected.

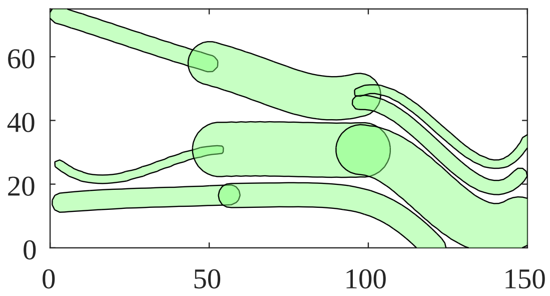

Figure 7.17. Component plot.

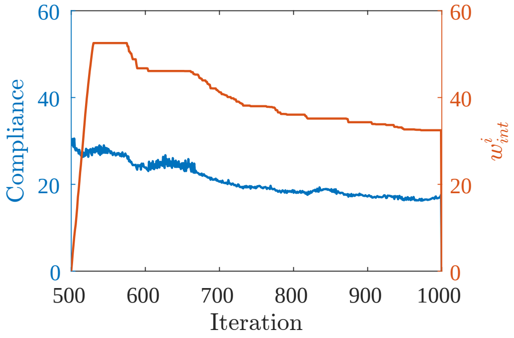

Figure 7.18. Convergence of adaptive weight.

Concluding from the described remarks, all formulations presented in this chapter are validated. However, the physical aspect of compliance minimization does not seem fully optimized from the structure in Fig. 7.14. By comparison to the unconstrained structure in Fig. 6.21, the constraints seem to cause geometric locking of the structure causing convergence to undesired local minima. The cause of this geometric locking is thought to be a combination of the following.

- Domain size.
- Number of predefined components.
- Overlap constraints.
- Minimum length constraints.

The effects of these are further investigated.

7.5.3 Investigation of Locking Problem

To investigate geometric locking and possible alleviation of locking to local minima, a comparison of test cases is performed. The unconstrained optimized result in Sec. 6.5.2 and the fully constrained result in Sec. 7.5.2 are included in the test cases, listed in Tab. 7.1, and used as references. For comparability all test are run for 1000 iterations.

Test	**Description**	**Structure**	C	**Result**
1	Unconstrained optimized structure	Fig. 6.21	3.65	Infeasible
2	Fully constrained structure	Fig. 7.14	17.6	Feasible
3	Constraints activated on unconstrained optimized structure	Fig. 7.19	89.1	Infeasible
4	Minimum length constraints removed	Fig. 7.20	13.0	Infeasible
5	Fully constrained without f_{int} contribution	Fig. 7.21	17.7	Infeasible
6	Fully constrained with double domain lengths	Fig. 7.22	-	Feasible
7	Fully constrained with four components	Fig. 7.23	13.9	Feasible
8	Fully constrained with five components	Fig. 7.24	21.5	Feasible

Table 7.1. Test cases and compliance comparison.

The resulting structure corresponding to each respective test is depicted in Fig. 7.19 through Fig. 7.21.

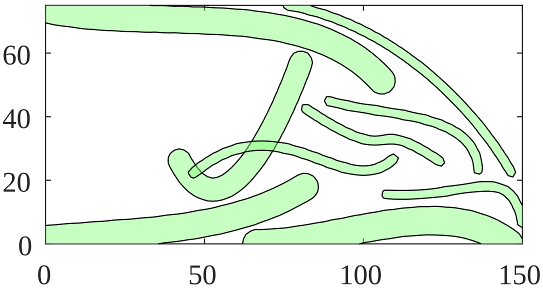

Figure 7.19. Test 3: Constraints activated on the optimized structure in Fig. 6.21.

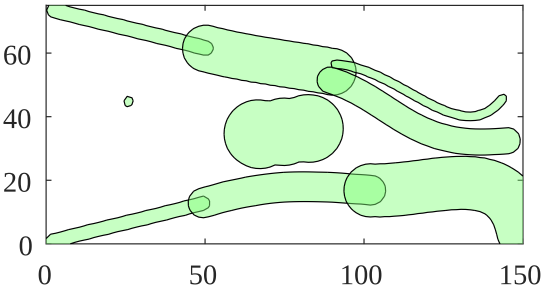

Figure 7.20. Test 4: Without length constraints.

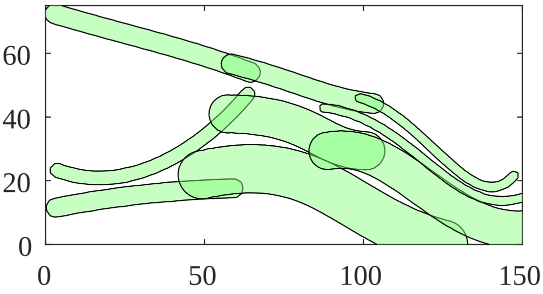

Figure 7.21. Test 5: Without f_{int} contribution.

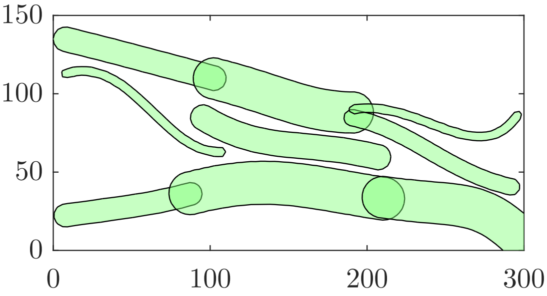

Figure 7.22. Test 6: Double domain lengths.

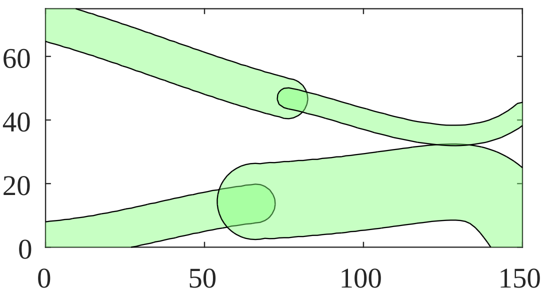

Figure 7.23. Test 7: Only four components.

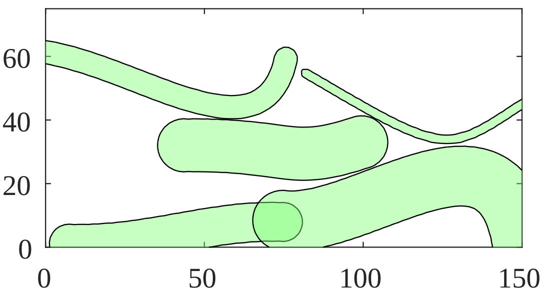

Figure 7.24. Test 8: Only five components.

From evaluation of the test cases the following remarks are noted.

- Overlap and curvature constraints has to be implemented initially to produce feasible designs (Comparison of test 2 and 3).
- The length constraints:
  - Cause geometric locking of the structure (Comparison of test 2 and 4).
  - Affects the structure formation since constraint fulfillment produce relatively long components and thereby enhance the initial condition dependency (Visual comparison of test 2, 4 and 6).
- The endpoint objective:
  - Might cause undesired geometric locking and needs further investigated (Comparison of test 2 and 5).
  - Is needed to produce feasible endpoint overlaps (seen from test 5)
- The predefined number of components:
  - Might alleviate geometric locking effects with fewer components and thereby produce equally or less compliant structures (evaluated from test 2 and 7)
  - Restricts the structure design freedom with fewer components and enhance the initial condition dependency (comparison of test 7 and 8)

From these remarks, a tuning of the presented optimization formulations is described and result presented in Sec. 7.5.5. The influence from the predefined number and placement of components on the resulting structure will not by further investigated, since the initial guess dependency is an inherent problem for the MMC framework.

By the remarks, the behavior of the multi-objective weighting needs to be further investigated.

7.5.4 Multi-objective Weighting - Effects of Adaptive Weight

Seen from Tab. 7.1, the fully constrained structure in test 2 has a compliance value approximately equal to the structure without the endpoint continuity objective in test 5. The compliance progression of these tests, after the weighting w_{int}^{i} is initialized, is seen in Fig. 7.25. In Fig. 7.26 the corresponding objective value contributions are depicted.

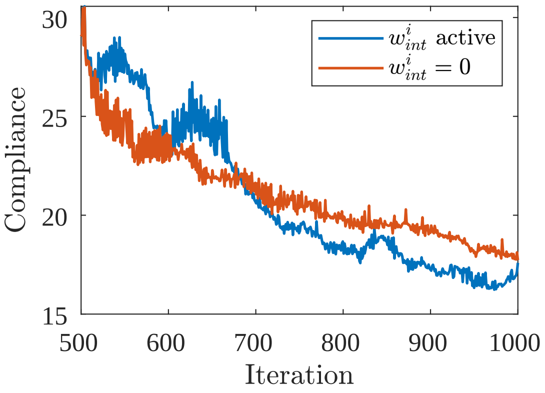

Figure 7.25. Compliance comparison of test 2 and 6.

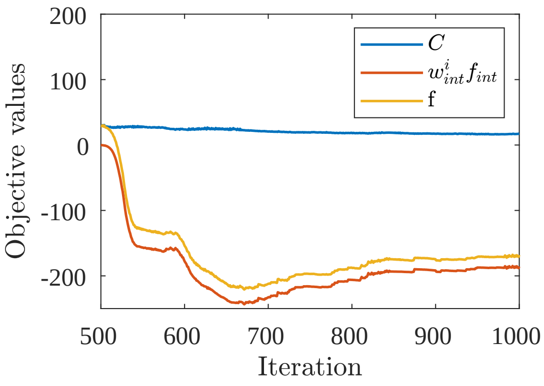

Figure 7.26. Objective value progressions of test 2.

From the comparison in Fig. 7.25, the implemented weighting affects the progression of compliance minimization. From visual comparison, the effect is destabilization of compliance convergence, but the results at the end are approximately identical. From Fig. 7.26, the weighting, combined with the negative values of f_{int}, is seen to rapidly decrease the multi-objective value f. After iteration 650, the combined objective is seen to increase and a concern of this effect is possible compliance minimization prohibition. However, this is not seen from the result of the test case. For argumentation the multi-objective formulation is repeated in Eq. (7.34).

$$f = C + w_{int}^{i} f_{int} \tag{7.34}$$

$$w_{int}^{i} = \alpha_{int}^{i} C_{min} \tag{7.35}$$

The reasoning of the concern for compliance minimization prohibition, is the scaling C_{min} in the adaptive weighting. Since f_{int} is negative and the adaptive relative weighting α_{int}^{i} converge to 2, the largest scaling factor C_{min} will produce the lowest overall objective f. Hence, the optimizer might account for this by not lowering C_{min} further. However, the endpoint continuity objective is necessary for feasible designs as shown in Fig. 7.21. From these arguments, the following remarks are noted.

- Implementation of the endpoint continuity objective is necessary for feasible endpoint overlap
- Implementation does not seem to increase the compliance value although this is still a concern.
- Implementation of the endpoint continuity objective does affect the progression of compliance minimization.

In conclusion, the endpoint continuity objective should only be implementation after compliance has converged, so C_{min} is the actual minimum. Results using the remarks listed are presented next.

7.5.5 Result by Formulation Tuning

From the fully constrained result in Sec. 7.5.2, all formulations were validated but locking to an undesired local minima seemed to occur, which is verified from the test case investigations. From the investigations, the parameters influencing the locking problem were remarked. For formulation tuning, these remarks are converted to guidelines for alleviating the locking effect. The guidelines are listed in the following.

- Compliance objective: Unaltered.
- Endpoint continuity objective: Initialize when compliance has converged (in these results at iteration 900).
- Volume, overlap, multioverlap and curvature constraints: Unaltered.
- Length constraints: Relax until a continuous structure is formed. In these results a continuously decreasing length relaxation, L^i_{relax}, is implemented as in Eq. (7.36). L^i_{relax} is set to 25 mm initially and decreased linearly to 0 mm between iteration 500 and 750.

$$\mathbf{g}^c_{length} = L_{min} - L^i_{relax} - \begin{Bmatrix} L^c_{edge+} \\ L^c_{edge-} \end{Bmatrix} \tag{7.36}$$

Using these guidelines, the resulting feasible structure is seen in Fig. 7.27. The result is shown at 1000 iterations and reaches a compliance value of 9.9, which is the lowest compared to all feasible tests and considerably lower than the fully constrained formulation. The progression of the structure is depicted in Appendix D.2.3 and the orientation and density fields used for computation are depicted in Appendix D.2.2.

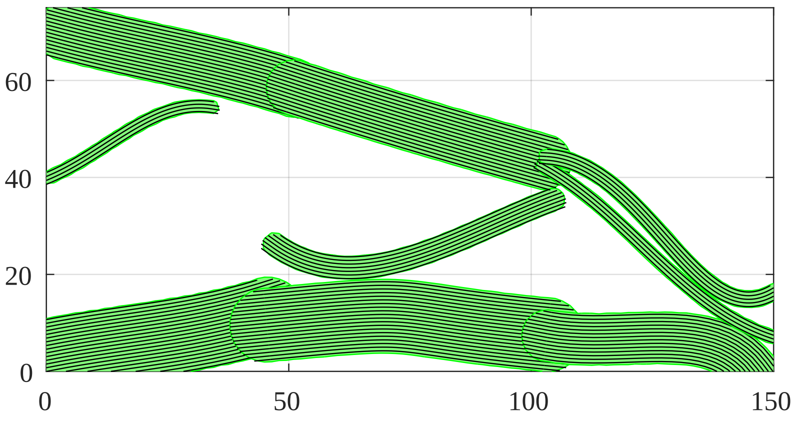

Figure 7.27. Manufacturable structure by formulation tuning.

To verify manufacturing feasibility, the component plot in Fig. 7.28 shows only allowable endpoint overlapping. The influence of the formulation tuning on compliance is seen in Fig. 7.29. As seen, the removal of the length constraint relaxation does not seem to influence compliance considerably. The introduction of the endpoint continuity objective does seem to increase compliance, however this increase is thought to be necessary to compute manufacturing feasible endpoint overlap.

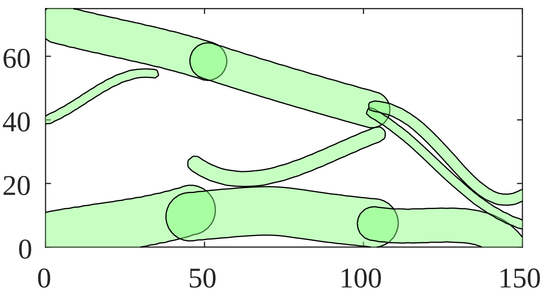

Figure 7.28. Component plot showing no infeasible overlap.

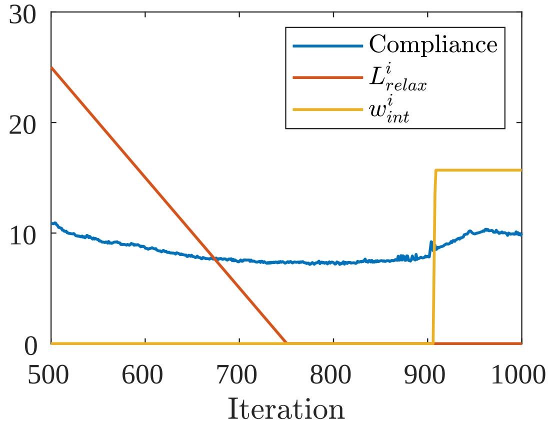

Figure 7.29. Compliance during formulation tuning.

With this result the manufacturing constraints are verified and concluded. Optimization formulation tuning for alleviation of geometric locking is presented but parameter tuning investigations will not be conducted.

With the implementation of manufacturing constraint in the optimization formulation, constrained compliance minimized structures are constructed. With this ensured, implementation of performance related criteria as failure is investigated.

8 | Strength Constraints

From obtaining geometrically feasible structures in the previous chapter, the next obvious step is to extend the scheme to obtain physically feasible structures, i.e. structures that do not fail. First, this chapter briefly reviews composite failure theories. A criterion is selected and implemented in the code. Next, challenges in strength-constrained optimization, and ways of overcoming them, are presented. Following this, a brief review on strength-based optimization with MMC is done. Strength constraints are implemented and results are obtained and discussed.

8.1 Composite Failure

Including failure aspects in the optimization formulation is motivated by avoiding part failure in the optimized part. In this work, failure is restricted to material failure modes.

8.1.1 Comparison and Selection of Failure Criteria

A multitude of composite failure criteria have been proposed, and not one is universally accepted. Naturally, the most important aspects of failure criteria are their ability to predict failure and their ease of use. Other than that, criteria can be compared in their ability to e.g. supply the mode of failure associated with the loading. Further, it may be advantageous that they use less, or more easily determined, strength parameters (Thomsen, 2010).

The following list is not an attempt on a complete overview of failure criteria. Instead, some criteria with unique advantages and disadvantages are listed, to illustrate the challenges involved in posing a failure criterion. The list is based on Thomsen (2010) and Jones (1999).

- 'Classic' criteria (Max. stress and max. strain)
    - ⊕ These criteria are popular and simple criteria and yield associated failure modes. They require only 5-6 material parameters, which can all be determined from uniaxial tests.
    - ⊖ Cusps make them non-differentiable in certain points, and there is limited- to no stress interaction (which, in some cases, is present).
- 'Physical' (e.g. Puck)

  - ⊕ Distinguishes between fiber- and matrix failure and is 'physically' based (i.e. provides insight to the failure).
  - ⊖ Is computationally expensive and may require tuning/determination of inclination parameters.

- 'Interactive' or 'polynomial' criteria (e.g. Tsai-Hill and Tsai-Wu)
  - ⊕ Easy to apply, and based on one equation. Takes interaction into account.
  - ⊖ Tsai-Hill assumes equal properties in tension and compression. For Tsai-Wu, one parameter has to be determined from an expensive biaxial test, alternatively it may be approximated from uniaxial data.

Thus, it is a difficult task to fulfill all requirements for failure criteria simultaneously. In this work, it may be less important *how* the material fails than *if* the material fails, as the criteria are incorporated as constraints. Thus, the convenient Tsai-Wu failure criterion is implemented.

8.1.2 Implementation of the Tsai-Wu Failure Criterion

The Tsai-Wu failure criterion represents the strengths in tensor form, Eq. (8.1a). For lamina in plane stress, the criterion reduces to Eq. (8.1b) (Jones, 1999).

$$F_i\bar{\sigma}_i + F_{ij}\bar{\sigma}_i\bar{\sigma}_j = 1 \tag{8.1a}$$

$$F_1\bar{\sigma}_1 + F_2\bar{\sigma}_2 + F_6\bar{\sigma}_6 + F_{11}\bar{\sigma}_1{}^2 + F_{22}\bar{\sigma}_2{}^2 + F_{66}\bar{\sigma}_6{}^2 + 2F_{12}\bar{\sigma}_1\bar{\sigma}_2 = 1 \tag{8.1b}$$

When the right-hand side is one, the criterion predicts failure. Thus the overbars on the stresses indicate the stress state that leads to failure.

The components of the strength tensors, with the plane stress assumption, can be related to the measured material strengths as given in Eq. (8.2) (Jones, 1999). The strength parameters used are given in Tab. 5.1.

$$F_1 = \frac{1}{X_t} + \frac{1}{X_c} \quad F_{11} = -\frac{1}{X_t X_c} \tag{8.2a}$$

$$F_2 = \frac{1}{Y_t} + \frac{1}{Y_c} \quad F_{22} = -\frac{1}{Y_t Y_c} \tag{8.2b}$$

$$F_6 = 0 \quad F_{66} = \frac{1}{S^2} \tag{8.2c}$$

$$F_{12} \approx -0.5\sqrt{F_{11}F_{22}} \tag{8.2d}$$

Eq. (8.2c) is from the sign-independence of shear stress and Eq. (8.2d) is an approximation to the interaction parameter that has to be determined from bi-axial tensile testing (Groenwold and Haftka, 2006).

For the Tsai-Wu criterion, care has to be taken. Because of the addition of the linear terms in Eq. (8.3), the Tsai-Wu criterion does not scale linearly with stresses. Groenwold and Haftka (2006) therefore propose to use the safety factor, equal to a failure multiplier, λ, in Eq. (8.3).

$$\bar{\sigma_i} = \lambda \sigma_i \tag{8.3a}$$

$$\lambda^2(F_{11}\sigma_1^2 + F_{22}\sigma_2^2 + F_{66}\sigma_6^2 + 2F_{12}\sigma_1\sigma_2) + \lambda(F_1\sigma_1 + F_2\sigma_2) - 1 = 0 \tag{8.3b}$$

Thus λ, which is equal to a Factor of Safety (FOS), may be found by solving the quadratic formula in Eq. (8.4a) for the smallest positive root.

$$a\lambda^2 + b\lambda + c = 0 \tag{8.4a}$$

$$\lambda = \frac{-b \pm \sqrt{b^2 - 4ac}}{2a} \tag{8.4b}$$

Instead of the FOS, the failure index, $\mathcal{F}$, given by Eq. (8.5), can be used.

$$\mathcal{F}_{TW} = \frac{1}{\lambda} \tag{8.5}$$

This definition of the Tsai-Wu failure criterion is implemented in the code. Thus, the stresses found in the Cartesian coordinate system by the finite element method are transformed using Eq. (5.8) into the material (1-2) coordinate system to evaluate the failure index, $\mathcal{F}_{TW}$, on an element basis.

8.2 Challenges in Strength-based TO

In the previous section, computation of the element-wise Tsai-Wu failure index, $\boldsymbol{\mathcal{F}_{TW}}^e$, was described. Thus, the present task is to limit the maximum value contained in this vector. In general, strength-constrained topology optimization has two difficulties; (1) strength is a local criterion, and (2) singular optima. Further, a jagged edge problem occurs. This section reviews these difficulties.

Interestingly, so far in this work, the decoupling of design model (the components) and analysis model (FE-grid of projected densities and angles) has been beneficial for implementation of geometric manufacturing constraints. Since stress is a local criterion, defined on element-basis, the parametrization of relatively few geometric parameters may lack local control, compared to e.g. SIMP.

8.2.1 Aggregation

Since the Tsai-Wu failure index is computed for every element, the number of constraints posed is infeasible to implement. Thus, similarly to the curvature constraint implemented previously, aggregation is used. The most common aggregation techniques are reviewed in Appendix C.2, based on this appendix the following selection is made.

Selection: For the strength constraint, the P-norm aggregation technique is adopted due to the failure index being strictly positive. Here, a global rather than regional aggregate is used. Thus the P-norm aggregated Tsai-Wu failure index is given by Eq. (8.6)

$$||\mathcal{F}_{TW}||_P = \left(\sum_{e=1}^{N_e} (\boldsymbol{\mathcal{F}_{TW}}^e)^P \right)^{\frac{1}{P}} \tag{8.6}$$

8.2.2 Singular Optima

Singular optima refer to optima which cannot be reached by gradient-based optimization due to the constraints present. In Sved and Ginos (1968), when optimizing a three-bar truss structure, the optimal solution was to remove one truss. However, the stress constraint prevented one bar from being removed. The same problem occurs in SIMP, due to the limit of the stress being nonzero for zero density (Verbart et al., 2015).

To avoid the problem of singular optima, the optimization problem is typically relaxed via ϵ-relaxation or qp-relaxation. In ϵ-relaxation, the constraint is perturbed by a small variable ϵ, which can be gradually changed in a continuation approach, to approach the original problem. In qp-relaxation, a parameter q is adopted in Eq. (8.7) (Bruggi, 2008) (Le et al., 2010).

$$\boldsymbol{\sigma}^e = (\boldsymbol{\rho}^e)^{p-q}\mathbf{C_0}\boldsymbol{\epsilon}^e \tag{8.7}$$

Here, $\mathbf{C_0}$ is for solid material. Thus for $q < p$, stresses are zero at zero density, solving the singularity problem. For SIMP, this method has the additional advantage of penalizing intermediate densities, driving the design toward discreteness.

Selection: With component projection in MMC, intermediate densities exist for the sole purpose of utilizing a fixed-grid mesh, and element-wise densities are not a design variable. Therefore it is argued that in this work, penalization of the intermediate densities through the stress state should not be done, as this would be the equivalent of penalizing the component perimeter length. On the other hand, as indicated by the results from Sec. 7.5.2, adjacent components appeared disconnected. Since intermediate densities are present on the edges, more connectivity may be achieved by penalizing intermediate densities. This aspect requires further study, but for simplicity the stress interpolation function for intermediate densities is chosen to be the same as for volume and compliance, consisting of multiplication by the density, Eq. (8.8)

$$\boldsymbol{\sigma}_{\mathbf{xy}}{}^e = \boldsymbol{\rho}^e\bar{\mathbf{Q}}^e\boldsymbol{\epsilon}^e \tag{8.8}$$

Here, $\bar{\mathbf{Q}}^e$ is the orthotropic stiffness matrix of solid material. Thus for $\boldsymbol{\rho}^e = 0$ the element stresses (and failure indices) are zero.

8.2.3 Jagged Edges

In general, intermediate density is a concept introduced to make the discrete topology optimization problem continuous. After optimization, a discrete design is sought. Thus, in SIMP, a threshold projection filter can be introduced to obtain discrete designs. However, when a fixed-grid model is used with a discrete design, artificial stress raisers can occur. This problem is generally referred to as the 'jagged edge' problem, and a schematic is shown on Fig. 8.1 (Hermansen and Olesen, 2020).

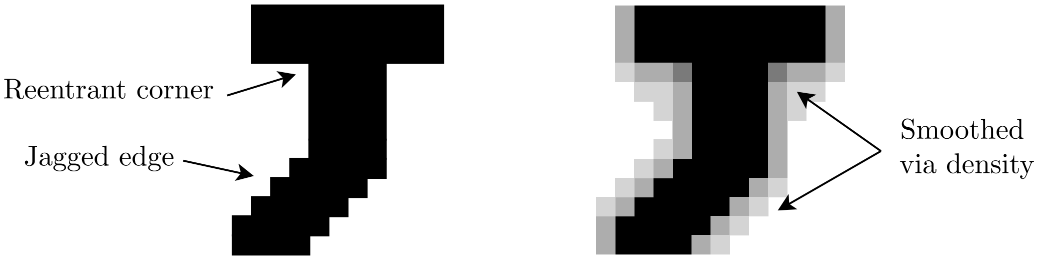

Figure 8.1. Jagged edge problem relieved by intermediate densities. Stress state lowered at reentrant corner.

One solution to this problem is to accept intermediate densities on the jagged edges (Hermansen and Olesen, 2020). da Silva et al. (2019) show that with the correct parameters for threshold projection and ϵ-relaxation, the intermediate boundary can reduce the error caused by jagged edges. Thus, improving the accuracy of the underlying structure via a layer of intermediate densities.

Selection: In this work, no attempt is made at resolving the jagged edge problem, since intermediate densities are present at all edges due to component projection. It is however emphasized that the parameters for Heaviside projection and stress interpolation in MMC can be tuned similarly to what is done in da Silva et al. (2019), such that an intermediate density layer on the edges can improve the accuracy of stress evaluation and mitigate the effects of jagged edges.

8.3 MMC with Strength Criteria

Only a few papers have included strength considerations in the problem formulation in the MMC framework. These are briefly reviewed.

Zhang et al. (2017a) are the first to do stress-based topology optimization using MMC. The component formulation consists of bars with constant width and semi-circular ends, where the length and angle of each component are design variables. Further, a component density is introduced to be able to remove components from the design domain. Different problem formulations are used, including a compliance minimization problem, a stress minimization problem and a volume minimization problem, the latter with a stress constraint.

A main result in Zhang et al. (2017a) is that with stress-based optimization in MMC, a connected initial guess is needed. Both the stress minimization problem and the stress constrained problem fail to converge when the components are initialized with interrupted load paths. When a connected initial structure is used, the solution converges, and with a smooth convergence for the stress constraint for the volume minimization problem.

In Rostami and Marzbanrad (2021) stress-constrained problems are solved using the MMC framework. The components used are varying-thickness components (similar to component 'b' in Fig. 6.1) and a curved skeleton component. In Rostami and Marzbanrad (2021), the initial guess has non-interrupted load paths and the results converge and satisfy the strength constraint.

In Zhang et al. (2017a), it is discussed that reentrant corners are present in the stress-optimized results, formed by component overlaps and that these are not accurately captured due to intermediate densities, as sketched previously in Fig. 8.1. However, since the component parametrization has no design freedom for generating smooth rounded corners, this can be expected. The component parametrization in terms of strength-based optimization will be further discussed in Chap. 11.

8.4 Implementation and Test

This section presents the optimization formulation with implemented strength constraints the results obtained from this formulation.

8.4.1 Pre-formulation Test

With the knowledge from Sec. 8.3, firstly the test results from Sec. 6.5 are revisited. The maximum failure index for every iteration is saved and plotted with compliance in Fig. 8.2. 12 elements near the load introduction are not considered when finding the maximum failure index, and the maximum failure index does not occur in the same elements in each iteration.

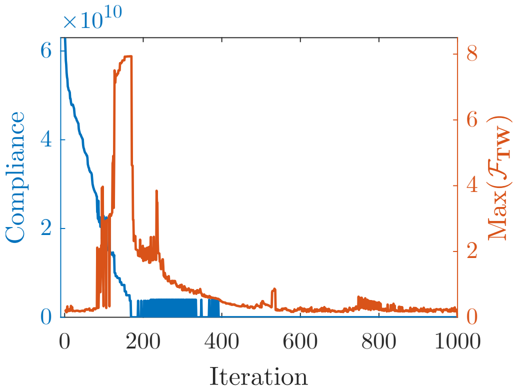

Figure 8.2. Same test as in Sec. 6.5, maximum failure index monitored.

As Fig. 8.2 shows, the maximum failure index is well above failure during iterations, especially where the components start to contact the fixed support or each other at approximately $75 - 200$ iterations, forming a load transfer path. These high failure indices are the likely cause of the need for a connected initial guess. Furthermore, initial tests conducted with the strength constraint, with an unconnected initial guess, agree with the other works presented in Sec. 8.3 in the sense that no solution was obtained.

To avoid the problem caused by disconnected initial guesses, the tuned constrained result from Sec. 7.5.5 is used as the initial guess for the failure index constrained formulation, presented in the next subsection.

8.4.2 Formulation and Parameters

The optimization problem is the same as in Eq. (7.33), except the failure index constraint, Eq. (8.9), is included.

$$g_{FI} = ||\mathcal{F}_{TW}||_P - 1 \leq 0 \tag{8.9}$$

A value of $P = 20$ is used for the P-norm. The benchmark example is the same as in the previous chapter, however, the load is increased from $F = 40\,\mathrm{N}$ to $F = 150\,\mathrm{N}$ as the initial guess using $F = 40\,\mathrm{N}$ already satisfies the failure index constraint. Two tests, with different discretizations, are run. One is 100×50 elements, consistent with the previous chapters. The other is with 200×100 elements. The move limits and gradient perturbations are the same as Tab. 6.2, except the endpoint coordinate perturbations are defined based on the discretization and are 1.5 mm and 0.75 mm for the coarse and fine discretization respectively. Furthermore, for the finely discretized model, α^i_{int} is fixed at a value of 2 due to the endpoint-continuity objective being deleted due to a drastic change in compliance in the first iterations, as shown in the next subsection.

8.4.3 Results

Fig. 8.3 and Fig. 8.4 shows the resulting structure after 1000 iterations, continued from the initial guess, with a coarse and fine discretization respectively.

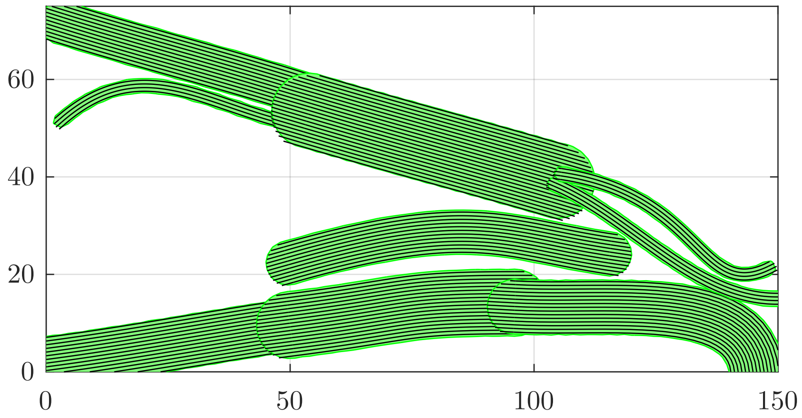

Figure 8.3. Structure plot with failure index constraint. 100 × 50 elements.

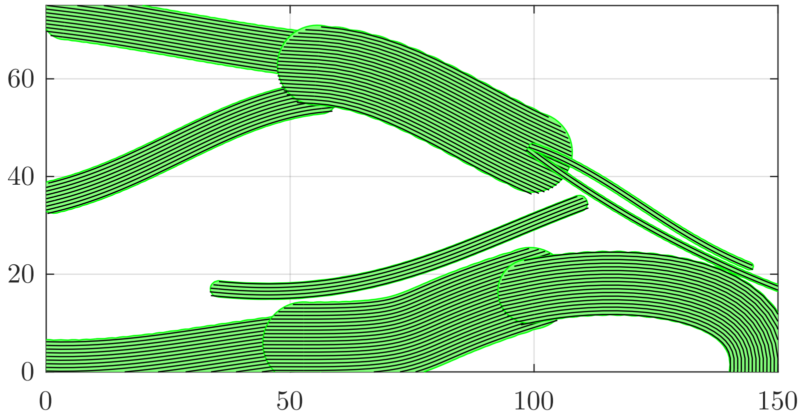

Figure 8.4. Structure plot with failure index constraint. 200 × 100 elements.

Fig. 8.5 and Fig. 8.6 show the element-wise failure index from the above two structures.

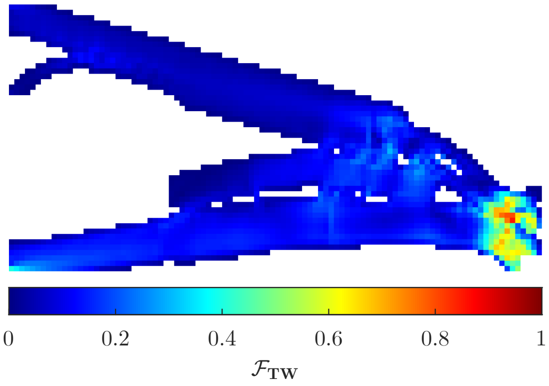

Figure 8.5. Element-wise Tsai-Wu failure index. 100 × 50 elements.

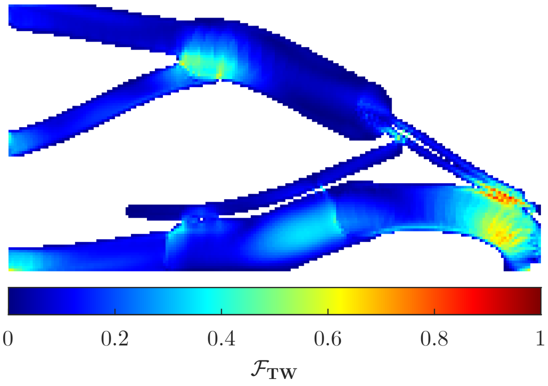

Figure 8.6. Element-wise Tsai-Wu failure index. 200 × 100 elements.

The resulting structures, using the different discretizations, are inherently different. The reason is likely the mesh refinement, since gradient perturbation sizes are different. In Tab. 8.1 the compliance and failure index of both the initial guess and result from optimization, using both discretizations, is given.

Objective and constraint	**Initial guess** 100 × 50	**Initial guess** 200 × 100	**Result** 100 × 50	**Result** 200 × 100
Compliance	140.65	159.64	116.38	164.14
$\|\|\mathcal{F}_{TW}\|\|_P$	1.10	1.84	0.88	0.92

Table 8.1. Objective and strength constraint at iteration 1 and iteration 1000.

As seen in the table, both structures satisfy the constraint, however, for the fine discretization it is expected that failure is being more accurately captured, leading to different structures. Furthermore, as expected, the objective is being compromised to satisfy the additional constraint.

In the results using the coarse mesh, one curvature constraint is violated by a value of 11×10^{-4}, however, the P-norm is overestimating this value. All other constraints, in both tests, are satisfied.

Fig. 8.7 and Fig. 8.8 show the iteration history of compliance and the P-norm aggregated Tsai-Wu failure index, for the coarse and refined mesh, respectively.

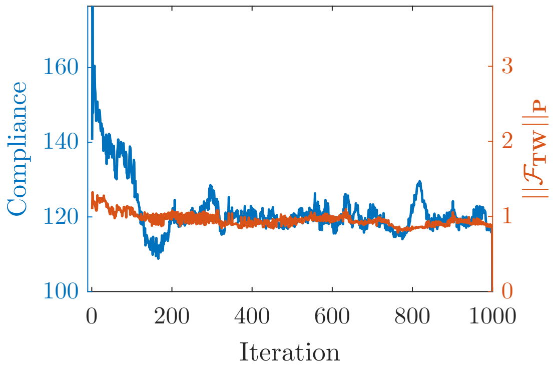

Figure 8.7. Convergence with failure index constraint using 100 × 50 elements.

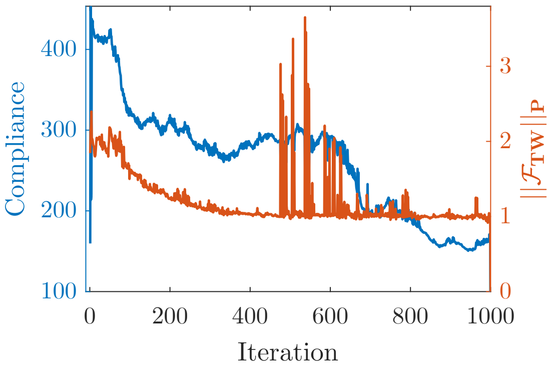

Figure 8.8. Convergence with failure index constraint using 200 × 100 elements.

In Fig. 8.8, the initially low compliance led to fixation of $\alpha^i_{int} = 2$ for all iterations. Interestingly, non-smooth convergence of the failure index constraint in the finely-discretized test is apparent, and the problem is still solved despite these peaks. It is expected that while high failure indices are present during optimization, they still provide meaningful directional information since the major part of the structure is already formed, in comparison to unconnected initial guesses.

With the results presented in this section, failure index constraints have successfully been implemented with active manufacturing constraints in this framework.

9 | Discussion

This chapter seeks to discuss the use and design-analysis-product relations of the developed scheme. Firstly, the use of the scheme is exemplified by other benchmark examples. Then, the inherent concern of restricting design freedom, by the use of the MMC framework, is discussed in relation to fiber placement. The analysis-product conformity is discussed and compared to other frameworks among missing considerations and method deficiencies.

9.1 Other Benchmark Examples

To investigate robustness of the presented scheme, two other benchmark examples are solved. These are the Messerschmitt-Bölkow-Blohm (MBB) beam and the L-bracket.

9.1.1 Example Setup

The boundary conditions for these examples are seen in Fig. D.20 and Fig. D.21. The optimization formulation used is the constrained in Eq. (7.33) with identical tuning to the result in Sec. 7.5.5. Meaning the length constraint relaxation is fully removed by iteration 750 and endpoint objective is activated at iteration 900. The dimensions, discretization and load used for computation are given in Tab. 9.1.

Parameter	**MBB**	**L-bracket**
Dimensions	150×50 mm	150×150 mm
Discretization	100×33 elements	100×100 elements
Load F	1 N	40 N

Table 9.1. Parameters used to generate results.

The initial conditions of the benchmark examples are depicted in Fig. 9.1 and Fig. 9.2.

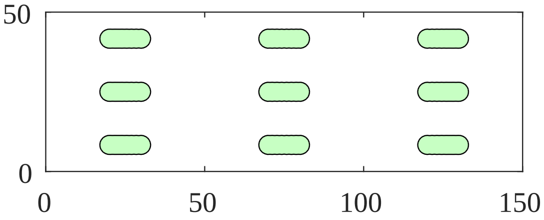

Figure 9.1. Initial conditions for the MBB beam.

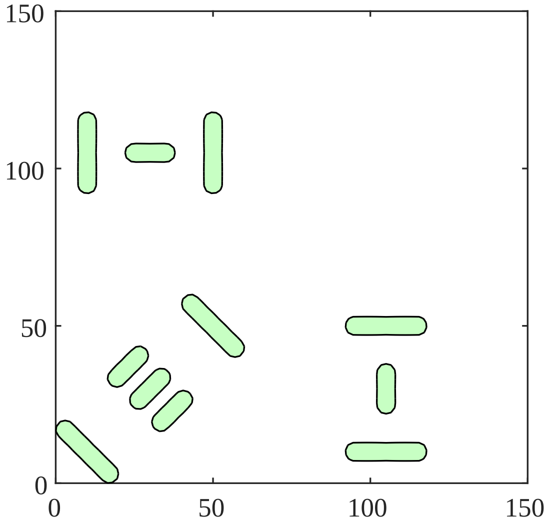

Figure 9.2. Initial conditions for the L-bracket.

With the described setup the benchmark examples are computed.

9.1.2 Results

The resulting structures are depicted for the MMB beam and L-bracket in Fig. 9.3 and Fig. 9.4 respectively. Again, the depicted discontinuity between adjacent components are only due to the geometric depiction and coarse mesh used, meaning these are connected in the analysis model as shown in Appendix D.3.1 and Appendix D.3.2.

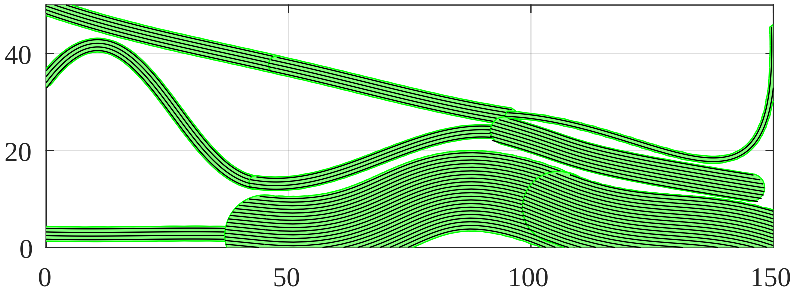

Figure 9.3. MBB beam at 2000 iterations.

From the MBB beam structure in Fig. 9.3, all manufacturing constraints are fulfilled. The compliance convergence is shown in Fig. D.22 and Fig. D.23 with a convergence similar to the presented of the cantilever. Hence, structure progression similar to previously described phases of component enlargement, nonlinear structure forming and considerable change after a continuous load path is constructed, occurs.

From the resulting L-bracket structure, the manufacturing constraint of overlap is not fulfilled due to an infeasible overlap of 0.2% of the volume, depicted approximately in the center of Fig. 9.4. Further, infeasible endpoint overlaps are seen in the top, left and center of the structure.

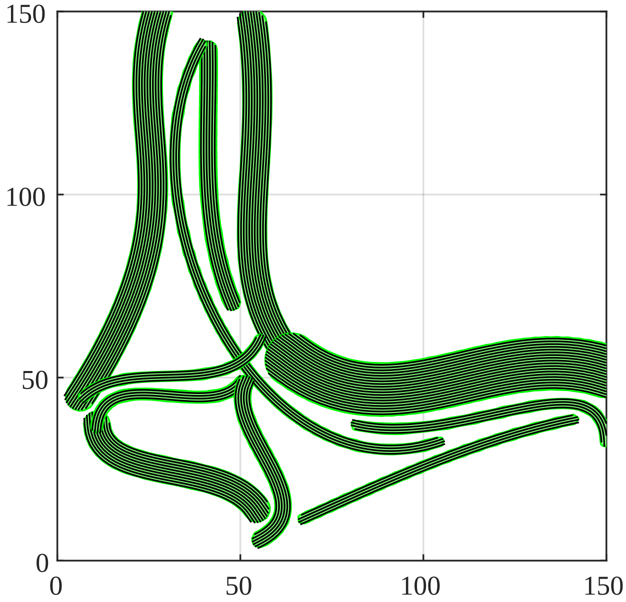

Figure 9.4. L-bracket at 1500 iterations.

All other constraints than the overlap constraint are fulfilled and the compliance convergence is given in Fig. D.24. From these results, notable remarks are given.

9.1.3 Remarks

Evaluating from the convergence and structure of the MBB beam in Fig. 9.3, the presented benchmark example has converged to a manufacturable compliance minimum. Evaluating from the upper right component in the structure, this minimum does seem to be local. Since convergence to local minima is an inherent problem for the framework, the result is evaluated as acceptable.

In the L-bracket, the reason for the infeasible endpoint overlaps, needs to be further investigated. The overlap constraint is implemented initially and endpoint continuity objective activated at iteration 900, as for the other computed structures. A possible reason is thought to be the perturbation sizes of the central difference approximations causing inaccurate sensitivities. This is described in Sec. 9.3.1.

Comparing the L-bracket to other works as Elmstrøm et al. (2023) and Papapetrou et al. (2020), the topology is significantly different. Again, the reason is thought to be locking to a local minimum. Alleviation strategies for the locking problem, is in this work limited to the tuned formulation presented in Sec. 7.5.5. Robustness of the tuning suggested has not been investigated for other examples and is left for further work.

9.2 Design Freedom

The main concern in Chap. 3 of utilizing the MMC framework, was the design restriction posed from the component parametrization and the number of components. Oppositely, as compared in Sec. 3.4, the main advantage of the MMC framework was alleviation of post-processing for manufacturing constraints due to this design restriction. Hence, the idea of matching the manufacturing constraints with the design restrictions through the parametrization occurred. Thereby, total design freedom within the manufacturing constraints would be inherently integrated in the method. This section seeks to discuss whether the parametrization utilizes the full design freedom within the manufacturing constraints.

Here, design freedom is evaluated by the individual component parametrization and component interactions since these form the structure. For evaluation, a reference needs to be established, which from the problem statement and the introduction, is stated as AM processes being capable of producing structures with "selectively deposited fibers". By selectively deposited fibers, a single continuous fiber being placed as an arbitrary curve fulfilling the manufacturing constraints, is meant. If this is allowed by the parametrization, the total design freedom is utilized.

To compare the component parametrization, a schematic of the fiber placement concept is depicted in Fig. 9.5. The curve depicted in 1) is the reference selectively deposited fiber. Sketched in 2) is the cubic component skeleton curve used in the component formulation. Depicted in 3) is the arbitrary reference curve constructed by multiple connected component skeletons. Seen from Fig. 9.5, the parametrization of a single component does cause design restrictions, but due to the formulated endpoint continuity, arbitrary curves are possible.

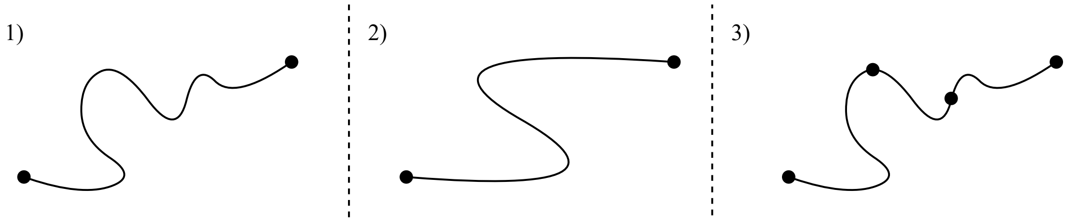

Figure 9.5. 1) Total fiber placement freedom: Arbitrary curve fulfilling length, curvature and overlap constraint. 2) Fiber placement by cubic component parametrization. 3) Fiber placement of arbitrary curve by multiple components with endpoint continuity.

A limiting factor is the length constraint on every component, causing the length of every segment of the curve in 3) to be at least L_{min}. Further, fibers are not placed individually due to the intra-component fiber placing accounting for multiple parallel fibers. However, components with constant thickness equal to one fiber could be implemented straightforwardly, allowing for individual fiber placement. This has not been investigated due to the scaling of domain size in the order of 100 mm and fiber thickness being 0.75 mm, causing a large amount of fibers, resulting in an infeasible number of design variables.

Thereby, the parametrization of the presented method causes the additional undesired design restrictions listed.

- Fiber placement by a cubic curve with minimum length L_{min} and not an arbitrary curve.
- Fibers placed parallel with equidistance within every component and not individually.

The first restriction could be alleviated by other spline component descriptions reviewed in Sec. 6.1 or increasing the polynomial degree. However design sensitivities and component stability becomes a concern. Another alleviation approach is length constraint relaxation when endpoint continuity is formed, but attempts were unsuccessful as described in Sec. 7.4.2.

The second restriction could be alleviated by initializing more components, but computational efficiency and memory is a practical restriction. Further, initializing more components contribute to geometric locking due to the minimum length and overlap constraints as stated in Sec. 7.5.3.

9.3 Analysis-Product Conformity

In Chap. 3, the relation between analysis and manufactured model through the design model was used for framework and method comparison. One of the main reasons for choosing the MMC framework was the close relation of the geometric design model and the manufactured product. A consequence of this relation is separation of the design and analysis model. This section seeks to discuss the discrepancies between the manufactured product and analysis model and thereby the inaccuracies of the analyzed product. Further, these are compared to other frameworks.

9.3.1 Correspondence of Product and Analysis Model

Here, multiple properties of the presented scheme is described and evaluated according to analysis-product conformity.

Intermediate Densities

An obvious discrepancy between the analysis and product is the nonphysical intermediate density elements on component boundaries. Using a fixed grid, intermediate density boundaries are inevitable, but the size of the boundary is controllable from the density Heaviside projection in Eq. (6.21). In all presented results, the Heaviside projection is tuned so only the density of the element on the boundary becomes intermediate. Hence, the effect of intermediate density boundaries are minimized. As seen in the results, elements of intermediate densities cause the analysis model to be connected while the design model is disconnected. This discrepancy should be resolved. Using a finer discretization, the effects are reduced, but not removed. The presented framework is a candidate method for explicitly-defined boundaries, and such extensions are suggested for further work.

Accuracy of Sensitivities from Central Differences Approximations

Another aspect in which the fixed grid affects the design, is in the gradient computation. This work uses semi-analytical gradients with central difference approximations. Since the physical properties as stiffness and volume are computed from projections to nodes, design variable perturbations are limited by the mesh size to compute a difference. Meaning the perturbations have to be large enough to change the density- and orientation fields to compute a gradient. Hence, the accuracy of the sensitivities are mesh size dependent.

Fiber Discontinuity Modeling

A typical error between the analysis and manufactured model is fiber discontinuity modeling. Stated throughout Chap. 3 none of the evaluated methods account for fiber discontinuities which specifically is a deficiency in the element-wise orientation parametrization methods. Fiber discontinuity modeling is not included in this work, however component-wise orientation alignment is given from the projection, instead of element-wise parametrization. Further, overlap connections are prohibited, and the combination of projection and prohibition, alleviates influence of the lacking modeling. To clarify, the possible component interactions are depicted in Fig. 9.6 where 2) and 3) in principle are the same interaction. Sketched in red are the projected element orientations. From the endpoint continuity in 1), the fiber orientations are aligned, hence no discontinuity modeling is needed.

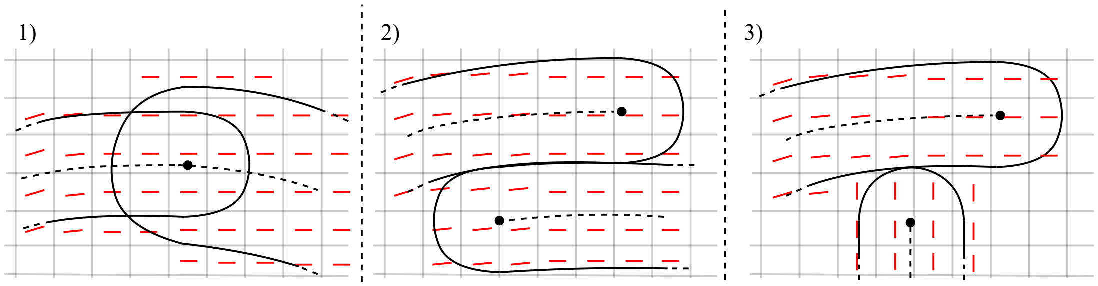

Figure 9.6. Sketched possible component connections and orientation fields.

In Fig. 9.6 2) the components align adjacent to each other and thereby the projected orientations are aligned. This interaction therefore corresponds to the transverse fiber properties which correspond to the geometry. Hence, fiber discontinuity modeling is not needed. With the same component boundary interaction, but unaligned components in 3), fiber discontinuity modeling is needed. Evaluating from the results presented throughout the report, the number of T-section interaction as in 3) is limited. Therefore, it is argued that the presented method alleviates the influence of lacking fiber discontinuity modeling.

Accuracy of Orientation Projection

In Sec. 6.3.3, two approaches for the construction of the orientation field were suggested. A continuous and differentiable averaging approach, and a recursive semi-circle approach, which was defined to yield correctly projected orientations. With the prospect of efficient computation, the averaging approach was chosen and implemented. As a result of this choice, the orientation fields are erroneous, but the deviations were evaluated as negligible. To argue the validity of this choice, the element-wise orientation difference between the used and the recursive semi-circle approach is shown in Fig. 9.7. The example used is the short cantilever beam from the tuned constrained formulation in Fig. 7.27.

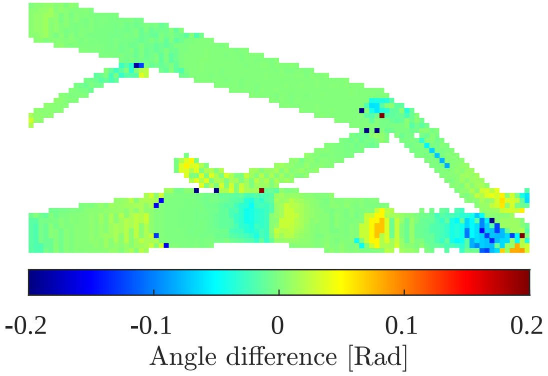

Figure 9.7. Orientation projection difference.

From Fig. 9.7, a maximum deviation of 0.2 Rad equal to 11° and an overall correspondence is seen. The validity of the projection thus depends on how sensitive the material properties are to this angular difference. If high fidelity is needed, the recursive semi-circle approach is suggested.

Missing Fiber Placement Modeling

In the presented method, the minimum fiber separation distance, D_{sep}, is accounted for, by placing fibers with equidistance of D_{sep} inside components. Thereby, the fiber volume fraction is kept constant and the defined material parameters are in accordance. But the component thickness t^c is parameterized as a continuous variable, and the material properties are used throughout the thickness. This means that, the analysis model does not account for the discrete number of fibers placed within a component. For clarification the problem is sketched in Fig. 9.8. Here, the actual fibers in the manufactured model are depicted red and the component edges black. As sketched, the distance from the edge to the first encountered fiber changes continuously and for conformity, the material properties in this region, should be altered accordingly. An alternative could be to evenly space the allowable discrete number of fibers and alter the fiber volume fraction accordingly. These details are not implemented.

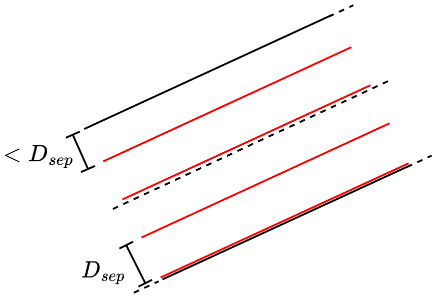

Figure 9.8. Discrepancy of component thickness and discrete number of fibers.

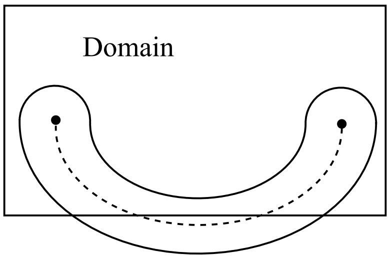

Figure 9.9. Geometric definitions unconstrained to the domain.

Another conformity issue caused by the separation of design and analysis model is that geometrically computed definitions are not constrained to the domain, as stated in Sec. 6.5.5. This, combined with the component parametrization, allows for the structure in the design model to be defined outside the domain, while the analysis model only accounts for projected nodal values inside the domain. A depiction is given in Fig. 9.9. This is specifically an issue, since the geometrically computed length and curvature constraints are computed outside the domain and are not cut as in the analysis model. Therefore a domain boundary definition should be defined.

9.3.2 Comparison to Other Frameworks

In comparison to other reviewed frameworks and methods in Chap. 3, the analysis, including element formulations, lacking fiber discontinuity modeling etc. is overall identical. An advantage for analysis-product conformity is the possible utilization of mesh techniques in the geometry based frameworks.

To compare the differences of analysis-product conformity between frameworks and methods, a broader perspective of the underlying limitations are needed. For clarification a comparison is constructed in Tab. 9.2. The comparison is constructed with basis in the reviews in Chap. 3 and only represents the methods conceptually.

Method	**Design parametrization**	**Fiber placement**	**Constrained via**	**Fiber continuity**
SOMP	Element density and orientation	Path planning	Post-processing and filtering	From path planning
DMO	Element material (orientation)	Path planning	Post-processing and filtering	From path planning
MTO-C	Element density and orientation layers	From membership filtering	Component filtering	Component-wise
Level-set	Higher order function	-Fast-marching -Path planning	Fast-marching	Edge dependent
MMC	Bar components and number	From design	In design	Component-wise
This work	ANCF components and number	From design	In design	Component-wise and endpoint continuity

Table 9.2. Method comparison.

The inherent differences of these methods have basis in the design parametrization, which the other listed properties are a direct cause of. In Sec. 3.4 it is argued that, post-processing alters the optimized design causing loss of analysis-product conformity. Evaluated from Tab. 9.2, the main cause for the need of post-processing in SOMP, DMO and MTO-C, is the lack of fiber placement consideration in the design. As a consequence, filtering techniques and path planning accounting for the manufacturing constraints are needed. Thereby, conformity is worsened and in worst case fibers are unmanufacturable leading to a different design. An example of unmanufacturable fibers is given in Fig. 9.10, where the SOMP method is utilized with orientation filtering and streamlining as path planning (Elmstrøm et al., 2023). The example is an L-bracket with the same manufacturing limitations and overall dimensions as the computed example in Fig. 9.4.

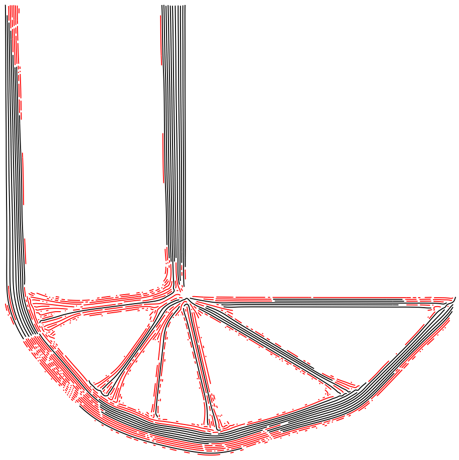

Figure 9.10. L-bracket from Elmstrøm et al. (2023) showing unmanufacturable fibers in red.

Marked in red are the fiber paths that do not satisfy the manufacturing limitations. Compared to the visualized fibers in Fig. 9.4, the amount of manufacturable volume is significantly larger for the presented approach compared to the SOMP example. Therefore, the approach of implementing constraints in the design has the intended effect of increasing analysis-product conformity compared to other methods.

9.4 Initial Guess Dependence

Gradient-based solvers find local minima to the optimization problem. With such solvers, the solution depends on the initial guess. Here, arguments are put, that initial guess dependency applies to a larger extent to the formulation proposed in this work, in comparison to other works.

Guo et al. (2016) use the MMC framework, with isotropic materials, without overlap constraints. Herein, different initial guesses are used. By visual inspection of the resulting component plots, it is seen that different component layouts lead to approximately the same structural topology. These result due to overlap. Since overlap is not allowed in the formulation proposed in this work, it is expected that, due to the lack of this mechanism, initial guess dependence will be more pronounced.

Initial guess dependency, has been viewed as an inherent problem in the MMC formulation, and studies of the problem have thus not been conducted. Thus, no advice can be given as to how an initial guess should be defined for the compliance minimization problem. For the strength-constrained problem it is suggested that the initial guess follows a compliance-minimization problem. Thereby, load paths are formed when the strength constraint is activated, in agreement with the works of Zhang et al. (2017a).

10 | Conclusion

The goal of this work was to develop a Moving Morphable Components-based scheme, for simultaneous topology and fiber layout optimization, in a way that ensures manufacturable parts and displays conformity between the analyzed and produced part.

The Absolute Nodal Coordinate Formulation was chosen to describe each component, allowing fibers to move, merge and curve throughout the design domain. Using the component skeleton to describe the fibers, an orientation field description was constructed to describe equally-spaced and intra-component continuous fibers. The lengths and curvatures were successfully described and constrained using P-norm aggregation for the point-wise curvatures. The fiber separation, length and curvature determine the manufacturing feasibility and quality of the produced part.

A formulation for inter-component fiber continuity without *a priori* knowledge of the component layout was formulated as a multi-objective problem. The formulation does not provide full fiber continuity in all cases, but lessens the amount of post-processing needed and the difference between analyzed and produced part. Furthermore, a component overlap constraint was formulated based on volume equality. Thereby, multiple fibers cannot be defined in the same place. Further, such constraint is necessary for the fiber length constraint to be defined, however, it is expected that this formulation makes the problem more initial guess dependent.

The element-wise Tsai-Wu failure index was successfully constrained below a value corresponding to failure on an optimized, manufacturable, part. However, in agreement with other studies, the initial guess for such formulation requires uninterrupted load paths.

The proposed developments can be used to ensure manufacturability, and conformity between analyzed and produced part, if the inter-component continuity function is successfully reduced to zero, and all constraints are fulfilled.

If conditions are satisfied, a topology and fiber layout with low compliance, reduced volume, that is not expected to fail and can be manufactured with limited post-processing, results from the scheme.

11 Suggestions for Further Developments

In this chapter, several suggestions are made for further developments of this work. The first section focuses on suggestions for the components and the problem formulation. The next section makes further suggestions to the numerical model.

11.1 Components and Formulation

The optimization formulation and component parametrization used in this thesis has been selected, based on the ability to model manufacturing limitations, such that they can be constrained. Here, several improvements are suggested.

Component Density

In Zhang et al. (2017a), a design variable $\alpha = [0, 1]$ for the component density is introduced. This design variable allows the optimizer to remove components from the design domain. In this work, the optimization is performed with a fixed number of components, which cannot be removed from the design. According to the results obtained in Chap. 7, the components tend to lock the design domain, because of the constraints. Therefore, the introduction of a design variable, capable of removing components, may improve the designs obtained, as well as reduce the initial guess dependency.

Multiple Materials

The use of multiple materials in the parametrization may be heavily motivated by e.g. cost considerations. For the MEX-based systems described in Chap. 2, multiple materials may be used in one part, with one or more nozzles used during the process. The cost differences between polymer and continuous fiber is given in Tab. 11.1.

Cost	**Polymer/short FR**	**Continuous FR**	**Unit**
Material cost	$\approx$ 0.20-0.22	$\approx$ 2.78	EUR/cm^3
Print speed	$\leq$ 80	$\leq$ 10	mm/s

Table 11.1. Material- and process related costs. Materials cost based on Markforged (n.d.), print speeds on Anisoprint (n.d.).

Based on Tab. 11.1, the continuous fiber material is significantly more expensive in terms of both materials cost and process time. Furthermore, in certain regions of the part it may be more efficient to have an isotropic material, for example in regions of biaxial stress. With the MMC formulation, it is possible to use multiple density fields to allow the use of multiple materials, as conceptually sketched in Fig. 11.1.

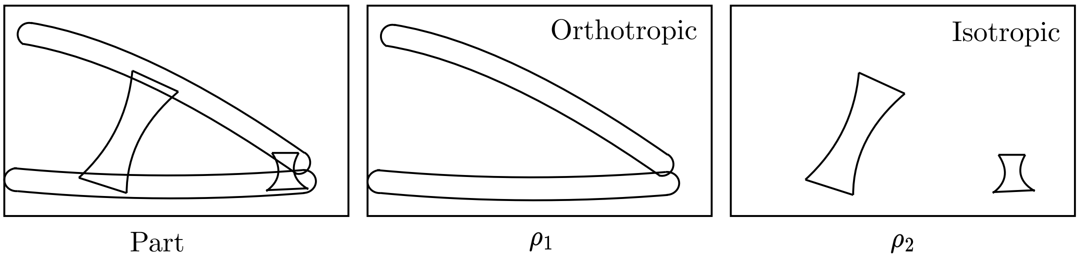

Figure 11.1. Multiple Materials in MMC.

Which should be used in junction with the constitutive matrix as defined in Eq. (11.1)

$$\mathbf{C}^e = \mathbf{C_0} + \boldsymbol{\rho_1}^e(\bar{\mathbf{Q}}^e - \mathbf{C_0}) + \boldsymbol{\rho_2}^e(\mathbf{C_{iso}} - \mathbf{C_0}) \tag{11.1}$$

Here, $\mathbf{C_0}$ is an isotropic material with $E = 1 \times 10^{-6}\,\text{MPa}$. Since the orthotropic and isotropic properties, $\bar{\mathbf{Q}}$ and $\mathbf{C_{iso}}$ respectively, cannot exist in the same element, a dominant density field description of $\boldsymbol{\rho_1}$ is needed.

Going 2.5D and 3D

This work focused on optimization in two dimensions. This is justified, since additive manufacturing is typically done in 2.5D, where 2D layers are stacked to form a 3D part. 2.5D computation is thought to be possible by constructing multiple layers of the presented method and combining these with laminate theory. However, if 2.5D aspects are to be implemented it is evident from Tab. 2.2 that more formulations are necessary, as listed below.

- A maximum overhang angle between layers should be taken into account.
- Voids in the part should be eliminated depending on the AM process in question (Does not apply to MEX, unless there are large overhangs in voids. Does apply to VPP and PBF, due to powder or polymer infiltrating the void).

An extension of the presented method to a full spatial description could be implemented by the following steps.

1. Alter domain and element formulations.
2. Expanding the component design variables in Eq. (6.13a) by endpoint z-coordinates and spatial orientations.
3. Replacing the shape function in Eq. (6.17) with the spatial ANCF shape function.
4. Adding z-direction thickness to the segment-wise TDF in Eq. (6.19a) and Eq. (6.22).

5. Computing spatial lengths, orientation etc. throughout Chap. 6 and Chap. 7.

A spatial description has not been pursued since AM processes are still limited in terms of their capability to manufacture parts with spatially varying fibers in 3D (Schmidt et al., 2020). However, if that is the goal, it is expected that the main difficulty involved is to include the path-planning in the optimization. Similar to in 2D, where fibers cannot overlap, the location of the printhead should be taken into account in 3D. This is thus a problem of structural layout and fabrication sequence, simultaneously. Some refer to this as "Space-time topology optimization" see e.g. Wang et al. (2020).

Components with Stress Relief Mechanisms

Zhang et al. (2018) used the Moving Morphable Void (MMV) approach, in which the area occupied by the "components" is treated as voids instead. The parametrization used for the voids is B-splines. Fig. 11.2 shows how overlap between the splines form sharp corners. These are treated by forming a boundary spline curve, effectively merging voids to a smooth structural boundary, depicted on Fig. 11.3.

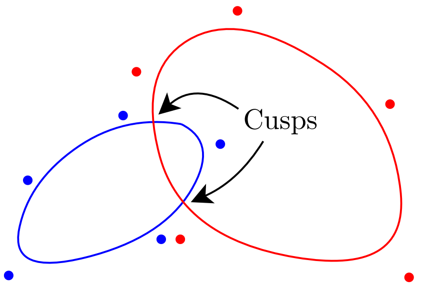

Figure 11.2. Two B-splines before merging, control points indicated. Process described by Zhang et al. (2018).

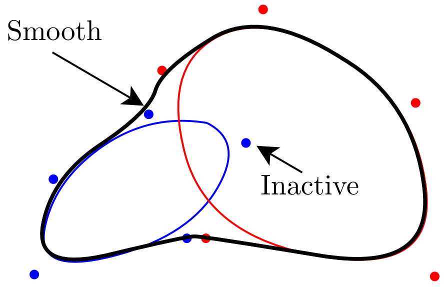

Figure 11.3. Merged B-spline, cusps are alleviated. This process is used in Zhang et al. (2018).

Thus, smooth corners in the resulting topology is in a sense built into this parametrization. Similar features may be built into the MMC framework, as it is expected to be difficult to reduce stresses, if design freedom does not exist. In the results of Zhang et al. (2017a), reentrant corners are formed from the components overlapping each other. The components in their work consists of bars of constant width with semi-circular ends. Thus, there is no design freedom for generating smooth rounded corners.

Suggestions for stress relief mechanisms are as follows:

- Use components where the skeleton can curve, as in the present work.
- Use components where the thickness can be varied through the length (similar to component b) in Fig. 6.1). This is also used in in Rostami and Marzbanrad (2021).
- Zhang et al. (2018) proposes that fillets are introduced at intersections between different components in the MMC framework.

11.2 Mathematical Model

It is by successive evaluation of the mathematical finite element model that the optimization results are generated. Further, it is the mathematical model that evaluates whether the constraints are fulfilled. Therefore, the model has to be of high enough fidelity, such that this process can be trusted. Alternatively, post-processing or re-evaluation in an improved model has to be done.

Component Boundary

In relation to the component boundary, multiple methods have been proposed to remove the intermediate densities for a crisp boundary definition, which some problems may require. These are e.g. remeshing via XFEM, as was done in the original MMC article in Guo et al. (2014). Such an approach can however cause severe element distortion. Alternatively CutFEM procedures have been proposed as outlined in Hermansen and Olesen (2020) and Andreasen et al. (2020). With such methods, intermediate densities, and the challenges they cause, can potentially be resolved.

Efficiency - Analytical Sensitivities

The sensitivities are throughout this report computed by central differences since the purpose of the presented method is a proof of concept, rather than efficient computation. However, most formulations are continuous and differentiable allowing for analytical sensitivities. Therefore, the focus of further work should be on reformulating the listed discontinuous formulations to allow for analytical sensitivities.

- Structure orientation field in Eq. (6.32).
- Adaptive weight, w_{int}^{i}, in multi-objective Eq. (7.12). However, convergence is ensured, hence analytical sensitivities could be argued negligible.
- Overlap constraint: Allowable endpoint overlap in Eq. (7.21). A suggestion for a differentiable formulation is given in Appendix E if discrepancies of geometrically and discrete element based volume computations are alleviated by e.g. XFEM, CutFEM or remeshing.
- Multi-overlap constraint in Eq. (7.23).

All other formulations presented throughout this report should be continuous and differentiable, allowing for analytical sensitivities.

Element Choice

The finite elements used in this work are isoparametric Q4 elements. Such elements were implemented, due to the possibility of having non-axis parallel element edges. However, the elements are still sensitive to distortion, and display parasitic shear, especially in bending (Cook et al., 2002). In the code, the element aspect ratio has been controlled, however, for general use, improved formulations may be necessary. Improved formulations to avoid parasitic shear strains are outlined in e.g. Cook et al. (2002).

Bibliography

Andreasen et al., 2020. Casper Schousboe Andreasen, Martin Ohrt Elingaard and Niels Aage. *Level set topology and shape optimization by density methods using cut elements with length scale control.* Struct Multidisc Optim, 62, pp. 685–707, 2020.

Anisoprint, 2022. Anisoprint. *Material datasheet, CFC PETG Ver. 2.1*, Anisoprint, 2022.

Anisoprint, n.d. Anisoprint. *Basic Specifications.* `https://anisoprint.com/solutions/desktop/`, n.d. Last used: 21-02-2024.

ANSYS, Inc., 2023. ANSYS, Inc. *Mechanical User's Guide*, 2023.

Baranowski et al., 2023. Michael Baranowski, Felix Basalla, Florian Kößler and Jürgen Fleischer. *Investigation of the Thermal Characteristics of a Novel Laser Sintering Machine for Additive Manufacturing of Continuous Carbon Fibre-Reinforced Polymer Parts.* Polymers, Journal 15, 3406, 2023.

Barbero, 2011. Ever J. Barbero. *Introduction to Composite Materials Design, 2nd ed.* ISBN: 978-1-4398-9413-2, eBook. CRC Press, 2011.

Bendsøe and Kikuchi, 1988. Martin Philip Bendsøe and Noboru Kikuchi. *Generating optimal topologies in structural design using a homogenization method.* Comput Methods Appl Mech Eng, 71, pp. 197–224, 1988.

Bendsøe and Sigmund, 2004. M.P. Bendsøe and O. Sigmund. *Topology optimization : theory, methods and applications.* ISBN: 3540429921, Engineering online library. Springer, 2004.

Boissonneault, 2022. Tess Boissonneault. *A new paradigm for composite additive manufacturing.* `https://www.voxelmatters.com/a-new-paradigm-for-composite-additive-manufacturing/`, 2022. Last used: 04-04-2024.

Bruggi, 2008. Matteo Bruggi. *On an alternative approach to stress constraints relaxation in topology optimization.* Struct Multidisc Optim, 36, pp. 125–141, 2008.

Cook et al., 2002. Robert D. Cook, David S. Malkus, Michael E. Plesha and Robert J. Witt. *Concepts and Application of Finite Element Analysis, Fourth Edition.* ISBN: 978-0-471-35605-9, Paperback. Wiley, 2002.

da Silva et al., **2019**. Gustavo Assis da Silva, André Teófilo Becka and Ole Sigmund. *Stress-constrained topology optimization considering uniform manufacturing uncertainties.* Comput Methods Appl Mech Eng, 344, pp. 512–537, 2019.

Dambrine and Kateb, **2010**. Marc Dambrine and Djalil Kateb. *On the ersatz material approximation in level-set methods.* ESAIM. Control, optimisation and calculus of variations, 16, pp. 618–634, 2010.

Deng and Chen, **2016**. JiaDong Deng and Wei Chen. *Design for structural flexibility using connected morphable components based topology optimization.* Sci. China Technol. Sci., 59, pp. 839–851, 2016.

DS/EN ISO/ASTM, **2022**. DS/EN ISO/ASTM. *Additive manufacturing - General principles - fundamentals and vocabulary.* 52900:2021, DS/EN ISO/ASTM. Danish Standard, 2022.

Elmstrøm et al., **2023**. Frederik Tobias Elmstrøm, Jacob Lykkegård Hansen, Rasmus Kaalund Schøn, Christian Troelsgaard and Frederik Brun Hoff Østergaard. *The Science of Compliance: Continuous Fiber Angle Topology Optimization with Stress Constraints and Path Planning*, Aalborg University, 2023.

ExOne, **2018**. ExOne. *What is Binder Jetting?* `https://www.exone.com/en-US/Resources/case-studies/what-is-binder-jetting`, 2018. Last used: 07-02-2024.

Gadegaard and Thuesen, **2022**. Frederik Juel Gadegaard and Jan Thuesen. *Strength based optimization and test of fiber reinforced additively manufactured structures considering topology and fiber orientation*, Aalborg University, 2022.

Gibson et al., **2021**. Ian Gibson, David Rosen, Brent Stucker and Mahyar Khorasani. *Additive Manufacturing Technologies, Third Ed.* ISBN: 978-3-030-56127-7, eBook. Springer, 2021.

Groenwold and Haftka, **2006**. Albert A. Groenwold and Raphael T. Haftka. *Optimization with non-homogeneous failure criteria like Tsai–Wu for composite laminates.* Struct Multidisc Optim, 32, pp. 183–190, 2006.

Guo et al., **2014**. Xu Guo, Weisheng Zhang and Wenliang Zhong. *Doing Topology Optimization Explicitly and Geometrically—A New Moving Morphable Components Based Framework.* J. Appl. Mech., Vol. 81/081009, 2014.

Guo et al., **2016**. Xu Guo, Weisheng Zhang, Jian Zhang and Jie Yuan. *Explicit structural topology optimization based on moving morphable components (MMC) with curved skeletons.* Comput Methods Appl Mech Eng, 310, pp. 711–748, 2016.

Hermansen and Olesen, **2020**. Sebastian Hermansen and Asbjørn Malte Olesen. *Topology Optimization of General Structures with Anisotropic Fatigue Constraints*, Aalborg University, 2020.

Jones, **1999**. Robert M. Jones. *Mechanics of Composite Materials, Second Edn.* ISBN: 978-1-56032-712-7, Hardcover. Taylor & Francis Group, 1999.

Khadiri et al., **2023**. Issam El Khadiri, Maria Zemzami, Nhan-Quy Nguyen, Mohamed Abouelmajd, Nabil Hmina and Soufiane Belhouideg. *Topology optimization methods for additive manufacturing: a review.* Int. J. Simul. Multidisci. Des. Optim., Journal 14, 12, 2023.

Khatua et al., **2023**. Vivek Khatua, B. Gurumoorthy and G. K. Ananthasuresh. *Selectively embedding multiple spatially steered fibers in polymer composite parts made using vat photopolymerization.* Indian Institute of Science, page 10, 2023.

Langnau, **n.d.** Leslie Langnau. *What is polymer directed energy deposition (DED) for 3D printing and how can it benefit you?* `https://www.designworldonline.com/what-is-polymer-directed-energy-deposition-ded-for-3d-printing-and-how-can-it-benefit-you/`, n.d. Last used: 22-02-2024.

Le et al., **2010**. Chau Le, Julian Norato, Tyler Bruns, Christopher Ha and Daniel Tortorelli. *Stress-based topology optimization for continua.* Struct Multidisc Optim, 41, pp. 605–620, 2010.

Leger, **1999**. J. C. Leger. *Menger Curvature and Rectifiability.* Annals of mathematics, 149, pp. 831–869, 1999.

Li et al., **2023**. Zonghao Li, Xueyan Hu and Weiqiu Chen. *Moving morphable curved components framework of topology optimization based on the concept of time series.* Struct Multidiscip Optim, 66, 19, 2023.

Liu and Du, **2021**. Dong Liu and Jiangfeng Du. *Shape and topology optimization in electrical impedance tomography via moving morphable components method.* Struct Multidiscip Optim, 64, pp. 585–598, 2021.

Loughborough University, **N.d.** Loughborough University. *The 7 Categories of Additive Manufacturing.* `https://www.lboro.ac.uk/research/amrg/about/the7categoriesofadditivemanufacturing/`, N.d. Last used: 07-02-2024.

Lu et al., **2022**. Yue Lu, Xiaoxiao Han, Andrew Gleadall, Feng Chen, Wei Zhu and Liguo Zhao. *Continuous fibre reinforced Vat photopolymerisation (CONFIB-VAT).* Additive Manufacturing, 60, 103233, 2022.

Lund, **2023**. Erik Lund. *Lecture in Engineering Optimisation – Concepts, Methods and Applications.* Lecture 9, Structural Optimization, 2023.

Markforged, **n.d.** Markforged. *Materials.* `https://shop.markforged.com/shop/s/category/products-and-services/materials/0ZG5d000000800IHGA2?c__results_layout_state=%7B%7D`, n.d. Last used: 21-02-2024.

Markforged, **2022**. Markforged. *Design Guide for 3D Printing with Composites, Ver. 1.7.* `https://support.markforged.com/portal/s/article/Composites-Design-Guide-1`, 2022. Last used: 14-02-2024.

Marler and Arora, **2010**. R. Timothy Marler and Jasbir S. Arora. *The weighted sum method for multi-objective optimization: new insights.* Struct Multidisc Optim, 41, pp. 853–862, 2010.

Mason and Gardiner, **2022**. Hannah Mason and Ginger Gardiner. *3D printing with continuous fiber: A landscape.* `https://www.compositesworld.com/articles/3d-printing-with-continuous-fiber-a-landscape`, 2022. Last used: 21-02-2024.

Matsuzaki et al., **2018**. Ryosuke Matsuzaki, Taishi Nakamura, Kentaro Sugiyama, Masahito Ueda, Akira Todoroki, Yoshiyasu Hirano and Yusuke Yamagata. *Effects of Set Curvature and Fiber Bundle Size on the Printed Radius of Curvature by a Continuous Carbon Fiber Composite 3D Printer.* Additive Manufacturing, Journal 24, pp. 93–102, 2018.

Mokhtarzadeh et al., **2024**. M Mokhtarzadeh, F Lopez Jimenez and K Maute. *Concurrent level set and fiber orientation optimization of composite structures.* arXiv preprint arXiv:2403.18971, 2024.

Norato et al., **2015**. J.A. Norato, B.K. Bell and D.A. Tortorelli. *A geometry projection method for continuum-based topology optimization with discrete elements.* Comput Methods Appl Mech Eng, 293, pp. 306–327, 2015.

Oest and Lund, **2017**. Jacob Oest and Erik Lund. *Topology optimization with finite-life fatigue constraints.* Struct Multidisc Optim, 56, pp. 1045–1059, 2017.

Otsuka et al., **2023**. Keisuke Otsuka, Shuonan Dong, Ryo Kuzuno, Hiroyuki Sugiyama and Kanjuro Makihara. *Moving Morphable Multi Components Introducing Intent of Designer in Topology Optimization.* AIAA Journal, 61, pp. 1720–1734, 2023.

Papapetrou et al., **2020**. Vasileios S. Papapetrou, Chitrang Patel and Ali Y. Tamijani. *Stiffness-based optimization framework for the topology and fiber paths of continuous fiber composites.* Composites. Part B, Engineering, 183, 107681–, 2020.

Pedersen, **1989**. P. Pedersen. *On optimal orientation of orthotropic materials.* Structural Optimization, 1, 101–106, 1989.

Pedersen, **2000**. P. Pedersen. *On optimal shapes in materials and structures.* Struct Multidisc Optim, 19, 169–182, 2000.

Rostami and Marzbanrad, **2021**. Pooya Rostami and Javad Marzbanrad. *Stress-limited topology optimization with local volume constraint using moving morphable components.* Arch. Appl. Mech., Journal 91, pp. 2345–2367, 2021.

Schmidt et al., 2020. Martin-Pierre Schmidt, Laura Couret, Christian Gout and Claus B.W. Pedersen. *Structural topology optimization with smoothly varying fiber orientations.* Struct Multidisc Optim, 62, 3105–3126, 2020.

Sethian and Wiegmann, 2000. J.A. Sethian and Andreas Wiegmann. *Structural Boundary Design via Level Set and Immersed Interface Methods.* J. Comput. Phys., 163, pp. 489–528, 2000.

Shabana, 2014. Ahmed A. Shabana. *Dynamics of multibody systems.* ISBN 978-1-107-04265-0, Hardback. Cambridge University Press, 2014.

Shannon et al., 2022. T. Shannon, T. T. Robinson, A. Murphy and C. G. Armstrong. *Generalized Bezier components and successive component refinement using moving morphable components.* Struct Multidiscip Optim, 65, 2022.

Sigmund, 2001. O. Sigmund. *A 99 line topology optimization code written in matlab.* Struct Multidiscip Optim, 21, pp. 120–127, 2001.

Sigmund, 2007. Ole Sigmund. *Morphology-based black and white filters for topology optimization.* Struct Multidisc Optim, 33, pp. 401–424, 2007.

Smith and Norato, 2021. Hollis Smith and Julián A. Norato. *Topology optimization with discrete geometric components made of composite materials.* Comput Methods Appl Mech Eng, 376, 113582–, 2021.

Smith and Norato, 2019. Hollis A Smith and Julián A Norato. *Geometric constraints for the topology optimization of structures made of primitives.* SAMPE 2019-Charlotte, NC, 2019.

Stegmann and Lund, 2005. J. Stegmann and E. Lund. *Discrete material optimization of general composite shell structures.* Int J Numer Methods Eng, 62, pp. 2009–2027, 2005.

Stolpe and Svanberg, 2001. M. Stolpe and K. Svanberg. *On the trajectories of penalization methods for topology optimization.* Struct Multidisc Optim, 21, pp. 128–139, 2001.

Sun et al., 2022. Zhi Sun, Ziwen Song, Junfu Song and Haiyan Li. *Structural Optimization of Fiber-Reinforced Material Based on Moving Morphable Components (MMCs).* Acta Mech. Solida Sin., 35, pp. 632–646, 2022.

Svanberg, 2007. Krister Svanberg. *Mma and gcmma.* Versions September, 2007.

Svanberg, 1987. Krister Svanberg. *The method of moving asymptotes-a new method for structural optimization.* Int. J. Num. Met. Eng., 24, pp. 359–373, 1987.

Sved and Ginos, 1968. G. Sved and Z. Ginos. *Structural optimization under multiple loading.* International Journal of Mechanical Sciences, 10, pp. 803–805, 1968.

Thomsen, 2010. Ole Thybo Thomsen. *Failure in Composite Materials.* Lecture notes for Ph.D. course on "Analysis and Design Optimisation of Laminated Composite Structures", 2010.

Top3DMedia, 2022. Top3DMedia. *Anisoprint Composer A4 3D Printer In-Depth Review.* `https://top3dshop.com/blog/anisoprint-composer-a4-3d-printer-review`, 2022. Last used: 14-02-2024.

Ukil et al., 2011. Abhisek Ukil, Vishal H Shah and Bernhard Deck. *Fast computation of arctangent functions for embedded applications: A comparative analysis.* 2011 IEEE International Symposium on Industrial Electronics, pages pp. 1206–1211, 2011.

Verbart et al., 2015. Alexander Verbart, Fred van Keulen and Matthijs Langelaar. *Topology Optimization With Stress Constraints.* ISBN: 978-94-6259-739-6, Publisher's PDF. TU Delft, 2015.

Wang et al., 2003. Michael Yu Wang, Xiaoming Wang and Dongming Guo. *A level set method for structural topology optimization.* Comput Methods Appl Mech Eng, 192, pp. 227–246, 2003.

Wang et al., 2020. Weiming Wang, Dirk Munro, Charlie C. L.Wang, Fred van Keulen and Jun Wu. *Space-time topology optimization for additive manufacturing.* Struct Multidisc Optim, 61, pp. 1–18, 2020.

Xu et al., 2022. Yanan Xu, Yunkai Gao, Chi Wu, Jianguang Fang, Guangyong Sun, Grant P. Steven and Qing Li. *Concurrent optimization of topological configuration and continuous fiber path for composite structures — A unified level set approach.* Comput Methods Appl Mech Eng, 399, 115350–, 2022.

Xu et al., 2024. Yanan Xu, Zhaoxuan Feng, Yunkai Gao, Chi Wu, Jianguang Fang, Guangyong Sun, Na Qiu, Grant P Steven and Qing Li. *Topology optimization for additive manufacturing of CFRP structures.* Int. j. Mech. Sci., 269, 108967–, 2024.

Zhang et al., 2024. Feng Zhang, Bowen Li, Wuzhan Wo, Xiaobin Hu, Min Chang and Peng Jin. *Topology Design of 3D Printing Continuous Fiber-Reinforced Structure Considering Strength and Non-Equidistant Fiber.* Advanced engineering materials, 26, 2301340, 2024.

Zhang et al., 2021. Haoqi Zhang, Jiayun Chen and Dongmin Yang. *Fibre misalignment and breakage in 3D printing of continuous carbon fibre reinforced thermoplastic composites.* Additive Manufacturing, Journal 38 (2021), 101775, 2021.

Zhang et al., 2017a. Shanglong Zhang, Arun L. Gain and Julián A. Norato. *Stress-based topology optimization with discrete geometric components.* Comput. Methods Appl. Mech. Engrg., Journal 325, pp. 1–21, 2017a.

Zhang et al., 2016. Weisheng Zhang, Jie Yuan, Jian Zhang and Xu Guo. *A new topology optimization approach based on Moving Morphable Components (MMC) and the ersatz material model.* Struct Multidiscip Optim, 53, pp. 1243–1260, 2016.

Zhang et al., 2017b. Weisheng Zhang, Wanying Yang, Jianhua Zhou, Dong Li and Xu Guo. *Structural Topology Optimization Through Explicit Boundary Evolution.* J. Appl. Mech., 84, 2017b.

Zhang et al., 2018. Weisheng Zhang, Dong Li, Jianhua Zhou, Zongliang Du, Baojun Li and Xu Guo. *A Moving Morphable Void (MMV)-based explicit approach for topology optimization considering stress constraints.* Comput. Methods Appl. Mech. Engrg., Journal 334, pp. 381–413, 2018.

Zheng and Kim, 2020. Rongzhen Zheng and Cheol Kim. *An Enhanced Topology Optimization Approach Based on the Combined MMC and NURBS-Curve Boundaries.* Int. J. Precis. Eng. Manuf., 21, pp. 1529–1538, 2020.

Zhou and Saitou, 2018. Yuqing Zhou and Kazuhiro Saitou. *Gradient-based multi-component topology optimization for stamped sheet metal assemblies (MTO-S).* Struct Multidiscip Optim, 58, pp. 83–94, 2018.

Zhou et al., 2018. Yuqing Zhou, Tsuyoshi Nomura and Kazuhiro Saitou. *Multi-component topology and material orientation design of composite structures (MTO-C).* Comput Methods Appl Mech Eng, 342, pp. 438–457, 2018.

Zhu et al., 2021. Benliang Zhu, Rixin Wang, Nianfeng Wang, Hao Li, Xianmin Zhang and Shinji Nishiwaki. *Explicit structural topology optimization using moving wide Bezier components with constrained ends.* Struct Multidiscip Optim, 64, pp. 53–70, 2021.

A | Background on AM Processes

This appendix provides background information on the seven AM-processes as defined by ISO 52900:2021 (DS/EN ISO/ASTM, 2022), in the form of their basic definition and supplementary conceptual sketches.

Binder Jetting (BJT) and Material Extrusion (MEX)

In BJT, a powder material is joined by application of a liquid bonding agent. The bonding agent may be deposited from a print head. Fig. A.1 shows a conceptual sketch of the process. In MEX, material is dispensed through a nozzle. To make a three-dimensional part, the nozzle- and/or part is moved and more material dispensed onto the part. The material is typically supplied from a spool with wire filament. The process is shown in Fig. A.2.

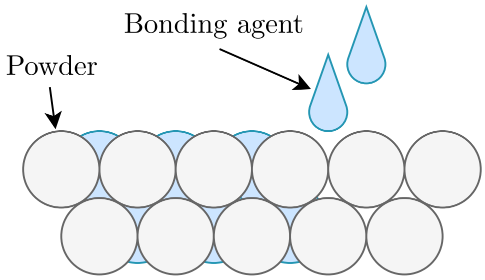

Figure A.1. Binder jetting. Inspired by ExOne (2018).

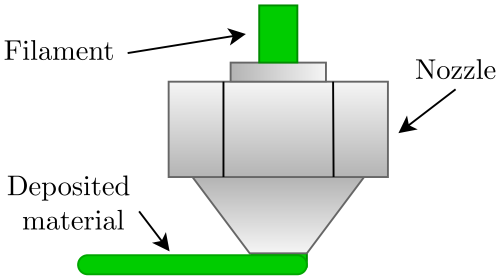

Figure A.2. Material Extrusion. Inspired by Loughborough University (N.d.).

Material Jetting (MJT) and Vat Photopolymerisation (VPP)

In MJT, droplets of material are sequentially deposited and solidified using UV light. The process is similar to ink jet printing. The process is seen in Fig. A.3. VPP uses a photopolymer resin, contained in a vat. The resin is selectively cured via light, shown in Fig. A.4.

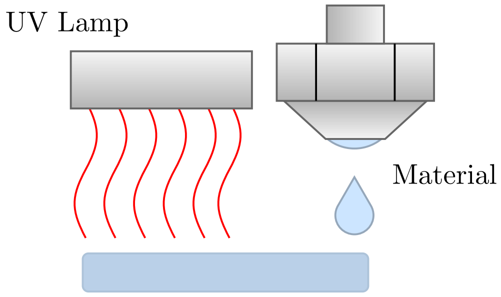

Figure A.3. Material jetting. Inspired by Loughborough University (N.d.).

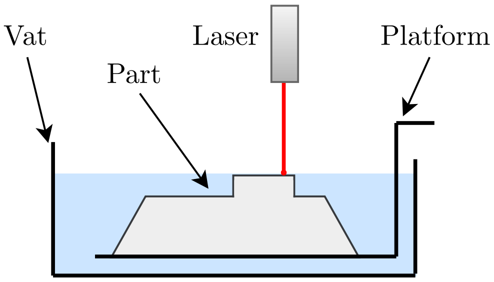

Figure A.4. Vat photopolymerisation. Inspired by Loughborough University (N.d.).

Powder Bed Fusion (PBF) and Directed Energy Deposition (DED)

In PBF, thermal energy is supplied to a powder bed (e.g. via laser), joining the base material in powder form into a part, seen in Fig. A.5. In DED, material is supplied (in powder or wire form) and fused via melting as they are being deposited. Energy is supplied by e.g. lasers, arcs or electron beams. This process is shown in Fig. A.6.

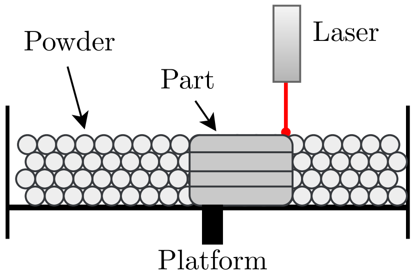

Figure A.5. Powder bed fusion. Inspired by Loughborough University (N.d.).

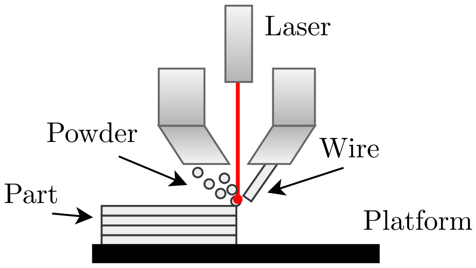

Figure A.6. Directed Energy Deposition. Inspired by Loughborough University (N.d.).

Sheet Lamination (SHL)

In SHL, sheets of material are supplied, cut to shape and bonded to form a part. The process uses spools of sheet material, and is visualized in Fig. A.7.

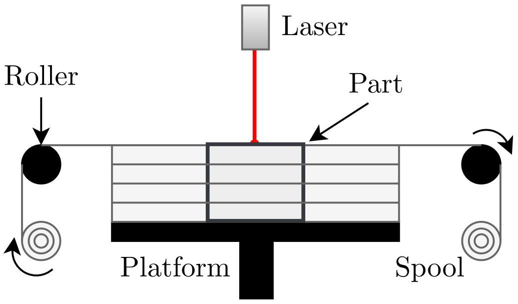

Figure A.7. Sheet lamination. Inspired by Loughborough University (N.d.).

B Orientation Projection Methods

This appendix presents different attempted definitions for component orientation projection. Used are 1) full circles, 2) ellipses and 3) semi-circles.

B.1 Shapes for Projection and Assessment

Marked with blue in Figs. B.1 to B.5 is the level-set of the higher order function for each curve segment. In black is the skeleton curve going from coordinate $(1, 0.4)$ to $(0.2, 0.4)$. The projected element-wise orientations are depicted with the red quiver plot and are computed in every segment from the discretized skeleton curve. The angles are computed with the atan2 operator, hence angle discontinuity is at $-\pi$ and π.

B.1.1 Circle Projection

Fig. B.1 shows circle angle projection, recursively projected (described in Appendix B.2) and Fig. B.2 shows projections with the average computed.

With the average in Fig. B.2, it is meant that each time the circle covers an element, the angle is projected, and the averaged angle is calculated based on how many times an element is covered by a circle as described in Sec. 6.3.3, but with direct angles instead of vectorized angles.

It is clearly seen, that the recursively placed, compared to the averaged, has a larger error between the angle of the curve and the projected angle to the FE-grid, close to where the curve ends and starts. Furthermore, because of the circular shape, there is a 'delay' in the assignment, i.e. where the angle is supposed to be zero (in the middle of the path) is shifted further to the right.

With averaging of angles in Fig. B.2, obvious errors in the angle projection are apparent.

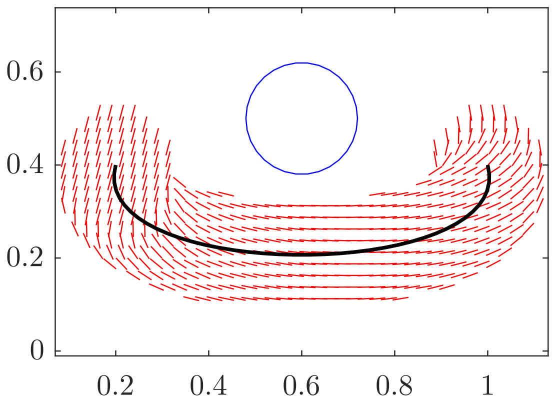

Figure B.1. Circle projection recursively placed.

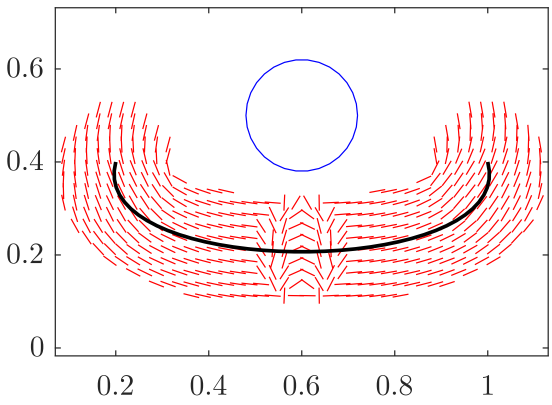

Figure B.2. Circle projection with averaging.

Fig. B.3 shows the case with the circle projection based on vectors, presented in Chap. 6. This result displays nearly exactly the element angles in Fig. B.2, but without the obvious error.

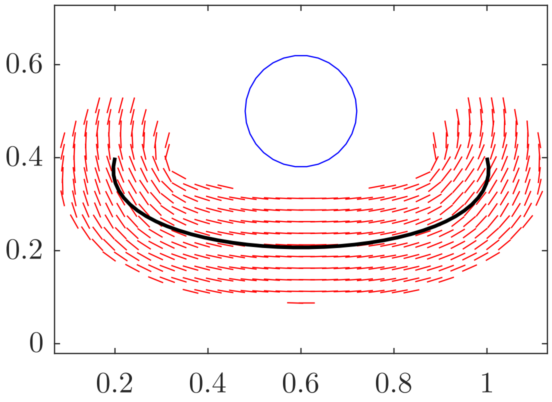

Figure B.3. Vectorized Circle projection with averaging.

B.1.2 Ellipse Projection

With the 'delay' problem described above, an intuitive solution is to change the shape to an ellipse, lessening the effect. Fig. B.4 shows ellipse angle projection, recursively placed.

By visual inspection, compared to the circle projection, the projected angles fit the angle of the skeleton better, in regions of high curvature.

However, as the two ellipses on the skeleton illustrate, there is a risk that the outer-most elements are not assigned an angle. Furthermore, in regions of high curvature, the inner-most elements angles are replaced by following ellipses. Furthermore, the ellipses segment shape does not match the density field segment shape. This discrepancy has to be accounted for.

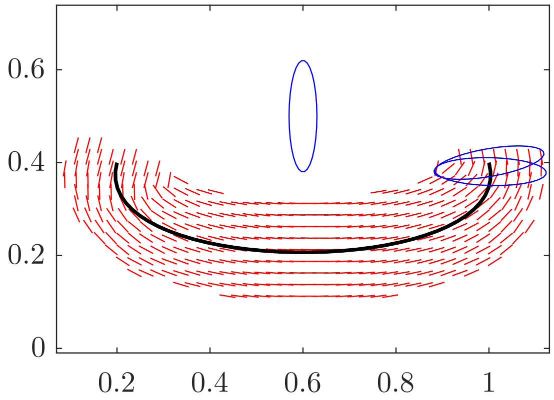

Figure B.4. Ellipse projection, recursively projected.

B.1.3 Semi-Circle Projection

Fig. B.5 shows semi-circle angle projection, recursively projected.

In this case, based on visual inspection, there is very little error between the angle of the curve and the projected angle to the FE-grid in all parts of the curve.

The two ends are different in shape, hence, a full circle at the first segment is needed to fit the density field made by circles. With this shape, the same curvature problem as was the case for the elliptical shape is present.

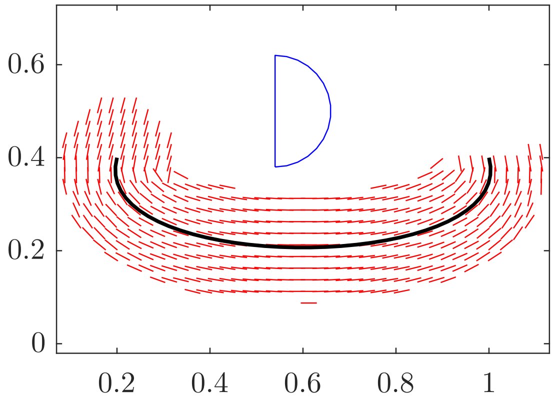

Figure B.5. Half-circle projection, recursively projected.

B.1.4 Assessment

By visual inspection and the parallelism definition from Sec. 6.3.3, the best-fitting projected element angles are obtained using the semi-circle projection. However, this definition is problematic for a thickness greater than the radius of curvature (see e.g. the area near $(0.3, 0.38)$ in Fig. B.5). Furthermore, the projected angles would have to be defined recursively causing nondifferentiabillity. Therefore an element-wise angle difference of the recursive projected semi-circles and the differentiable vectorized average of circles is used for evaluation of the error introduced by averaging. The difference is seen in Fig. B.6.

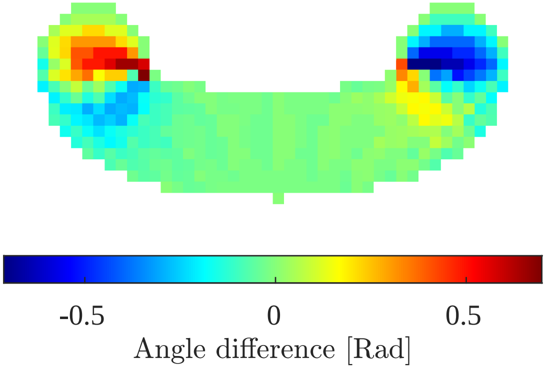

Figure B.6. Element-wise angle difference between Fig. B.5 and Fig. B.3.

From Fig. B.6 the maximum differences are seen at large curvature and namely the largest values are seen where the semi-circle projection is incorrect (thickness greater than radius of curvature). Taking the absolute value of each element and computing the average yields and average angular difference of 0.1 Rad. Evaluated from the maximum and average angular deviations and with the prospect of gained efficiency of analytic sensitivities, the circle projection method with averaged vectorized angles is used in this work.

The next section presents details on how the semi-circle projection can be implemented rather than the full-circle definition presented in Chap. 6.

B.2 Recursively Projected Semi-circles Description

Firstly the angle of each segment of the skeleton curve is computed from two points as in Eq. (B.1). Here the four-quadrant inverse tangent is used to avoid angular discontinuity at $\frac{\pi}{2}$ and $\frac{-\pi}{2}$ (Ukil et al., 2011).

$$\theta^{c,s} = \operatorname{atan2}\left(\frac{f_y^{c,s+1} - f_y^{c,s}}{f_x^{c,s+1} - f_x^{c,s}}\right) \tag{B.1}$$

To compute a higher dimensionality semi-circle according to placement an orientation of the skeleton curve, a domain transformation as in Eq. (B.2) is needed.

$$\begin{bmatrix} (x')^{c,s} \\ (y')^{c,s} \end{bmatrix} = \begin{bmatrix} \cos(\theta^{c,s}) & \sin(\theta^{c,s}) \\ -\sin(\theta^{c,s}) & \cos(\theta^{c,s}) \end{bmatrix} \begin{bmatrix} x - f_x^{c,s} \\ y - f_y^{c,s} \end{bmatrix} \qquad s = [1 : N_s] \tag{B.2}$$

From the transformed domains the higher order dimension semi-circles are given by Eq. (B.3b). Since the placement of the orientation field has to equal the density field the first segment of every curve is a full circle given by Eq. (B.3a).

$$\phi_\theta^{c,1} = \left(t + \frac{L_{elem}}{2}\right)^2 - \left((x')^{c,1}\right)^2 - \left((y')^{c,1}\right)^2 \tag{B.3a}$$

$$\phi_\theta^{c,s} = \begin{cases} \left(t + \frac{L_{elem}}{2}\right)^2 - \left((x')^{c,s}\right)^2 - \left((y')^{c,s}\right)^2, & (x')^{c,s} \geq 0 \\ -1, & (x')^{c,s} < 0 \end{cases} \qquad s = [2 : N_s] \tag{B.3b}$$

To form a component-wise higher order dimensionality function used in Eq. (B.6), every segment is combined to a unified description by Eq. (B.4).

$$\phi_\theta^c = \max(\phi_\theta^{c,1}, ..., \phi_\theta^{c,s}, ..., \phi_\theta^{c,N_s}) \qquad s = [1 : N_s] \tag{B.4}$$

From these segment- and component-wise functions, an angle projection to the fixed grid is implemented using level-sets. The angles are projected to element centers, as opposed to the density field being on element nodes, to have a single element-wise orientation. The projection is formulated recursively as in Eq. (B.5), where $\mathbb{H}_\theta^{c,s}$ denotes the orientation field of segment s in component c. The formulation is recursive since placement continuity is ensured from overlapping semi-circles and angle projection is only wanted segment-wise. Meaning orientations projected from different segments should not interact. A depiction of the component orientation field construction is seen in Fig. B.7 through Fig. B.9.

$$\mathbb{H}_\theta^{c,1} = \theta^{c,1}, \qquad \phi_\theta^{c,1} \geq 0 \tag{B.5a}$$

$$\mathbb{H}_\theta^{c,s} = \begin{cases} \theta^{c,s}, & \phi_\theta^{c,s} \geq 0 \\ \mathbb{H}_\theta^{c,s-1}, & \phi_\theta^{c,s} < 0 \end{cases} \qquad s = [2 : N_s] \tag{B.5b}$$

To simplify notation, component-wise orientation fields are written as $\mathbb{H}_\theta^{c,N_s} = \mathbb{H}_\theta^c$. The full structure orientation field $\mathbb{H}_{\theta,full}$, is formed recursively as in Eq. (B.6). By doing this, the order in which components are recursively projected defines which component is dominant, which is unwanted.

$$\mathbb{H}_{\theta,full}^c = \begin{cases} \mathbb{H}_\theta^c, & \phi_\theta^c \geq 0 \\ \mathbb{H}_{\theta,full}^{c-1}, & \phi_\theta^c < 0 \end{cases} \qquad c = [1 : N_c] \tag{B.6}$$

The full orientation field is depicted in Fig. B.10 and the notation is simplified to $\mathbb{H}_{\theta,full}^{N_c} = \mathbb{H}_\theta$.

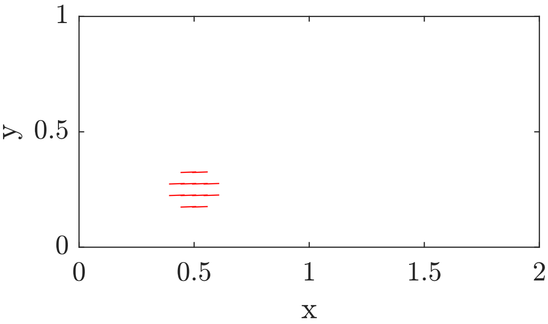

Figure B.7. First segment orientation field $\mathbb{H}_\theta^{c,s}$.

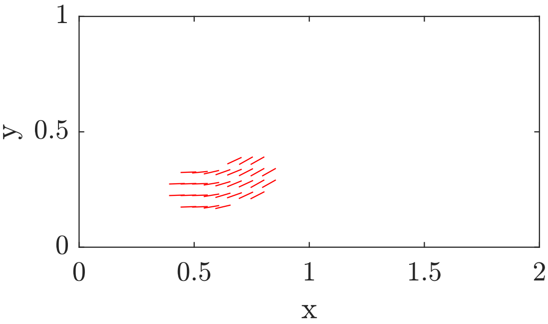

Figure B.8. Component orientation field $\mathbb{H}_\theta^{c,s}$, $s = 10$.

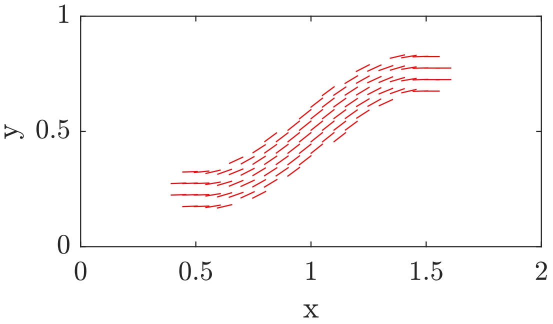

Figure B.9. Component orientation field $\mathbb{H}^c_\theta$.

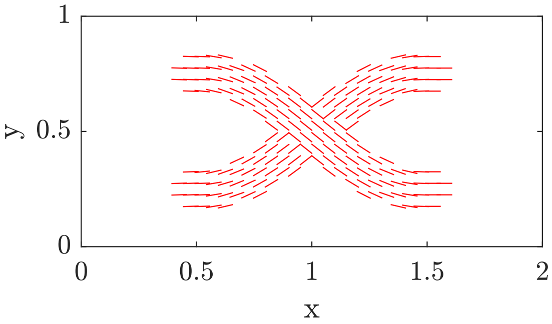

Figure B.10. Structure orientation field $\mathbb{H}_\theta$.

C | Implementation Details

This appendix presents details utilized in the presented scheme but not included in the main report.

C.1 Stiffness and Volume Gradients

The finite differences are computed as central differences seen for stiffness computation in Eq. (C.1). Here $\boldsymbol{\delta}$ is a perturbation vector, e denotes the element number and n nodal numbering according to every element. N_e is the total number of elements.

$$\frac{\Delta \mathbf{K}}{\Delta \mathbf{d}^d} = \frac{\mathbf{K}_{\boldsymbol{\delta}+} - \mathbf{K}_{\boldsymbol{\delta}-}}{2\boldsymbol{\delta}^d} \qquad d = [1 : N_d] \tag{C.1a}$$

$$\mathbf{K}_{\boldsymbol{\delta}+} = \sum_{e=1}^{N_e} \mathbf{K_e}^e \Big(\mathbf{C}^e \Big(\boldsymbol{\rho}^e \Big(\mathbb{H}_\rho^{e,n} \Big(\mathbf{d} + \boldsymbol{\delta}^d \Big) \Big) , \bar{\mathbf{Q}}^e \Big(\mathbf{T}^e \Big(\mathbb{H}_\theta^e \Big(\mathbf{d} + \boldsymbol{\delta}^d \Big) \Big) \Big) \Big) \Big) \Big) \tag{C.1b}$$

$$\mathbf{K}_{\boldsymbol{\delta}-} = \sum_{e=1}^{N_e} \mathbf{K_e}^e \Big(\mathbf{C}^e \Big(\boldsymbol{\rho}^e \Big(\mathbb{H}_\rho^{e,n} \Big(\mathbf{d} - \boldsymbol{\delta}^d \Big) \Big) , \bar{\mathbf{Q}}^e \Big(\mathbf{T}^e \Big(\mathbb{H}_\theta^e \Big(\mathbf{d} - \boldsymbol{\delta}^d \Big) \Big) \Big) \Big) \Big) \Big) \tag{C.1c}$$

The central difference approximation of the volume is given in Eq. (C.2), where W and H are domain width and height respectively.

$$\frac{\Delta V}{\Delta \mathbf{d}^d} = \frac{V_{\delta+} - V_{\delta-}}{2\delta^d} \qquad d = [1 : N_d] \tag{C.2a}$$

$$V_{\delta+} = \frac{1}{4WH} \sum_{e=1}^{N_e} \sum_{n=1}^{4} \mathbb{H}_\rho^{e,n}(\mathbf{d} + \boldsymbol{\delta}^d) \tag{C.2b}$$

$$V_{\delta-} = \frac{1}{4WH} \sum_{e=1}^{N_e} \sum_{n=1}^{4} \mathbb{H}_\rho^{e,n}(\mathbf{d} - \boldsymbol{\delta}^d) \tag{C.2c}$$

C.2 Aggregation Techniques

The purpose of aggregate functions is to aggregate multiple values into one, or a few, values. In an optimization context, aggregation can be used to e.g. reduce the number of constraints. A variety of aggregation functions have been proposed. The most common in structural optimization are the P-norm (Eq. (C.3a)), P-mean-norm (Eq. (C.3b)) and the

Kreisselmeier-Steinhauser function (Eq. (C.3c)) (Verbart et al., 2015).

$$\text{P-norm:} \qquad ||\mathbf{f}||_P = \left(\sum_{e=1}^{N_e} (\mathbf{f}^e)^P\right)^{\frac{1}{P}} \tag{C.3a}$$

$$\text{P-mean-norm:} \qquad ||\mathbf{f}||_{PM} = \left(\frac{1}{N_e}\sum_{e=1}^{N_e} (\mathbf{f}^e)^P\right)^{\frac{1}{P}} \tag{C.3b}$$

$$\text{K-S:} \qquad f_{KS} = \frac{1}{P}\ln\left(\sum_{e=1}^{N_e} e^{P\mathbf{f}^e}\right) \tag{C.3c}$$

The P-norm and P-mean-norm are considered upper and lower bounds, respectively. The three functions in Eq. (C.3) are compared in an example in Fig. C.1.

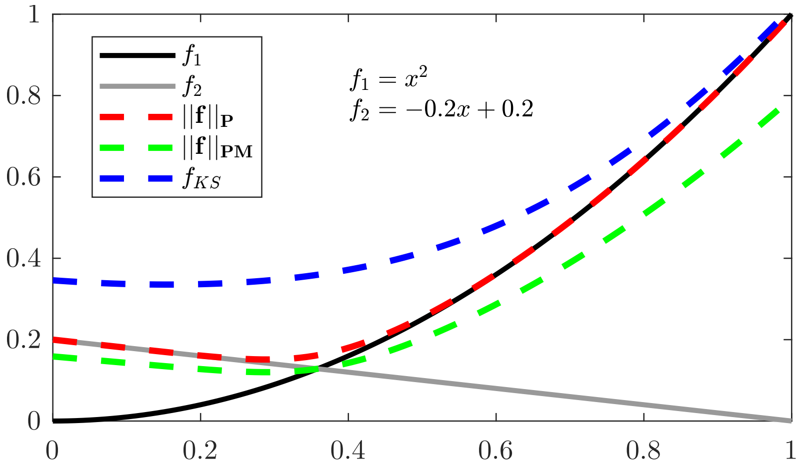

Figure C.1. Aggregate functions, $P = 3$.

In this example, the P-norm function provides a good estimate of the maximum value of the two functions.

All the above functions converge to the maximum value for in the limit of increasing P. This statement only applies to the P-norm when values are strictly positive. For the K-S function, values need not be strictly positive to fulfill this criterion, hence, the K-S function is used when aggregated values can be negative (Verbart et al., 2015).

D | Additional Results

This appendix presents additional information to the results presented throughout the report.

D.1 Additional Results from Unconstrained Formulation

These results are obtained from the optimization formulation in Chap. 6.

D.1.1 Iteration History

Fig. D.1 shows the same iteration history as in Fig. 6.20, from 383 iterations to 1000 iterations, due to the large compliance change.

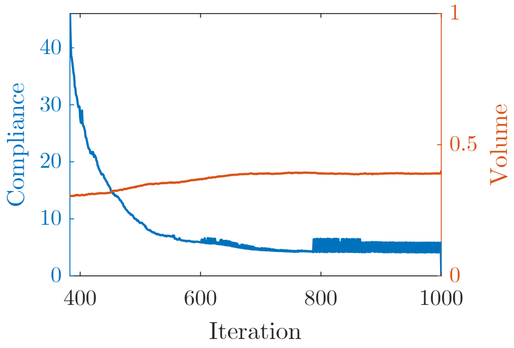

Figure D.1. Iteration history of short cantilever beam. (Same as Fig. 6.20).

D.1.2 Result with Different Stiffness Scaling

The resulting structure in Fig. D.2 is obtained using the unconstrained formulation and parameters as presented in Chap. 6. The difference is using the stiffness-scaling in Eq. (D.1). Here, low-density elements still have orthotropic properties.

$$\mathbf{C}^e = \mathbf{C}_{\mathbf{iso}}(1 - (\boldsymbol{\rho}^e)^2) + \bar{\mathbf{Q}}^e(\boldsymbol{\rho}^e)^2 \tag{D.1}$$

The angle of the low-density elements is 0° corresponding to horizontal in the following figure, and $E = 1\,\text{MPa}$ is used.

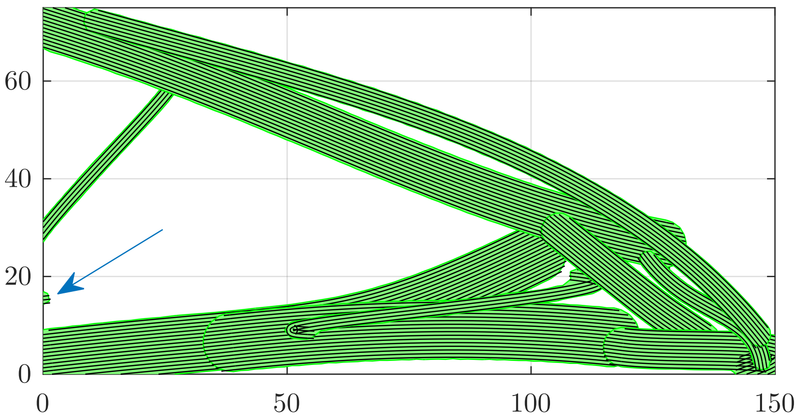

Figure D.2. Structure obtained with a different stiffness scaling. Ran for 2270 iterations.

D.1.3 Alignment with Principal Stress Directions

Fig. D.3 shows the principal stress directions of each element. This plot is generated using a modified version of a code from Elmstrøm et al. (2023). Blue indicates compression and red indicates tension. The length of each line indicates the magnitude, thus the lengths in each element is normalized with respect to the largest principal stress in that element.

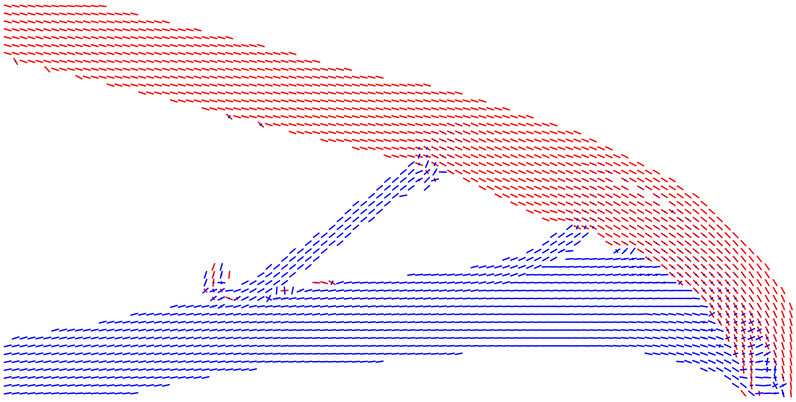

Figure D.3. Principal stress directions.

Fig. D.4 shows the error between the projected fiber angle and the angle of the largest principal stress.

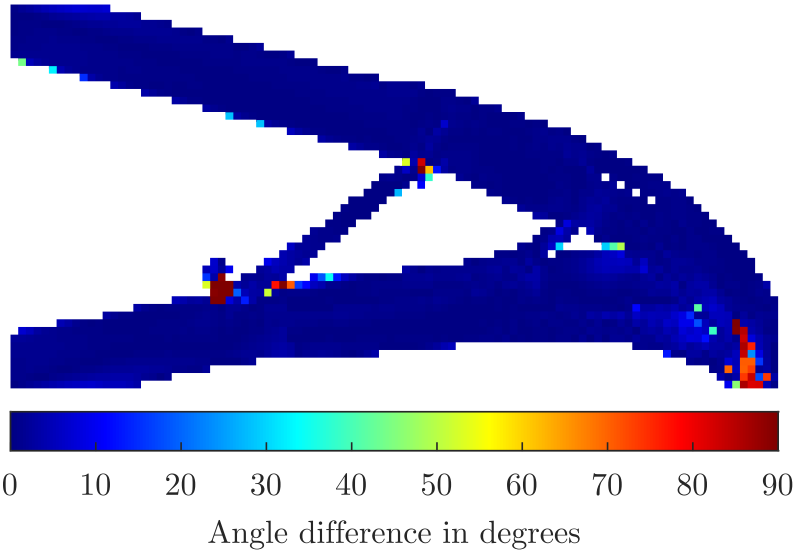

Figure D.4. Angle error between largest principal stress and projected fiber angle.

In Fig. D.4, the colorbar has a rather large range. Fig. D.5 shows that, for most of the structure, the error is smaller than 5°.

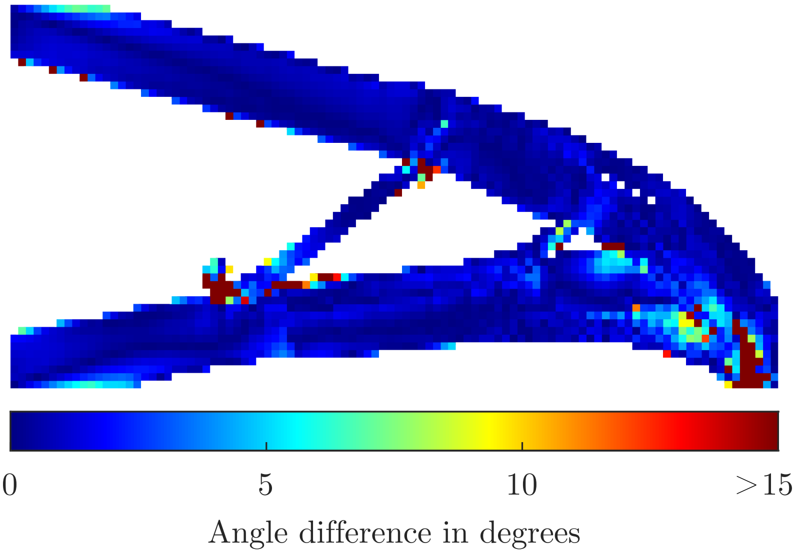

Figure D.5. Angle error between largest principal stress and projected fiber angle. Smaller colorbar range.

D.2 Additional Results from Constrained Formulation

Here, additional information regarding the results presented in Chap. 7.

D.2.1 Analysis Model Depictions for Fully Constrained Result

The orientation and density fields of the fully constrained result in Sec. 7.5.2 are depicted in Fig. D.6 and Fig. D.7 respectively.

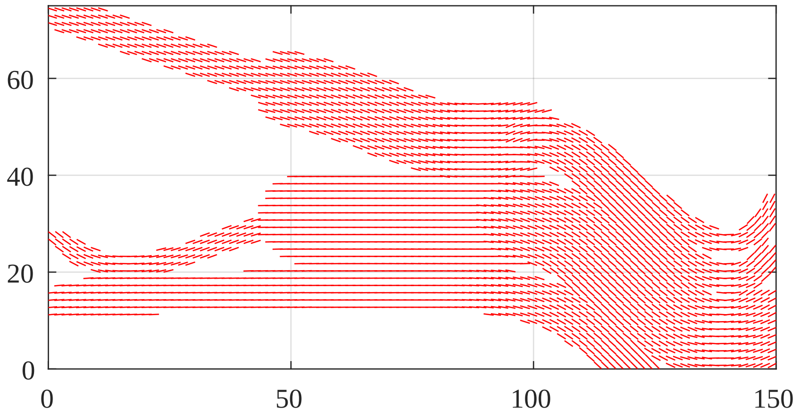

Figure D.6. Orientation field for fully constrained result in Fig. 7.14.

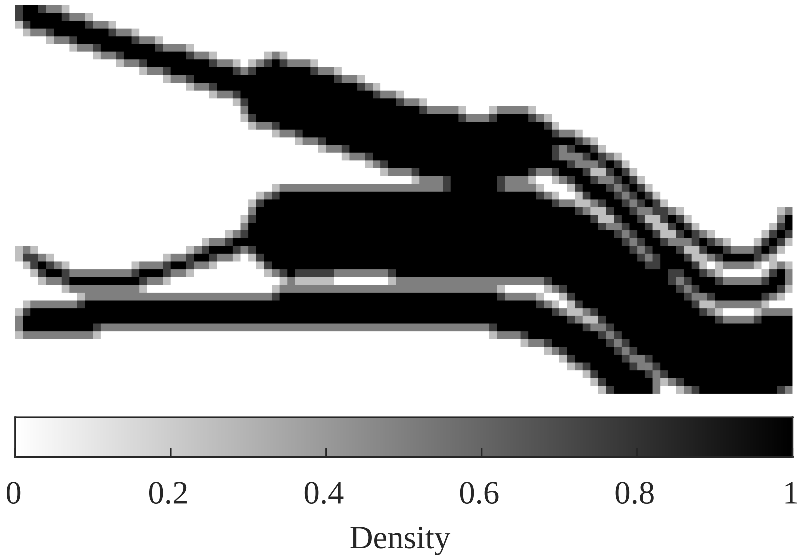

Figure D.7. Density field for fully constrained result in Fig. 7.14.

D.2.2 Analysis Model Depictions for Tuned Constrained Result

The orientation and density fields of the fully constrained result in Sec. 7.5.5 are depicted in Fig. D.8 and Fig. D.9 respectively.

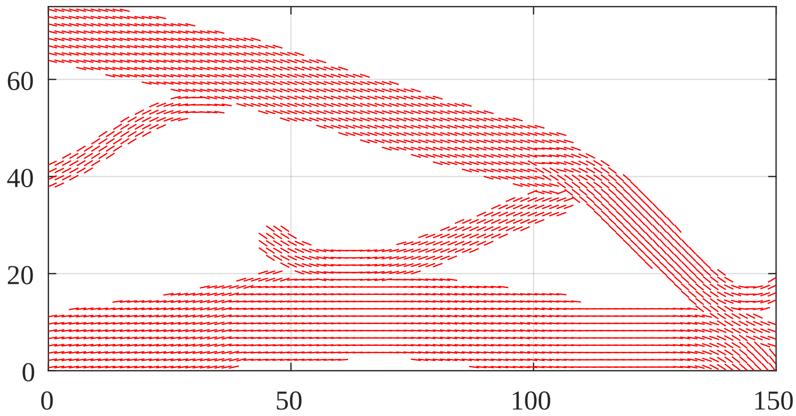

Figure D.8. Orientation field for tuned result in Fig. 7.27.

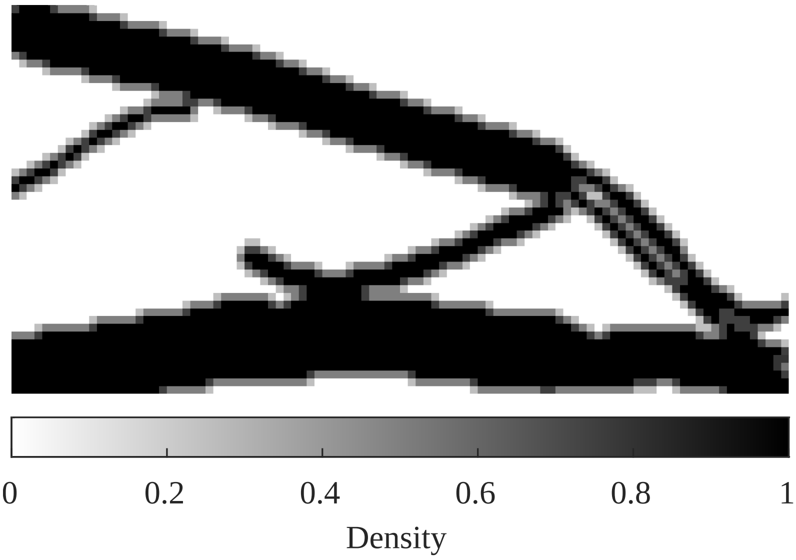

Figure D.9. Density field for tuned result in Fig. 7.27.

D.2.3 Tuned Constrained Result - Optimization Progression

Here, the progression of the structure in Fig. 7.27 is depicted.

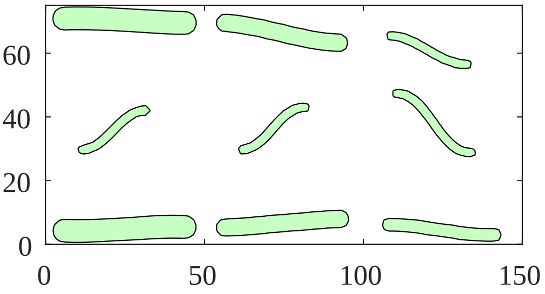

Figure D.10. 100 iterations.

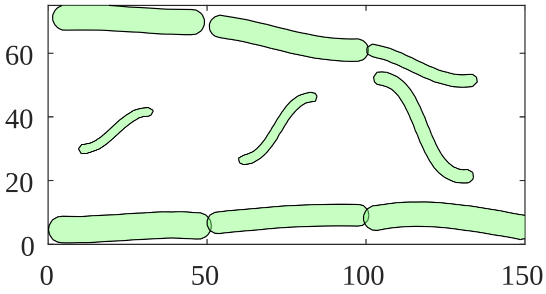

Figure D.11. 200 iterations.

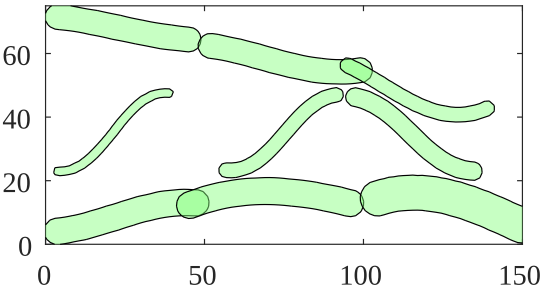

Figure D.12. 300 iterations.

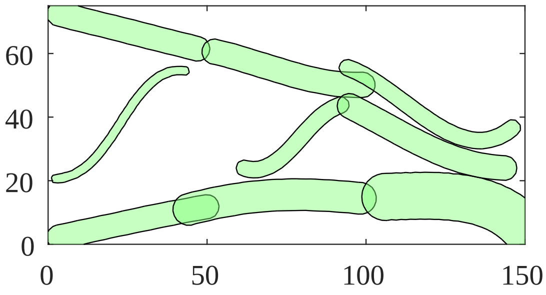

Figure D.13. 400 iterations.

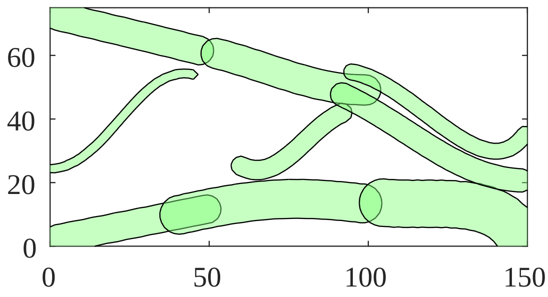

Figure D.14. 500 iterations.

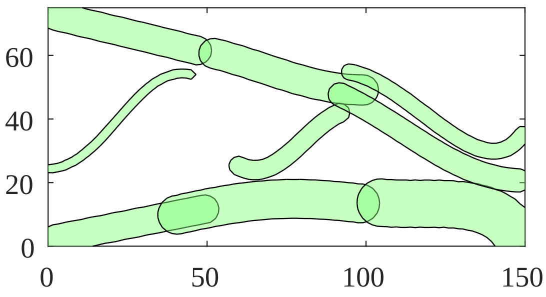

Figure D.15. 600 iterations.

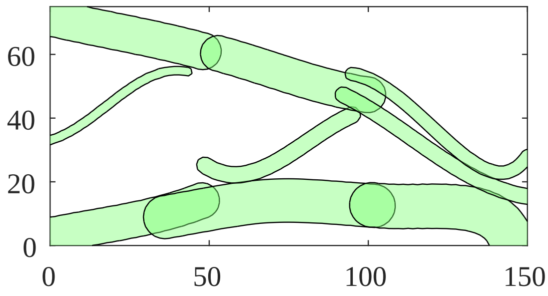

Figure D.16. 700 iterations.

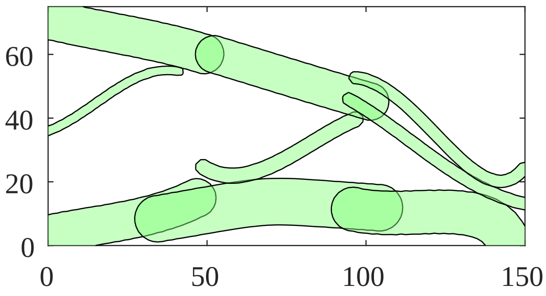

Figure D.17. 800 iterations.

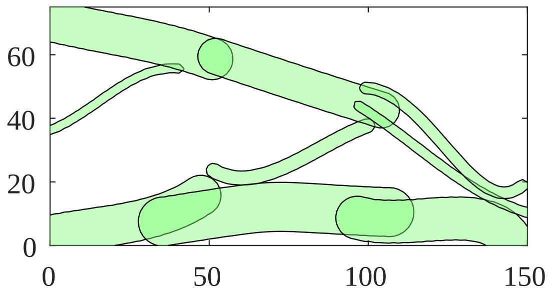

Figure D.18. 900 iterations.

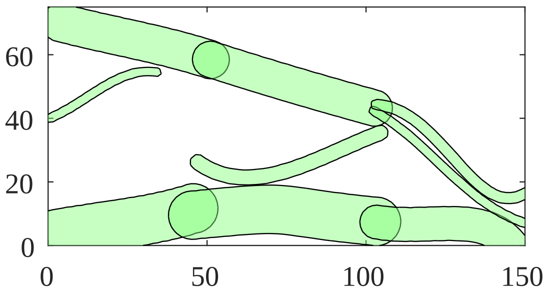

Figure D.19. 1000 iterations.

D.3 Details of Other Benchmark Examples

The boundary conditions for the computed MBB beam and L-bracket are given in Fig. D.20 and Fig. D.21.

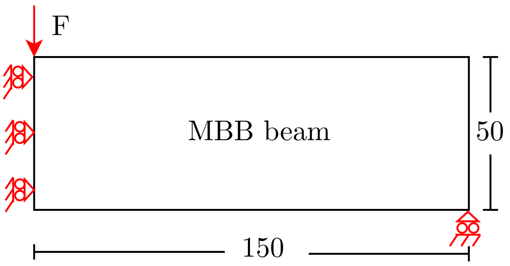

Figure D.20. MBB beam boundary conditions. Dimensions mm.

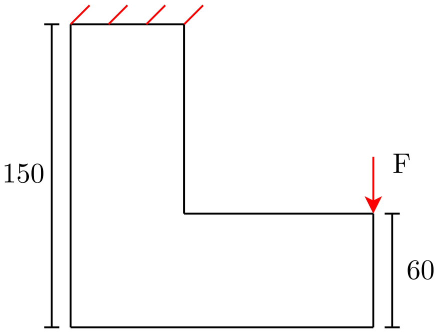

Figure D.21. L-bracket boundary conditions. Dimensions mm.

The convergence history for the MBB beam is given by Fig. D.22 and Fig. D.23.

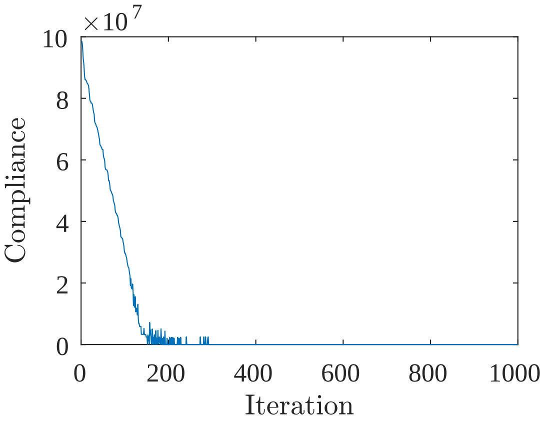

Figure D.22. Compliance of the first 1000 iterations.

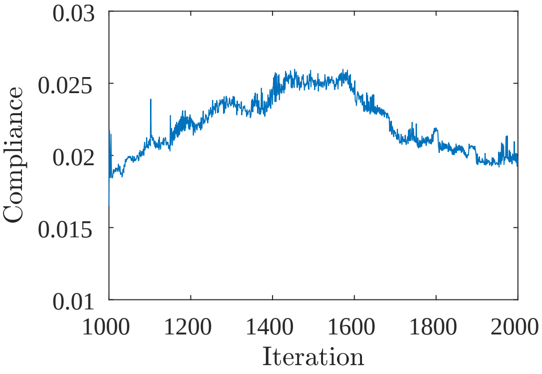

Figure D.23. Compliance from iteration 1000-2000.

The convergence history for the L-bracket is given by Fig. D.24 and Fig. D.25.

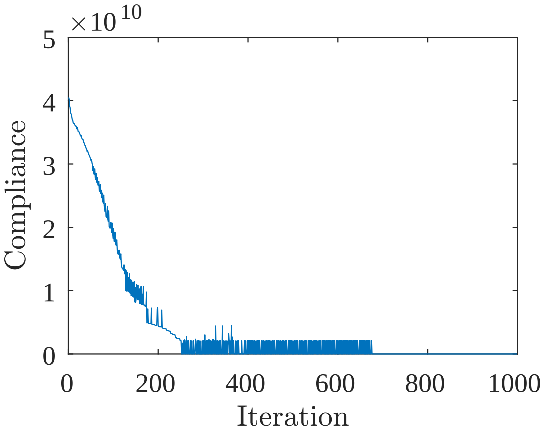

Figure D.24. Compliance of L-bracket example 0-1000 iterations.

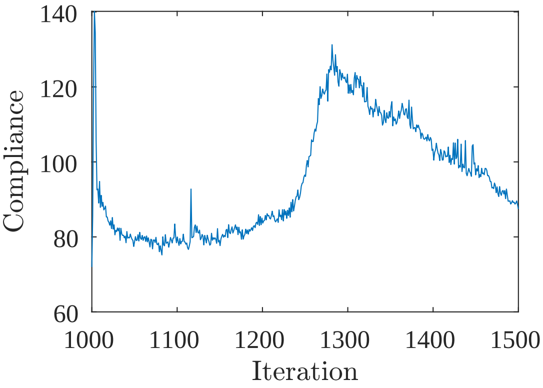

Figure D.25. Compliance of L-bracket example 1000-1500 iterations.

D.3.1 MBB beam - Resulting Fields

The orientation and density fields from the resulting MBB structure are seen in Fig. D.26 and Fig. D.27 respectively.

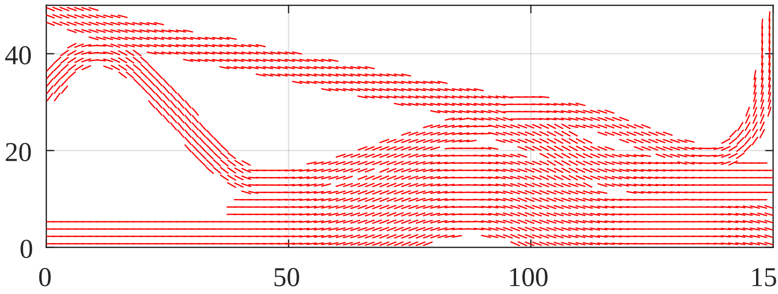

Figure D.26. Orientation field for tuned result in Fig. 9.3.

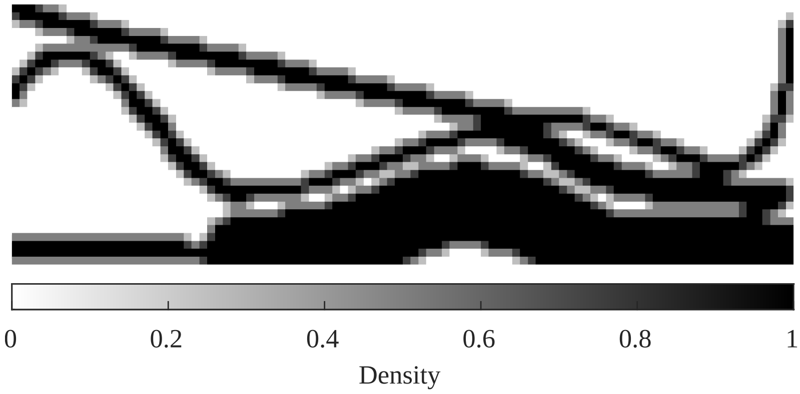

Figure D.27. Density field for tuned result in Fig. 9.3.

D.3.2 L-bracket - Resulting Fields

The orientation and density fields from the resulting L-bracket structure are seen in Fig. D.28 and Fig. D.29 respectively.

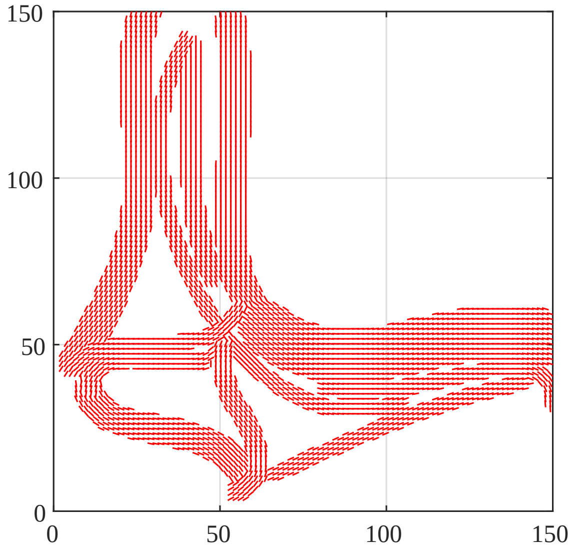

Figure D.28. Orientation field for tuned result in Fig. 9.4.

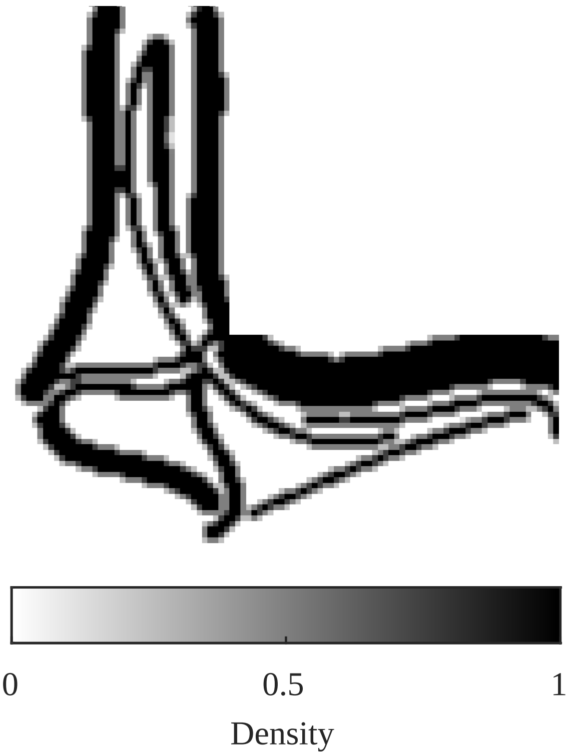

Figure D.29. Density field for tuned result in Fig. 9.4.

E

Geometrically Computed Allowable Overlap

E.1 Formulation

The initial idea for computation of the allowable endpoint overlap $V^r_{overlap}$, was to compute the volume geometrically. The approach proved insufficient due to the optimizer utilizing the discrepancy of geometric and discrete density based volumes, to form infeasible overlap, as shown in Appendix E.2. However the approach only produced 0.6% infeasible overlapping volume and highlight the idea while being continuous and differentiable. Further, if other grid methods than using a fixed grid was implemented, the discrepancy might not occur and computation would be both correct and provide possible analytical sensitivities of the overlap constraint.

As stated in Sec. 7.3.1, the allowable overlap should only be computed if the criteria are fulfilled. For clarification the endpoint connection relation and criteria are repeated in Fig. E.1 and listed respectively.

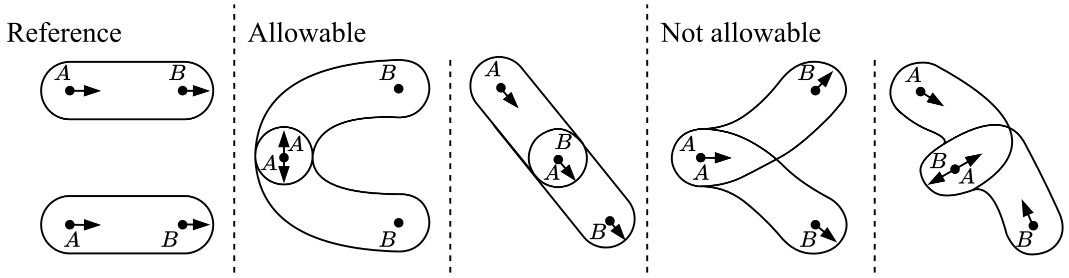

Figure E.1. Depiction of allowable overlap from endpoint A to B relation.

- If $\mathbf{l}^r_{int} \leq \mathbf{l}^r_{touch}$
- If A-A or B-B relation and $\frac{\pi}{2} \leq \boldsymbol{\theta}^r_{int} \leq \frac{3\pi}{2}$
- If A-B or B-A relation and $0 \leq \boldsymbol{\theta}^r_{int} \leq \frac{\pi}{2}$ or $\frac{3\pi}{2} \leq \boldsymbol{\theta}^r_{int} \leq 2\pi$

Computation of these criteria is achieved by Eq. (E.1) and Eq. (E.2) constructed with reference to an analytical step function. Further, the volume should only be computed when endpoint segments touch. For computation of the distance dependence the step function in Eq. (E.3) is utilized.

$$\mathbf{f}^r_{ori,AA} = \frac{1}{1+e^{-k_{ori}(\theta^r_{int}-\frac{\pi}{2})}}\frac{1}{1+e^{k_{ori}(\theta^r_{int}-\frac{3\pi}{2})}}, \qquad if \quad A-A \quad B-B \tag{E.1}$$

$$\mathbf{f}^r_{ori,AB} = \frac{1}{1+e^{k_{ori}(\theta^r_{int}-\frac{\pi}{2})}}+\frac{1}{1+e^{-k_{ori}(\theta^r_{int}-\frac{3\pi}{2})}}, \qquad if \quad A-B \quad B-A \tag{E.2}$$

$$\mathbf{f}^r_{dist} = \frac{1}{1+e^{k_{dist}(\mathbf{l}^r_{int}-\mathbf{l}^r_{contact})}} \tag{E.3}$$

Here $k_{ori} = 10$ and $k_{dist} = 50$ is used. For visualization the combined orientation and distance step function is rewritten from the polar coordinates $\boldsymbol{\theta}^r_{int}$ and $\mathbf{L}^r_{int}$ to Cartesian coordinates and depicted in Fig. E.2.

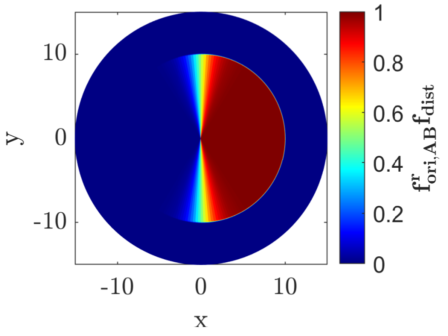

Figure E.2. Depiction of criteria functions.

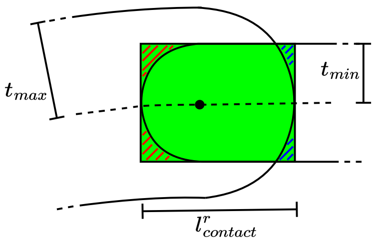

Figure E.3. Sketched overlap volume computation.

From Fig. E.2 the overlapping volume is only computed if the orientation and distance criteria are fulfilled. The geometrically computed volume is depicted in Fig. E.3 and formulated as in Eq. (E.4). Here the first term in Eq. (E.4b) account for the sketched green volume. The second and third term subtracts the sketched red and blue volume respectively. These volumes are averaged over the length $\mathbf{l}^r_{contact}$.

$$t_{min} = \min(t^c, t^q) \quad t_{max} = \max(t^c, t^q) \quad \theta = tan^{-1}\left(\frac{t_{min}}{t_{max}}\right) \tag{E.4a}$$

$$f^r_{vol} = 2t_{min} - \frac{(2-0.5\pi)t^2_{min}}{\mathbf{l}^r_{contact}} - \frac{2(t_{min}t_{max} - 0.5\theta t^2_{max} - 0.5t_{min}t_{max}\cos\theta)}{\mathbf{l}^r_{contact}} \tag{E.4b}$$

The tedious volume computation is to strictly only compute the actual allowable overlap. From the described criteria step functions and the volume computation, the allowable overlap volume is described by Eq. (E.5).

$$V^r_{overlap} = f^r_{ori}f^r_{dist}f^r_{vol}\frac{\mathbf{l}^r_{contact}-\mathbf{l}^r_{int}}{WH} \tag{E.5}$$

These definitions could be implemented directly in the overlap constraint in Eq. (7.15).

E.2 Discrepancy Between Geometric and Discrete Method

To clarify the discrepancy occurring between the geometric overlap volume computation and the used overlap computation from the density field, two endpoints connecting is sketched in Fig. E.4. The sketched blue and red components are the same component with different thicknesses.

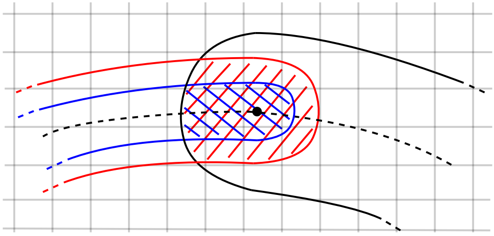

Figure E.4. Discrepancy of geometric and discrete overlap volume.

From the continuous geometric overlapping volume computation, it is obvious that the overlapping volume $V^r_{overlap}$ is larger for the red component than the blue.

If the volume is computed by the discrete element-wise densities, the overlapping volume $V^r_{overlap}$ is indifferent between the sketched red and blue component. This is due to the Heaviside density projection being to nodes and as depicted the red and blue components are projected to the same nodes inside the overlapping area.

Thereby the allowable overlapping volume $\sum_{r=1}^{N_r} V^r_{overlap}$ in the overlap constraint, repeated in Eq. (E.6), could be artificially increased by the geometric approach.

$$g_{overlap} = \sum_{c=1}^{N_c} V^c_c - \sum_{r=1}^{N_r} V^r_{overlap} - V \leq 0 \tag{E.6}$$

This was utilized by the optimizer to form physically infeasible overlap while still fulfilling the overlap constraint. This is seen by comparison of the structures in Fig. E.5 and Fig. E.6 where the discrepancy is utilized to form infeasible overlap near to the load in Fig. E.6.

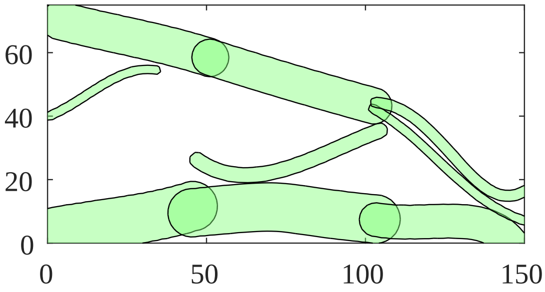

Figure E.5. Structure with discrete computed overlap volume.

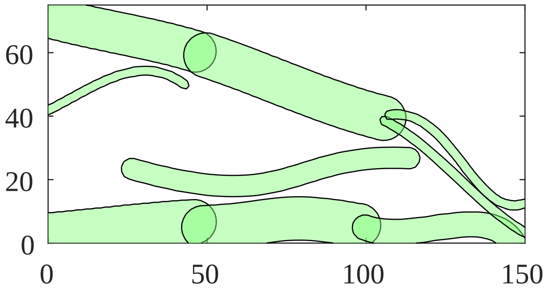

Figure E.6. Structure with geometric computed overlap volume.